UNIVERSITY OF OKLAHOMA

GRADUATE COLLEGE

CHARACTERIZATION OF THE IRON SULFIDE OXIDATION PRODUCTS FORMED DURING REDUCTIVE DECHLORINATION OF CHLORINATED ALIPHATIC CONTAMINANTS

A DISSERTATION

SUBMITTED TO THE GRADUATE FACULTY

in partial fulfillment of the requirements for the

Degree of

DOCTOR OF PHILOSOPHY

By

YING LAN
Norman, Oklahoma
2016

Downloaded from SHAREOK. Persistent Handle URL: https://hdl.handle.net/11244/34656

CHARACTERIZATION OF THE IRON SULFIDE OXIDATION PRODUCTS FORMED DURING REDUCTIVE DECHLORINATION OF CHLORINATED ALIPHATIC CONTAMINANTS

A DISSERTATION APPROVED FOR THE
SCHOOL OF CIVIL ENGINEERING AND ENVIRONMENTAL SCIENCE

BY

_____
Dr. Elizabeth C. Butler, Chair

_____
Dr. Andrew S. Elwood Madden

_____
Dr. Robert W. Nairn

_____
Dr. Mark A. Nanny

_____
Dr. David A. Sabatini

© Copyright by YING LAN 2016
All Rights Reserved.

ACKNOWLEDGEMENTS

During the last year of my Ph.D. studies, I keep thinking about one question: "What should I write in my acknowledgements to make it the most interesting and read-worthy part of my dissertation? How can I sum up the profound impacts others have had on my doctoral journey in two pages?" Thanks to my procrastination, I have never had a good answer for this question until now.

Dr. Elizabeth Butler is the first person I would like to thank. She trains me to think and work as a scientist, and helps me to continually find myself scientifically and professionally. I appreciate all her guidance and supports during my five-years of study at the University of Oklahoma. I especially appreciate her trust in me. I have learned a lot from her profound knowledge and serious scientific attitude to research. This attitude will guide me through my career. Special thanks to her for allowing my dissertation to cut in line to the top of her very long to-do list, and giving all the detailed comments to improve my work.

Dr. Andrew Elwood Madden introduced me to Environmental Geochemistry, and the amazing world of microscopy and spectroscopy in which I really enjoy working. He continues to generously share his knowledge and experience with geochemistry and mineralogy with me. I really enjoyed Dr. Mark Nanny's Aquatic Chemistry class, and it is the most challenging course I have ever taken. I learned how to think critically in research, and I admire his superior gifting in sharing his passion through excellent classroom management. Thank you to Dr. David Sabatini and Dr. Robert Nairn for serving on my dissertation committee, and for their ultimate support whenever I needed it.

Thank you to Dr. Preston Larson, Greg Strout, and Brittany Pritchett for assistance with solid sample analyses. Dr. Jason FitzSimmons and Dr. Hong Lin offered me the opportunity of working with the Center for Teaching Excellence, which truly created great memories outside of the lab life.

Special thanks to my friends, without them, my Ph.D. life would have been much more tedious. Many thanks to Junyi Du for all the help both as a co-worker and a true friend who has always been there in times of need. Hiking, camping, and running are the new hobbies Hao Ye has passed on to me. Finishing two half-marathons was surely not on my check-list and could not have been completed without the support of the Run4PhD team. Yuchao Jiang has been a great team member both in the Run4PhD team and the dissertation camp. Thank you to Lixia Chen, Lili Hou, and Jingling Hu for their support and friendship. Carol Ann Lindley offers me a sweet and welcoming host family, it will always be a heart-warming spot whenever I think about Norman. Additional thanks to the Wallace family, they are the most international-student-friendly family I have ever met.

My biggest thanks go to my mother, Liping Shi, to her I dedicate this dissertation. My long journey in the science world started from her Chemistry classroom when she was a Chemistry teacher during my younger years. Without the ultimate support from her and my family, I would not be the person I am right now.

Last but not least, Dr. Xiaoming Xu is the most phenomenal person I have ever met. His constant support and love have been unending. He sees all my flaws and blemishes, accepts them, and works around them with me. Thank you for always comforting me when I could not find my way.

TABLE OF CONTENTS

ACKNOWLEDGEMENTS iv

LIST OF TABLES viii

LIST OF FIGURES ix

ABSTRACT xiii

Chapter 1 Introduction 1

1.1. Formation and structure of mackinawite (FeS) 1
1.2. Transformation of FeS in natural conditions 1
1.3. Transformation of FeS during reaction with contaminants 3
1.4. Dechlorination of Chlorinated Aliphatic Contaminants by FeS 4
1.5. Overview of this dissertation 7
References 10

Chapter 2 Monitoring the Transformation of Mackinawite to Greigite and Pyrite on Polymer Supports 14

2.1. Introduction 14
2.2. Materials and methods 18
2.2.1. Anaerobic conditions 18
2.2.2. Synthesis of mackinawite 18
2.2.3. PMMA supports 19
2.2.4. Batch experiments 19
2.2.5. SEM, EDS, and XRD analyses 21
2.3. Results and discussion 22
2.4. Conclusions 26
References 27

Chapter 3 Iron Sulfide Oxidation Products Formed during Reductive Dechlorination of Carbon Tetrachloride 31

3.1. Introduction 31
3.2. Material and methods 33
3.2.1. General experimental conditions 33
3.2.2. Experiments to measure dissolved species over time 35
3.2.3. Experiments for FeS mineral characterization 36
3.3. Results and discussion 39
3.3.1. Kinetics of CT transformation by FeS 39
3.3.2. Characterization of the FeS surface after reaction with CT 44
3.3.3. Environmental Implications 52
References 53

Chapter 4 Iron Sulfide Oxidation Products Formed during Reductive Dechlorination of Trichloroethylene and Tetrachloroethylene 59

4.1. Introduction 59
4.2. Material and methods 61

4.2.1. General experimental conditions 61
4.2.2. FeS synthesis 61
4.2.3. Experiments to measure dissolved species over time 62
4.2.4. Experiments for FeS mineral characterization 63
4.3. Results and discussion 66
4.3.1. Kinetics of TCE and PCE transformation by FeS 66
4.3.2. Characterization of the FeS surface after reaction with TCE and PCE 69
4.4. Conclusion 88
References 89

Chapter 5 Conclusions and Recommendations 94

5.1. Conclusions 94
5.2. Recommendations for future work 96
5.2.1. Dechlorination ability of stabilized FeS 96
5.2.2. Surface characterization of greigite 97
References 98

Appendix A Supporting Information for Chapter 3 100

A1. FeS synthesis 100
A2. Analytical methods 100
A3. Chloride mass balance 101
A4. Characterization of FeS by XRD 101
A5. Characterization of FeS by XPS and XPS spectra analysis 102
A6. Eh-pH diagram 103
A7. Coexistence of FeS and $FeCO_3$ in sulfate-reducing conditions 103
References 116

Appendix B Supporting Information for Chapter 4 117

B1. D-spacing calculation 117

LIST OF TABLES

Table 2.1. Measured properties of minerals shown in Figure 2.2 (top part of table) and reported or theoretical properties of pure minerals (bottom part of table). 25

Table 4.1*. Concentrations used in different experimental setups. 63

Table 4.2*. Atomic percent (in %) obtained from XPS high energy resolution spectra 80

Table A1. Concentrations of FeS and CT used in different experimental setups 105

Table A2*. Relative atomic percentage** (in %) obtained from XPS high energy resolution spectra of FeS surface after reaction with CT for 14 days at pH 8. 0.0016 M FeS; 0.022 M Tris buffer; $(2.1\pm0.2)\times10^{-3}$ M CT. 106

Table A3*. Standard state free energies of formation used for Eh-pH diagram for the Fe-S-H_2O system at 25°C (Figure A7). 107

Table B1. Atomic percent (in %) of surface species on the FeS surface 118

Table B2. Changes in Fe:S and Fe:O in FeS samples during reaction with TCE and PCE at pH 8. 119

LIST OF FIGURES

Figure 1.1. A schematic summary of FeS transformation products by various environmental species. References of the transformations showed in the figure can be found in Sections 1.2 and 1.3..... 3

Figure 1.2. Overview of research tasks addressed in this dissertation. 7

Figure 2.1. SEM image of FeS particles adhered to a PMMA support after being placed in water for 7 days. 21

Figure 2.2. SEM images of FeS adhered to PMMA supports after reaction with 0.1 M sulfur at pH 6 and 75-78 ^{o}C. 23

Figure 3.1. Aqueous concentration changes during reaction of FeS with CT. (A, B) CT and CF; (C, D) dissolved Fe^{+2}; (E, F) dissolved S(-II); 0.003 M FeS; 0.022 M Tris buffer; C0, CT =6×10^{-4} M. Error bars (panels E and F) represent the standard deviation of the mean from duplicate analyses. For other parameters (panels A-D), measurements typically agreed within 5%. 41

Figure 3.2. Changes in Fe:S and Fe:O during reaction with CT at pH 8; (A) Fe:S and (B) Fe:O. See text for definition of Fe:S and Fe:O. The error bars represent the standard deviation of seven measurements. Conditions: 0.022 M Tris buffer, 0.003 M FeS, $(2.1\pm0.2)\times10^{-3}$ M CT..... 44

Figure 3.3. SEM images of FeS at 14 days (A) FeS, no-CT control, pH 7; (B) FeS with CT, pH 7; (C) FeS, no-CT control, pH 8; (D) FeS with CT, pH 8. All samples had 0.022 M Tris buffer, 0.003 M FeS, and $(2.1\pm0.2)\times10^{-3}$ M CT. 46

Figure 3.4. The XPS spectra of the FeS surface at pH 8, 14 days. (A) Fe $2p_{3/2}$ spectrum of no-CT control; (B) S 2p spectrum of no-CT control; (C) Fe $2p_{3/2}$ spectrum of FeS with CT; (D) S 2p spectrum of FeS with CT; Black dotted lines are experimental data, and green dashed lines are corresponding fits. The bars on top of each spectrum represent the relative proportions of species. 0.0016 M FeS; 0.022 M Tris buffer; $(2.1\pm0.2)\times10^{-3}$ M CT. 49

Figure 4.1. Aqueous concentration changes during reaction of FeS with TCE and PCE. (A) TCE; (B) PCE; (C) and (D) dissolved Fe^{+2}; (E) and (F) Cl^{-}. 3 mM FeS, 22 mM Tris buffer, pH 8. $C_{0,\,TCE}$ =(3.55±0.08) mM, $C_{0,\,PCE}$ =(0.46 ±0.01) mM. Error bars represent the standard deviation of the mean from two independent samples (each independent sample was measured twice). TCE volatilization control in (A) and PCE volatilization

control in (B) were samples containing TCE and PCE only, without FeS, and they were used to monitor volatilization losses. 69

Figure 4.2. XRD patterns of the FeS with TCE sample, the FeS with PCE sample, and the FeS control sample, pH 8, seven weeks. 70

Figure 4.3. Atomic percent of O, Fe, and S. pH 8, seven weeks. Normalized to 100% of the elements reported, unreported elements include C and Cu from the holey carbon grids. EDS does not detect H or He. The error bars represent the standard deviation of several (n) measurements (FeS control, n=16; FeS with TCE, n=12; FeS with PCE, n=16). 72

Figure 4.4. FeS control sample, pH 8, seven weeks. (A), (B) and (C) HRTEM images, and (D) SAED pattern of (A). Diffraction rings produced by mackinawite are marked by Miller indices in orange. In (A) and (B), FeS particles lying with the (001) plane parallel and perpendicular to the TEM grid are indicated by // and ⊥, respectively. 74

Figure 4.5. FeS with TCE sample, pH 8, seven weeks. (A) and (B) HRTEM image; (C) corresponding FFT pattern of (B). (D) SAED pattern of (A); SAED shows the presence of minor greigite (rings produced by mackinawite and greigite are marked by Miller indices in orange and red, respectively). The diffraction maxima of the FFT pattern (C) was indexed to those of FeS and greigite in orange and red, respectively. In (A), FeS particles lying with the (001) plane parallel and perpendicular to the TEM grid are indicated by // and ⊥, respectively. 75

Figure 4.6. FeS with PCE sample, pH 8, seven weeks. (A), (B) and (C) HRTEM images, and (D) SAED pattern of (A). SAED shows the presence of minor greigite (rings produced by mackinawite and greigite are marked by Miller indices in orange and red, respectively). 76

Figure 4.7. The S 2p XPS spectra of FeS surface (peaks correspond to S species), pH 8, seven weeks. (A) FeS control; (B) FeS with TCE; (C) FeS with PCE. Blue dotted lines are experimental data, and yellow lines are corresponding fits. 84

Figure 4.8. The O 1s XPS spectra of FeS surface, pH 8, seven weeks. (A) FeS control; (B) FeS with TCE; (C) FeS with PCE. Blue dotted lines are experimental data, and yellow lines are corresponding fits..... 86

Figure 4.9. The C 1s XPS spectra of FeS surface, pH 8, seven weeks. (A) FeS control; (B) FeS with TCE; (C) FeS with PCE. Blue dotted lines are experimental data, and yellow lines are corresponding fits..... 88

Figure A1. Experimental setup for preparing samples for SEM analysis using FeS chips. CT is transparent and not visible in the photo on the right... 108

Figure A2. Experimental setup for XRD, TEM/SAED, and XPS analyses. .. 109

Figure A3. Plots of $4[CT]_0 - 4[CT]_t - 3[CF]_t$ versus $[Cl^-]$ during CT reduction at (A) pH 7 and (B) pH 8. 0.003 M FeS; 0.022 M Tris buffer; $C_{0,\,CT} = 6\times10^{-4}$ M..... 110

Figure A4. XRD patterns of FeS samples (14 days) (A) pH 7; (B) pH 8. 0.0016 M FeS; 0.022 M Tris buffer; $(2.1\pm0.2)\times10^{-3}$ M CT. Data for mackinawite and greigite are from the International Centre for Diffraction Data (ICDD) powder diffraction file 4+ (PDF4+) database..... 111

Figure A5. Color comparisons of FeS experiment systems and dialysis tubing at 14 days. (A) pH 7; (B) pH 8; (C) dialysis tubing at pH 8. 0.022 M Tris buffer, 0.0016 M FeS, $(2.1\pm0.2)\times10^{-3}$ M CT..... 112

Figure A6. Particles from outside the dialysis tubing after reaction with CT at pH 8 for 14 days. (A) SEM image of particles on filter paper; (B) SAED pattern. 0.0016 M FeS; 0.022 M Tris buffer; $(2.1\pm0.2)\times10^{-3}$ M CT. 113

Figure A7. Eh-pH diagram for the Fe-S-H_2O system at 25°C, assuming ferrihydrite as the ferric (hydr)oxide phase, and $[Fe]_{total} = [S]_{total} = 1.6\times10^{-3}$ M (which equals to the FeS concentration used in experiments for XPS, XRD, TEM, and SAED analyses). Blue lines are boundaries for the stability field of H_2O. 114

Figure A8. FeS(s) concentration as percent of total Fe(II). Total carbonate concentration $[CO_3]_{total} = 10^{-3}$ M, total Fe(II) = 5×10^{-5} M, and total S(-II) = 3×10^{-4} M. Both FeS(s) and $FeCO_3$(s) were considered in the equilibrium calculations, but $FeCO_3$(s) never equaled a value above zero, and is therefore invisible in this figure. Dissolved species are not shown for clarity. 115

Figure B1. Calculation of d-spacing using HRTEM images obtained from FeS with PCE sample using Gatan Microscopy Suite® (version 2.32, Gatan, Inc., Pleasanton, CA). (A) HRTEM image of FeS with PCE, pH 8, seven weeks; (B) intensity profile from the atomic layers shown inside the yellow box in (A)..... 120

Figure B2. SEM images of the surface of FeS control sample, pH 8, 1 hour. 121

Figure B3. SEM images of the surface of FeS control sample, pH 8, 16 days. 122

Figure B4. SEM images of the surface of FeS control sample, pH 8, 32 days. 123

Figure B5. SEM images of the surface of FeS with TCE sample, pH 8, 16 days. 124

Figure B6. SEM images of the surface of FeS with TCE sample, pH 8, 32 days. 125

Figure B7. SEM images of the surface of FeS with PCE sample, pH 8, 16 days. 126

Figure B8. SEM images of the surface of FeS with PCE sample, pH 8, 32 days. 127

Figure B9. Atomic percent of FeS samples (A) FeS control at different times; (B) 16 days, pH 8; (C) 32 days, pH 8 (n=5-7)..... 128

Figure B10. The S 2p XPS spectra of FeS surface (fitted using peaks with binding energies consistent with iron sulfides minerals), pH 8, seven weeks. (A) FeS control; (B) FeS with TCE; (C) FeS with PCE. Blue dotted lines are experimental data, and yellow lines are corresponding fits. 129

Figure B11. The Fe $2p_{3/2}$ XPS spectra of FeS surface, pH 8, seven weeks. (A) FeS control; (B) FeS with TCE; (C) FeS with PCE. 130

ABSTRACT

The overarching objective of this research is to investigate the transformation of iron sulfide, mackinawite (FeS), in contaminated environments. A special research focus is to investigate the FeS oxidation products formed during dechlorination of tetrachloroethylene (PCE), trichloroethylene (TCE) and carbon tetrachloride (CT). The results from this research will enhance the ability to effectively apply FeS in the in situ remediation of contaminated sites by chlorinated aliphatic contaminants.

The transformation of powdered FeS to greigite (Fe_3S_4) and pyrite (FeS_2) under geochemical conditions similar to those in pristine or contaminated aquifers was monitored. To observe the transformation without altering or damaging the crystal structures, FeS particles were immobilized on poly(methyl methacrylate) (PMMA) supports, and mineralogical changes were monitored by scanning electron microscopy with energy dispersive X-ray spectroscopy (SEM/EDS). Powders of FeS immobilized on PMMA supports were placed in aqueous solutions containing polysulfides and mildly elevated temperatures (75-78 ^{o}C) to promote the transformation to greigite and pyrite. SEM/EDS results were consistent with previously reported X-ray diffraction (XRD) analysis that showed the transformation of mackinawite to greigite and pyrite. The similarities in sizes between most crystals over the course of the transformation from mackinawite to pyrite, as well as the coexistence of solids with morphologies and elemental compositions characteristic of mackinawite, greigite, and pyrite, are consistent with a solid state transformation. In some cases, however, much smaller pyrite crystals

were formed, which may have resulted from direct nucleation from solution. The results reported here extend the applicability of PMMA supports for studying mineralogical transformations to particles with dimensions from 100 nm to 2 μm, and to elevated temperatures. Such supports can be used to monitor iron-sulfur mineralogical changes in pristine and contaminated environments.

The FeS oxidation products formed during the reaction between FeS and CT at pH 7 and 8 were studied. XRD analysis suggested the formation of greigite upon reaction of FeS with CT at pH 7. At pH 8, reaction of FeS with CT led to the formation of abundant spherical particles with diameters between 50-400 nm on the FeS surface and in solution; far fewer such particles were observed at pH 7. Analysis of the FeS surface by EDS after reaction with CT at pH 8 showed decreased sulfur and elevated oxygen compared to unreacted FeS. The spherical particles that formed upon FeS reaction with CT were mostly amorphous with localized areas of poorly crystalline two-line ferrihydrite. X-ray photoelectron spectroscopy (XPS) indicated that the predominant Fe surface species after reaction with CT at pH 8 was Fe(III)-O, consistent with ferrihydrite and other amorphous iron (hydr)oxides as major products. No oxidation of sulfide was observed.

The oxidation products of FeS during reaction with TCE and PCE at pH 8 were also investigated. Results indicated that the FeS oxidation products by TCE and PCE were mainly greigite, and non-crystalline iron (hydr)oxides might be another possible product. S species on the FeS surface were oxidized during the dechlorination of TCE and PCE by FeS, while no oxidation of Fe species was observed within the time frame of the study.

This research provides direct evidence for the FeS oxidation products formed during dechlorination of CT, TCE, and PCE using FeS. Both ferrihydrite and Fe^{+2}, which is a product of greigite dissolution, can react with dissolved HS^- to form FeS, suggesting that, after oxidation by chlorinated aliphatic contaminants, FeS can be regenerated by addition or microbial generation of sulfide.

Chapter 1

Introduction

1.1. Formation and structure of mackinawite (FeS)

Iron sulfide minerals are an essential part of the iron cycle and sulfur cycle in the lower temperature environments. Mackinawite, $Fe_{1.00\pm0.01}S$ (Rickard et al., 2006) (referred to as FeS hereafter), is the initially precipitated iron sulfide mineral resulting from the reaction between dissolved Fe(II) and dissolved S(-II) at ambient temperature (Rickard et al., 2006). FeS has a tetragonal layer structure. In a tetragonal cell, one iron atom is linked in a tetrahedral coordination to four equidistant sulfur atoms (Wolthers et al., 2003). A tetrahedron is linked by edge-sharing to four adjacent tetrahedra, and by corner-sharing to four adjacent tetrahedra (Wolthers et al., 2003). These layers are held together by van der Waals forces, and the spacing between the layers is ~5 Å, which is the characteristic peak of FeS observed by X-ray powder diffraction (XRD) (Wolthers et al., 2003; Rickard et al., 2006). There are three commonly used ways to synthesize FeS in the lab: by the reaction of metallic iron with dissolved S(-II) (Mullet et al., 2002); by the reaction of ferrous iron with dissolved S(-II) (Wolthers et al., 2003); and via sulfate-reducing bacteria (Watson et al., 2000).

1.2. Transformation of FeS in natural conditions

FeS is the first crystalline iron sulfide phase formed in the aqueous system, it is highly stable under reducing conditions, and can be transformed into more stable phases under oxidizing conditions. A schematic summary of FeS oxidation products by various environmental species can be found in Figure 1.1. When FeS is exposed

to oxygen, it transforms into greigite (Fe_3S_4) (Boursiquot et al., 2001), goethite (α-FeOOH) (Benning et al., 2000; Boursiquot et al., 2001; Chiriţă et al., 2008), lepidocrocite (γ-FeOOH) (Chiriţå et al., 2008), hematite (α-Fe_2O_3) (Benning et al., 2000) and magnetite (Fe_3O_4) (Boursiquot et al., 2001). FeS can also be oxidized in the anaerobic conditions where other species are available as potential electron acceptors, such as polysulfides (Rickard, 1975), nitrite (Lin et al., 2009) and MnO_2 (Schippers and Jorgensen, 2001). When reacting with polysulfides, FeS undergoes a sulfur-addition transformation to form greigite (Reaction 1.1) (the polysulfide pathway) (Posfai et al., 1998; Benning et al., 2000).

$$3\ FeS(s) + S_n^{2-}(aq) \rightarrow Fe_3S_4(s) + S_{(n-1)}^{2-} \qquad 1.1$$

During this process, two-thirds of Fe(II) atoms in Fe(II)S are oxidized to Fe(III) by S(0) to form greigite ($Fe(II)Fe(III)_2S(-II)_4$), and S(-II) atoms in Fe(II)S remain unoxidized (Rickard and Morse, 2005). In contrast to greigite formation from FeS, pyrite ($Fe(II)S(-I)_2$) formation from FeS requires that the Fe(II) atoms in Fe(II)S remain unoxidized whereas the S(-II) atoms in Fe(II)S are oxidized (Reaction 1.2) (Rickard and Morse, 2005).

$$FeS(s) + S_n^{2-}(aq) \rightarrow FeS_2(s) + S_{(n-1)}^{2-} \qquad 1.2$$

If the sulfur-addition reaction continues after greigite is formed, greigite would continue transforming into pyrite, which is considered to be a stable iron(II) disulfide (Rickard and Luther, 2007). Pyrite formation from greigite requires both the reduction of Fe(III) and the oxidation of S(-II). At ambient temperature, these phase transformations may take months to years (Wang and Morse, 1996; Benning

et al., 2000). In summary, the oxidation products of FeS in natural or pristine environments consist of stable iron oxides and iron sulfides.

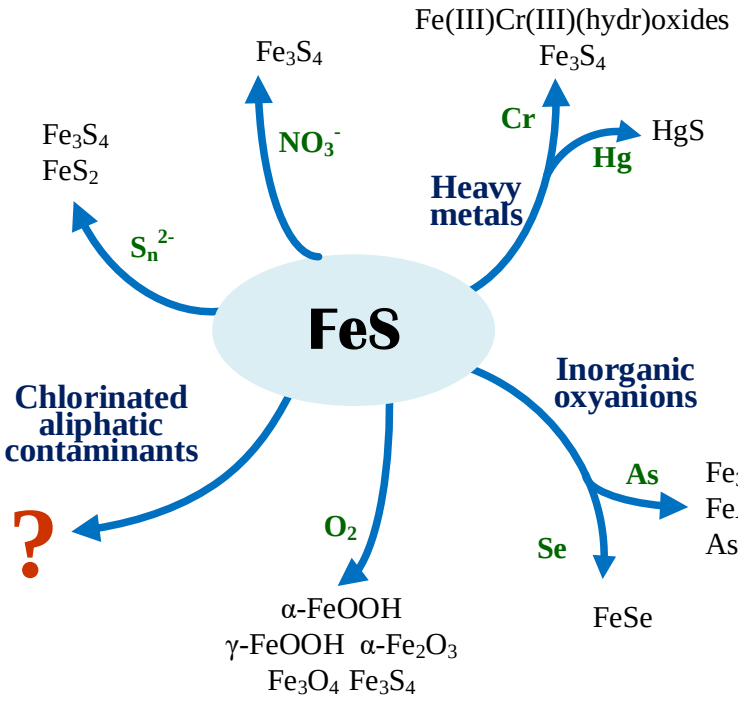


Figure 1.1. A schematic summary of FeS transformation products by various environmental species. References of the transformations showed in the figure can be found in Sections 1.2 and 1.3.

1.3. Transformation of FeS during reaction with contaminants

FeS is a highly reactive phase, and has been applied to the treatment of groundwater contaminants, such as heavy metals, chlorinated aliphatic contaminants, arsenic (As) and selenium (Se) (Gong et al., 2016) (Figure 1.1). Several mechanisms of contaminant removal by FeS have been reported by previous studies. During the reactions with heavy metals, FeS can remove mercury (Hg) through adsorption, precipitation of HgS, as well as the formation of surface complexes (Jeong et al., 2007). Chromium (Cr) (VI) can be reduced by FeS to Cr(III), which is insoluble and

less toxic compared to Cr(VI), accompanied by the formation of greigite and an Fe(III) and Cr(III) (hydr)oxide layer on the FeS surface (Mullet et al., 2004). FeS can also react with inorganic oxyanions, such as As and Se. The removal of As(III) was through the precipitation of AsS (Han et al., 2011b) or FeAsS (Bostick and Fendorf, 2003) at low pH values; whereas, as the pH increases, the As(III) was removed mainly through surface sorption (Han et al., 2011b). During the removal of As(III), FeS was oxidized into greigite (Gallegos et al., 2008). Formation of outer sphere surface complexation was a predominant mechanism of As(V) removal by FeS in aqueous solution (Farquhar et al., 2002; Wolthers et al., 2005), while no redox reaction between As(V) and FeS was reported (Wolthers et al., 2005). Sorption and reduction are also the important mechanisms of the removal of Se by FeS from aqueous solution, and FeSe was found on the FeS surface (Breynaert et al., 2008; Han et al., 2011a). In summary, the FeS-associated products during the reactions with heavy metals and inorganic oxyanions are greigite, sulfide precipitates, and iron (hydr)oxides layers on the FeS surface.

1.4. Dechlorination of Chlorinated Aliphatic Contaminants by FeS

Chlorinated aliphatic contaminants are widespread in soil and groundwater systems. They attract researchers' attention because they persist in soil and water systems, and because of their influences on both acute and chronic human-health problems (Moran et al., 2007). Tetrachloroethylene (PCE), trichloroethylene (TCE) and carbon tetrachloride (CT) are listed among the most frequently detected volatile organic compounds, due to common commercial and industrial usage (Moran et al., 2007). Abiotic dechlorination of CT, TCE, and PCE by FeS has been studied both in

the laboratory and in the field. FeS shows the greatest reactivity of dechlorination among iron minerals, including FeS, green rust, magnetite, and pyrite (He et al., 2015). In engineered groundwater treatment sites, such as permeable reactive barriers and enhanced reductive dechlorination locations, the iron-reducing and sulfate-reducing conditions often favor the formation of FeS. Thus, it is important to study the FeS oxidation products formed during dechlorination of CT, TCE, and PCE by FeS, in order to effectively apply FeS in remediation sites.

The kinetics and reaction pathways of the dechlorination of CT, TCE, and PCE by FeS have been well-studied (Butler and Hayes, 1999; Devlin and Muller, 1999; Butler and Hayes, 2000; Assaf-Anid and Lin, 2002; Zwank et al., 2005; Jeong and Hayes, 2007; Liang et al., 2007). FeS has different reactivity with CT, TCE, and PCE, depending on the pH values and the methods of FeS syntheses. In general, the dechlorination rate of CT by FeS is faster than the dechlorination rates of TCE and PCE by FeS. But the rate comparison between degradation of TCE and PCE by FeS received mixed results (Butler and Hayes, 1999; Liang et al., 2007). The rate constants are strongly dependent on pH, and increase as the pH increases (Butler and Hayes, 2001; Liang et al., 2007). Different preparation methods can also influence the reactivity of FeS. Freeze-dried FeS degraded TCE slower than non-freeze-dried FeS due to the decrease of specific surface area, as well as the mineral transformation introduced by freeze-drying process (He et al., 2010). The dechlorination pathways and organic daughter products of CT, TCE, and PCE by FeS were reviewed carefully by He et al. (2015) and Gong et al. (2016), and were discussed briefly in Chapter 3 and Chapter 4. However, the oxidized products of

FeS by CT, TCE, and PCE during the dechlorination in the abiotic environment are still unclear.

Despite the fact that FeS shows great reactivity in the dechlorination of CT, TCE, and PCE, few field tests have been reported (Kennedy et al., 2006; Shen and Wilson, 2007). In groundwater systems which demonstrate iron- or sulfate-reducing conditions, the formation of FeS is usually favored (Chapelle et al., 2009). By adding iron source, sulfate source, and carbon source to the groundwater systems according to the systems' environmental conditions, the in situ formation of FeS is feasible (Kennedy et al., 2006; Shen and Wilson, 2007; Chapelle et al., 2009; He et al., 2015). For example, Kennedy et al. (2006) reported that during the biogeochemical reductive dechlorination, in the presence of sulfate-reducing soil bacteria, FeS is formed at the expense of native iron minerals. They also did a field test by injecting sulfate salt and sodium lactate into the field, the resulting FeS reduced 95% TCE and PCE in less than 1 year (Kennedy et al., 2006).

In situ remediation using FeS is currently less popular compared to other widely used technologies, for example, in situ remediation using nano zero-valent iron particles. The reliable application of FeS during in situ remediation requires a better understanding of the FeS-associated products formed during the remediation process. This is the driving force of the research presented in this dissertation, which may be condensed into one question: "What are the abiotic products of FeS oxidation by CT, TCE, and PCE?"

1.5. Overview of this dissertation

The overarching objective of this research is to investigate the transformation of FeS in contaminated environments. A special research focus is to characterize the FeS oxidation products formed during reductive dechlorination of CT, TCE, and PCE. To reach this objective, this research is operationally divided into three tasks (Figure 1.2). Each task is addressed in one chapter in the dissertation.

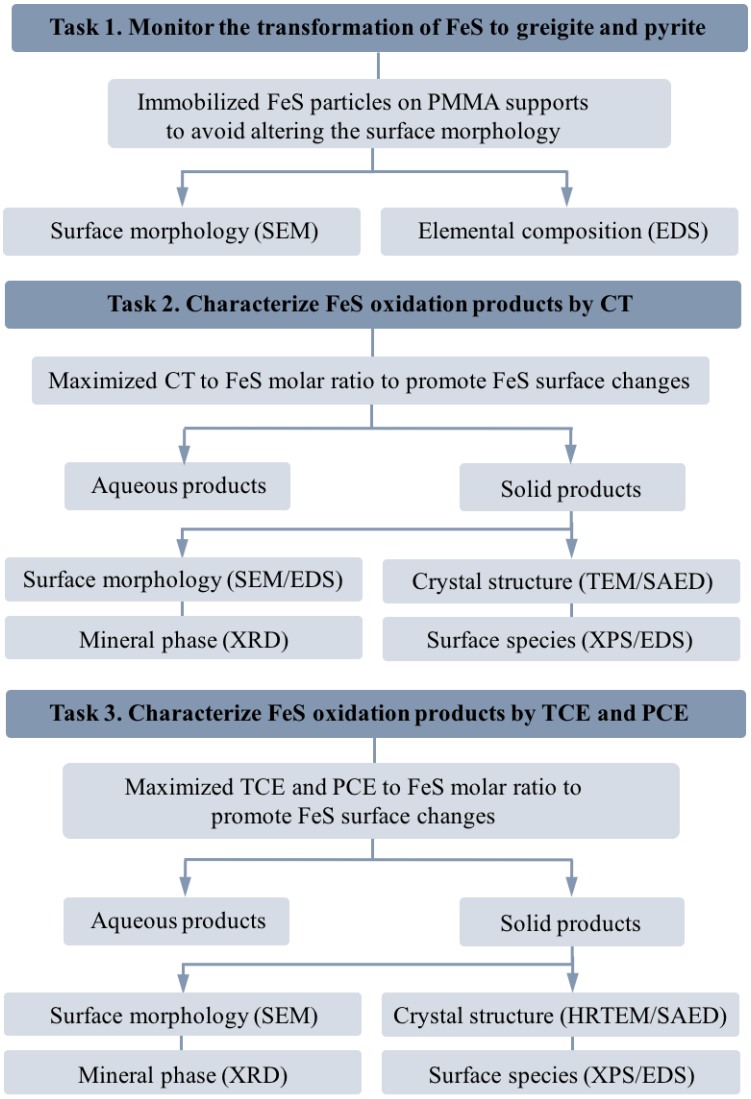


Figure 1.2. Overview of research tasks addressed in this dissertation.

Task 1: Monitor the transformation of FeS to greigite and pyrite under geochemical conditions similar to those in pristine or contaminated aquifers

The reaction pathways of the transformation of FeS to greigite and pyrite have been well-studied (Sweeney and Kaplan, 1973; Rickard, 1975; Benning et al., 2000; Li et al., 2008; Lin et al., 2009). Mineralogical changes during this transformation are typically identified after separations of solids from water by filtration. However, the size and texture of iron crystals are altered by filtration. Impurities and mineral losses are also drawbacks of this treatment. In aquifers and sediments, removal of trace minerals such as FeS for ex situ analyses without altering the minerals' morphology would be a challenge. In this task, FeS particles were immobilized on poly(methyl methacrylate) (PMMA) supports (referred to as "FeS chip" hereafter) in order to overcome the aforementioned drawbacks. Scanning electron microscopy (SEM) was used to monitor the morphology changes during the transformation of FeS to greigite and pyrite. Energy dispersive X-ray spectroscopy (EDS) was used to analyze the elemental composition of the minerals. It was also proved that FeS chips can be used in studying the mineralogical transformation of nanoscale FeS particles. Therefore, they were employed in the next two tasks. Task 1 is addressed in Chapter 2.

Task 2: Characterize the FeS oxidation products formed upon reductive dechlorination of CT

In Task 2, the oxidation products of FeS by CT were studied under experimental conditions that promoted the mineral transformation by maximizing CT to FeS molar ratios. These special setups gave the greatest possibility of

detecting changes on the FeS surface. Two unique and practical experimental setups using FeS chips and FeS particles enclosed in dialysis tubing were employed to recover small amounts of FeS from aqueous solutions. Powder X-ray diffraction (XRD) presented the information of the crystal structure of the minerals, and SEM provided results for morphology changes which occurred on the FeS surface. EDS was used to calculate the elemental composition of the minerals. X-ray photoelectron spectroscopy (XPS) was used as a surface sensitive technique to probe the changes of surface species and chemical states that took place on FeS surface within nanometers deep. Transmission electron microscopy (TEM) with selected area electron diffraction (SAED) was used to identify the morphology and crystal structure of the newly formed mineral products. Task 2 is addressed in Chapter 3.

Task 3: Characterize the FeS oxidation products formed upon reductive dechlorination of TCE and PCE

TCE and PCE are more frequently detected in groundwater system compared to CT (Doherty, 2000a, b; Moran et al., 2007). The oxidation products of FeS by TCE and PCE were investigated in Task 3. The experimental setups and solid analytical techniques used in Task 2 were employed in this task as well. Moreover, high resolution field emission transmission electron microscopy (HRTEM) with SAED was used to collect diffraction patterns and images of the crystal structure of the samples. Task 3 is addressed in Chapter 4.

This study provided the first direct evidence on the FeS-associated products formed during dechlorination of CT, TCE, and PCE using FeS. The conclusions

from Tasks 1, 2, and 3 are summarized in Chapter 5. Important accomplishments are highlighted, and areas for future investigation are identified. Consequently, the results from this work can be applied in groundwater remediation strategies that involve in situ remediation of chlorinated aliphatic contaminants using FeS. The results on the FeS-associated products can also help to assess the ability of FeS to be regenerated under natural conditions.

References

Assaf-Anid, N., and Lin, K.-Y. 2002. Carbon tetrachloride reduction by Fe^{2+}, S^{2-}, and FeS with vitamin B_{12} as organic amendment. *J Environ Eng* 128 (1):94-99.

Benning, L. G., Wilkin, R. T., and Barnes, H. L. 2000. Reaction pathways in the Fe-S system below 100 degrees C. *Chem Geol* 167 (1-2):25-51.

Bostick, B. C., and Fendorf, S. 2003. Arsenite sorption on troilite (FeS) and pyrite (FeS_2). *Geochim Cosmochim Ac* 67 (5):909-921.

Boursiquot, S., Mullet, M., Abdelmoula, M., Genin, J. M., and Ehrhardt, J. J. 2001. The dry oxidation of tetragonal FeS_{1-x} mackinawite. *Phys Chem Miner* 28 (9):600-611.

Breynaert, E., Bruggeman, C., and Maes, A. 2008. XANES-EXAFS analysis of se solid-phase reaction products formed upon contacting Se(IV) with FeS_2 and FeS. *Environ Sci Technol* 42 (10):3595-3601.

Butler, E. C., and Hayes, K. F. 1999. Kinetics of the transformation of trichloroethylene and tetrachloroethylene by iron sulfide. *Environ Sci Technol* 33 (12):2021-2027.

Butler, E. C., and Hayes, K. F. 2000. Kinetics of the transformation of halogenated aliphatic compounds by iron sulfide. *Environ Sci Technol* 34 (3):422-429.

Butler, E. C., and Hayes, K. F. 2001. Factors influencing rates and products in the transformation of trichloroethylene by iron sulfide and iron metal. *Environ Sci Technol* 35 (19):3884-3891.

Chapelle, F. H., Bradley, P. M., Thomas, M. A., and McMahon, P. B. 2009. Distinguishing iron-reducing from sulfate-reducing conditions. *Ground Water* 47 (2):300-305.

Chiriţă, P., Descostes, M., and Schlegel, M. L. 2008. Oxidation of FeS by oxygen-bearing acidic solutions. *J Colloid Interf Sci* 321 (1):84-95.

Devlin, J. F., and Muller, D. 1999. Field and laboratory studies of carbon tetrachloride transformation in a sandy aquifer under sulfate reducing conditions. *Environ Sci Technol* 33 (7):1021-1027.

Doherty, R. E. 2000a. A history of the production and use of carbon tetrachloride, tetrachloroethylene, trichloroethylene and 1,1,1-trichloroethane in the United States: Part 1 - Historical background; Carbon tetrachloride and tetrachloroethylene. *Environ Forensics* 1 (2):69-81.

Doherty, R. E. 2000b. A history of the production and use of carbon tetrachloride, tetrachloroethylene, trichloroethylene and 1,1,1-trichloroethane in the United States: Part 2 - Trichloroethylene and 1,1,1-trichloroethane. *Environ Forensics* 1 (2):83-93.

Farquhar, M. L., Charnock, J. M., Livens, F. R., and Vaughan, D. J. 2002. Mechanisms of arsenic uptake from aqueous solution by interaction with goethite, lepidocrocite, mackinawite, and pyrite: An X-ray absorption spectroscopy study. *Environ Sci Technol* 36 (8):1757-1762.

Gallegos, T. J., Han, Y. S., and Hayes, K. F. 2008. Model predictions of realgar precipitation by reaction of As(III) with synthetic mackinawite under anoxic conditions. *Environ Sci Technol* 42 (24):9338-9343.

Gong, Y. Y., Tang, J. C., and Zhao, D. Y. 2016. Application of iron sulfide particles for groundwater and soil remediation: A review. *Water Res* 89:309-320.

Han, D. S., Batchelor, B., and Abdel-Wahab, A. 2011a. Sorption of selenium(IV) and selenium(VI) to mackinawite (FeS): Effect of contact time, extent of removal, sorption envelopes. *J Hazard Mater* 186 (1):451-457.

Han, Y. S., Jeong, H. Y., Demond, A. H., and Hayes, K. F. 2011b. X-ray absorption and photoelectron spectroscopic study of the association of As(III) with nanoparticulate FeS and FeS-coated sand. *Water Res* 45 (17):5727-5735.

He, Y. T., Wilson, J. T., Su, C., and Wilkin, R. T. 2015. Review of abiotic degradation of chlorinated solvents by reactive iron minerals in aquifers. *Ground Water Monit R* 35 (3):57-75.

He, Y. T., Wilson, J. T., and Wilkin, R. T. 2010. Impact of iron sulfide transformation on trichloroethylene degradation. *Geochim Cosmochim Ac* 74 (7):2025-2039.

Jeong, H. Y., and Hayes, K. F. 2007. Reductive dechlorination of tetrachloroethylene and trichloroethylene by mackinawite (FeS) in the presence of metals: Reaction rates. *Environ Sci Technol* 41 (18):6390-6396.

Jeong, H. Y., Klaue, B., Blum, J. D., and Hayes, K. F. 2007. Sorption of mercuric ion by synthetic manocrystalline mackinawite (FeS). *Environ Sci Technol* 41 (22):7699-7705.

Kennedy, L. G., Everett, J. W., Becvar, E., and Defeo, D. 2006. Field-scale demonstration of induced biogeochemical reductive dechlorination at Dover Air Force Base, Dover, Delaware. *J Contam Hydrol* 88 (1-2):119-136.

Li, Y., van Santen, R. A., and Weber, T. 2008. High-temperature FeS-FeS_2 solid-state transitions: Reactions of solid mackinawite with gaseous H_2S. *J Solid State Chem* 181 (11):3151-3162.

Liang, X., Dong, Y., Kuder, T., Krumholz, L. R., Philp, R. P., and Butler, E. C. 2007. Distinguishing abiotic and biotic transformation of tetrachloroethylene and trichloroethylene by stable carbon isotope fractionation. *Environ Sci Technol* 41 (20):7094-7100.

Lin, S. P., Krause, F., and Voordouw, G. 2009. Transformation of iron sulfide to greigite by nitrite produced by oil field bacteria. *Appl Microbiol Biot* 83 (2):369-376.

Moran, M. J., Zogorski, J. S., and Squillace, P. J. 2007. Chlorinated solvents in groundwater of the United States. *Environ Sci Technol* 41 (1):74-81.

Mullet, M., Boursiquot, S., Abdelmoula, M., Genin, J. M., and Ehrhardt, J. J. 2002. Surface chemistry and structural properties of mackinawite prepared by reaction of sulfide ions with metallic iron. *Geochim Cosmochim Ac* 66 (5):829-836.

Mullet, M., Boursiquot, S., and Ehrhardt, J. J. 2004. Removal of hexavalent chromium from solutions by mackinawite, tetragonal FeS. *Colloid Surface A* 244 (1-3):77-85.

Posfai, M., Buseck, P. R., Bazylinski, D. A., and Frankel, R. B. 1998. Iron sulfides from magnetotactic bacteria: Structure, composition, and phase transitions. *Am Mineral* 83 (11-12):1469-1481.

Rickard, D., Griffith, A., Oldroyd, A., Butler, I. B., Lopez-Capel, E., Manning, D. A. C., and Apperley, D. C. 2006. The composition of nanoparticulate mackinawite, tetragonal iron(II) monosulfide. *Chem Geol* 235 (3-4):286-298.

Rickard, D., and Luther, G. W. 2007. Chemistry of iron sulfides. *Chem Rev* 107 (2):514-562.

Rickard, D., and Morse, J. W. 2005. Acid volatile sulfide (AVS). *Mar Chem* 97 (3-4):141-197.

Rickard, D. T. 1975. Kinetics and mechanism of pyrite formation at low-temperatures. *Am J Sci* 275 (6):636-652.

Schippers, A., and Jorgensen, B. B. 2001. Oxidation of pyrite and iron sulfide by manganese dioxide in marine sediments. *Geochim Cosmochim Ac* 65 (6):915-922.

Shen, H., and Wilson, J. T. 2007. Trichloroethylene removal from groundwater in flow-through columns simulating a permeable reactive barrier constructed with plant mulch. *Environ Sci Technol* 41 (11):4077-4083.

Sweeney, R., and Kaplan, I. 1973. Pyrite framboid formation: laboratory synthesis and marine sediments. *Econ Geol* 68 (5):618-634.

Wang, Q. W., and Morse, J. W. 1996. Pyrite formation under conditions approximating those in anoxic sediments .1. Pathway and morphology. *Mar Chem* 52 (2):99-121.

Watson, J. H. P., Cressey, B. A., Roberts, A. P., Ellwood, D. C., Charnock, J. M., and Soper, A. K. 2000. Structural and magnetic studies on heavy-metal-adsorbing iron sulphide nanoparticles produced by sulphate-reducing bacteria. *J Magn Magn Mater* 214 (1-2):13-30.

Wolthers, M., Charlet, L., Van der Weijden, C. H., Van der Linde, P. R., and Rickard, D. 2005. Arsenic mobility in the ambient sulfidic environment: Sorption of arsenic(V) and arsenic(III) onto disordered mackinawite. *Geochim Cosmochim Ac* 69 (14):3483-3492.

Wolthers, M., Van der Gaast, S. J., and Rickard, D. 2003. The structure of disordered mackinawite. *Am Mineral* 88 (11-12):2007-2015.

Zwank, L., Elsner, M., Aeberhard, A., Schwarzenbach, R. P., and Haderlein, S. B. 2005. Carbon isotope fractionation in the reductive dehalogenation of carbon tetrachloride at iron (hydr)oxide and iron sulfide minerals. *Environ Sci Technol* 39 (15):5634-5641.

Chapter 2 *

Monitoring the Transformation of Mackinawite to Greigite and Pyrite on Polymer Supports

2.1. Introduction

The transformation of the nonstoichiometric iron monosulfide mackinawite (FeS (mk)) to greigite (Fe_3S_4 (gr)) and pyrite (FeS_2 (py)) occurs in aquifers where iron- and sulfate-reducing bacteria create abundant reduced iron and sulfur species. Understanding and monitoring these mineral transformations are critical, since they can strongly influence the stability of chlorinated aliphatic hydrocarbons (U.S. EPA, 2009) and harmful metals (U.S. EPA, 2007) present in contaminated aquifers.

Mild oxidants are required for the transformation of mackinawite to greigite and pyrite, since the oxidation states of the iron and/or sulfur in these minerals are higher than those in mackinawite. Although some researchers (Taylor et al., 1979; Drobner et al., 1990; Rickard, 1997; Rickard and Luther, 1997; Butler and Rickard, 2000) have found that the hydrogen in aqueous H_2S can serve as an oxidant, i.e.,

$$FeS\ (mk) + H_2S = FeS_2\ (py) + H_2 \qquad 2.1$$

a far more commonly reported pathway for the transformation of mackinawite to pyrite is the "polysulfide pathway" (Sweeney and Kaplan, 1973; Luther, 1991; Schoonen and Barnes, 1991; Wilkin and Barnes, 1996; Benning et al., 2000), in

* Reprinted with permission from "Lan, Y. and Butler, E. C. 2014. Monitoring the transformation of mackinawite to greigite and pyrite on polymer supports. *Appl Geochem* 50:1-6". Copyright 2014 Elsevier.

which polysulfides react with mackinawite to form pyrite, sometimes with greigite as an intermediate:

$$3\ FeS\ (mk) + S_n^{2-} = Fe_3S_4\ (gr) + S_{n-1}^{2-} \qquad 2.2$$

$$Fe_3S_4\ (gr) + S_n^{2-} = 3\ FeS_2\ (py) + S_{n-2}^{2-} \qquad 2.3$$

(Sweeney and Kaplan, 1973; Schoonen and Barnes, 1991; Hunger and Benning, 2007).

While pyrite can also form via direct nucleation from solution (Schoonen and Barnes, 1991), evidence for pyrite formation via the solid state transformation of mackinawite and/or greigite includes formation of pyrite framboids on greigite spheres (Sweeney and Kaplan, 1973), formation of pyrite inside mackinawite clusters (Wang and Morse, 1996), formation of greigite on the surface of mackinawite (Herbert et al., 1998), formation of pyrite particles that exhibited ferrimagnetism, suggesting a core of greigite, which is ferrimagnetic (Benning et al., 2000), and kinetic measurements (Hunger and Benning, 2007). For a solid state transformation, Reactions 2.2 and 2.3 above would involve adsorption of polysulfides to mackinawite or greigite, electron transfer to the mineral surface, and atomic rearrangement (Hunger and Benning, 2007). The delocalized electrons in mackinawite may facilitate the initial electron transfer (Devey, 2010). Similarity in size between crystals of the starting (mackinawite) and ending (pyrite) minerals would be consistent with a solid state transformation (Stanton and Goldhaber, 1991), while formation of pyrite crystals much smaller than the mackinawite or greigite precursors would suggest direct crystallization of pyrite from solution (Csakberenyi-Malasics et al., 2012).

Mackinawite crystals can take several forms that reflect its layered structure (Lennie et al., 1995), including irregular, waxy-looking flakes arranged in dense piles or clumps (Benning et al., 2000; He et al., 2008; Csakberenyi-Malasics et al., 2012), irregular clusters (Csakberenyi-Malasics et al., 2012; Lee et al., 2013) and flower shaped "rosettes" (Herbert et al., 1998; Veeramani et al., 2013). Formation of rosettes may be favored at high ionic strength (Herbert et al., 1998). Greigite crystals take many forms, including needles (Horiuchi et al., 1974; Chen et al., 2005; Csakberenyi-Malasics et al., 2012), plates (Horiuchi et al., 1974; Snowball and Thompson, 1988) that can be arranged in flower shapes (Cao et al., 2009), cubooctahedra (Chang et al., 2008), octahedra (Snowball, 1997), and irregular shapes (Hoffmann, 1992; Chen et al., 2005; Csakberenyi-Malasics et al., 2012).

The degree of supersaturation with respect to pyrite, where supersaturation refers to the solution activities of Fe^{+2}, S(-II), and polysulfides in excess of those present in equilibrium with solid pyrite, determines the rate of pyrite formation and the morphology of the resulting crystals (Murowchick and Barnes, 1987). The following sequence of morphologies is typically observed from low to high supersaturation: cubes—including truncated and elongated cubes, cubo-octahedra, octahedra, pyritohedra, and cubo-pyritohedra (Murowchick and Barnes, 1987; Wang and Morse, 1996; Alonso-Azcarate et al., 2001). Needles of pyrite were observed at low supersaturation at temperatures below 250 ^{o}C (Murowchick and Barnes, 1987). Dendrites (Murowchick and Barnes, 1987) and spherulites (Wang and Morse, 1996) were observed at very high saturations. Pyrite framboids form at high

supersaturations when the rate of formation of new pyrite crystals exceeds the rate of growth of existing crystals (Ohfuji and Rickard, 2005).

Mineralogical changes such as Reactions 2 and 3 are typically identified after separation of solids from water by filtration (e.g., Luther (1991);Wilkin and Barnes (1996); Prol-Ledesma et al. (2010)), which may introduce impurities and result in mineral losses. In addition, Benning et al. (2000) reported that filtration altered the size and texture of mackinawite crystals. In aquifers, detection and removal of trace minerals such as mackinawite from the surrounding sediment matrix would likely be an insurmountable challenge, as would monitoring geochemical changes in such trace minerals. To overcome the challenges of monitoring geochemical transformations of trace minerals without altering their morphologies, Birkefeld et al. (2005, 2006, 2007) developed and tested a method for immobilization of mineral particles greater than 20 µm diameter on poly(methyl methacrylate) (PMMA or Plexiglas) chips using epoxy. Such immobilized mineral particles have been found to be stable and durable for up to 18 months buried in soils at a range of pH values (Birkefeld et al., 2005, 2006, 2007; Fakih et al., 2008); PMMA is highly resistant to weathering and is chemically inert with respect to reaction or absorption of contaminants (Birkefeld et al., 2005). Mineralogical changes such as copper slag and lead oxide weathering (Birkefeld et al., 2005, 2006, 2007), iron oxide reductive dissolution (Fakih et al., 2008), and trace arsenic mobilization (Fakih et al., 2008) have been monitored using this technique. The first objective of this study was to apply and test the PMMA supports developed by Birkefeld et al. (2005) under new conditions—specifically, using particles smaller

than 20 μm, different adhesives, and anaerobic conditions. The second objective was to use this method to monitor the transformation of mackinawite to greigite and pyrite under conditions relevant to anaerobic aquifers.

2.2. Materials and methods

2.2.1. Anaerobic conditions

All experimental mixtures were prepared in an anaerobic chamber (Coy Laboratory Products, Inc., Grass Lake, MI) containing a gas mixture of 95 % N_2 and 5 % H_2 and a Pd catalyst to remove trace amounts of oxygen. All aqueous solutions were made with nanopure water (18.0 MΩ-cm resistivity, Barnstead Ultrapure Water System, IA) that had been sparged with N_2 for 30 min, before being transferred to the anaerobic chamber. These solutions as well as solid chemical reagents and glassware were all equilibrated in the anaerobic chamber overnight before use.

2.2.2. Synthesis of mackinawite

Mackinawite was prepared using a method adapted from Rickard (1969) and Butler and Hayes (1998). A total of 1,200 mL of approximately 1.1 M Na_2S was slowly added to 2 L of 0.57 M $FeCl_2$ inside an anaerobic glove bag. The resulting slurry was mixed for 3 days and then decanted into polypropylene bottles that were tightly sealed and centrifuged at 8,000 rpm for 10 min. The supernatant was discarded, and fresh deoxygenated water was added; the bottles were shaken, equilibrated, and centrifuged eight times. Subsequently, the solid was freeze-dried under vacuum. A precipitate prepared by this method was previously characterized

by powder X-ray diffraction (XRD) as poorly crystalline mackinawite (Day 0) (Shao and Butler, 2009) using a Rigaku Max-B instrument (Tokyo, Japan).

2.2.3. PMMA supports

Sheets of PMMA were obtained from Professional Plastics, Inc., Fullerton, CA, then cut into rectangular prisms with dimensions (5 mm × 20 mm × 2.5 mm) chosen to pass through the mouth of a 22 mm dia. serum bottle and to fit into the sample holder for the scanning electron microscope (SEM). In a preliminary test, Loctite Stik'n Seal Outdoor Adhesive (Henkel Corporation, Rocky Hill, CT), a synthetic rubber containing hexane and toluene, was applied to a PMMA support from a squeeze tube, and smoothed flat with the edge of a piece of cardstock. Mackinawite particles were then shaken onto the adhesive-covered PMMA support and left to dry in the anaerobic chamber for two days. The mass of mackinawite on a PMMA support prepared in this way was approximately 0.003 g. Then, the adhesive was tested for durability by putting the mackinawite-coated PMMA support into a serum bottle filled with water for 7 days at room temperature, followed by SEM analysis. After 7 days, most of the particles remained attached to the PMMA surface, yet were not buried or encapsulated by the adhesive, and the supports were free from excess bubbles and holes (Figure 2.1).

2.2.4. Batch experiments

Inside the anaerobic chamber, two PMMA supports containing adhered mackinawite particles were placed in a series of 5 mL serum bottles filled with 5 mL of 0.1 M sulfur (prepared by addition of reagent grade sulfur, Sigma-Aldrich, St. Louis, MO, to nitrogen sparged water), and the final pH was approximately 6. The

solid to solution ratio was 0.006 g immobilized FeS to 5 mL aqueous solution. In the serum bottles, elemental sulfur was expected to react with the dissolved H_2S that was present in equilibrium with mackinawite (from the following dissolution reaction: $FeS + 2\ H^+ = Fe^{+2} + H_2S(aq)$) to produce polysulfides (Giggenba, 1972; Licht et al., 1986). The serum bottles were then sealed inside the anaerobic chamber with Teflon faced butyl rubber septa and aluminum crimp seals, removed from the chamber, and placed in an oven maintained at 75-78 °C for up to 16 days. This time period was more than sufficient for the complete transformation of mackinawite to pyrite (Shao and Butler, 2009). Preparation conditions (i.e., temperature, pH, and sulfur concentration) and reaction time were chosen to promote the transformation of mackinawite to pyrite (Sweeney and Kaplan, 1973; Wang and Morse, 1996; Shao and Butler, 2009) in a reasonable period of time. The formation of greigite and pyrite in the presence of mackinawite has also been observed at ambient temperatures, but typically over significantly longer periods (Rickard, 1969). At periodic time intervals, one bottle was removed from the oven and transferred back into the anaerobic chamber, and the mackinawite loaded PMMA supports were removed, washed three times with nanopure water, then dried in the anaerobic chamber prior to analysis by SEM.

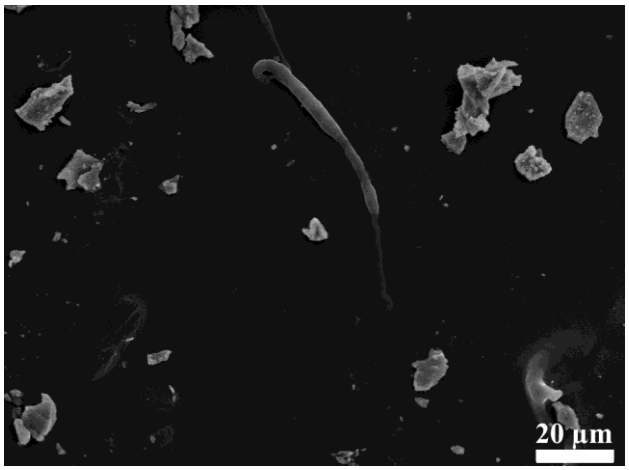


Figure 2.1. SEM image of FeS particles adhered to a PMMA support after being placed in water for 7 days.

2.2.5. SEM, EDS, and XRD analyses

The dried mackinawite loaded PMMA supports were kept in the anaerobic chamber until they were taken to the SEM laboratory in an airtight canning jar filled with a gas mixture of 95 % N_2 and 5 % H_2. The supports were sputter coated with gold and palladium nanoparticles using a Hummer VI triode sputter coater, then transferred immediately into the JEOL JSM-840 SEM operating at 10 or 15 kV. Multiple locations on each PMMA support were scanned, and images of representative spots, i.e., those showing common morphologies and crystal shapes, were collected. Unusual spots were also imaged in some cases. Energy dispersive X-ray spectroscopy (EDS) spectra of selected spots were also collected. Because the samples were unpolished, EDS results should be considered semi-quantitative only. Both PMMA supports from a given serum bottle were examined by SEM.

XRD analyses (previously reported in Shao and Butler (2009)) were performed on separate samples, prepared and treated in solutions with the same

composition, using mackinawite powders (approximately 9 g/L) that were loose in the serum bottles, i.e., not immobilized on the PMMA supports. These differences in experimental conditions (a higher FeS concentration and un-adhered particles) allowed a reasonable XRD signal to noise ratio.

2.3. Results and discussion

Mineralogical changes in the mackinawite particles adhered to the PMMA supports were monitored over time by SEM (Figure 2.2), and structural changes in un-adhered particles were confirmed by XRD (previously reported in Shao and Butler (2009)) There were no noticeable morphological changes between time zero (Figure 2.2a) and day 1 (not shown), but subsequent changes were observed, including formation of small spheres and possibly cubes or octahedra (day 2 (Figure 2.2b)), fine needles or plates (day 3 (Figure 2.2c)), octahedra composed of cubes overlaying morphologically indistinct material (day 5 (Figure 2.2d)), cubes, truncated cubes, and octahedra (days 7 and 9 (Figures 2.2e and 2.2f)), rosettes of flakes, cubes, truncated cubes, and octahedra (day 9, Figures 2.2f and 2.2g), and cubes on a morphologically indistinct background (12 days, Figure 2.2h). Most panels in Figure 2.2 show crystals with similar dimensions, on the order of 2 μm (Figures 2.2d, f, g, h), which is consistent with solid state transformation of mackinawite and not direct crystallization of greigite and pyrite from solution (Stanton and Goldhaber, 1991; Csakberenyi-Malasics et al., 2012).

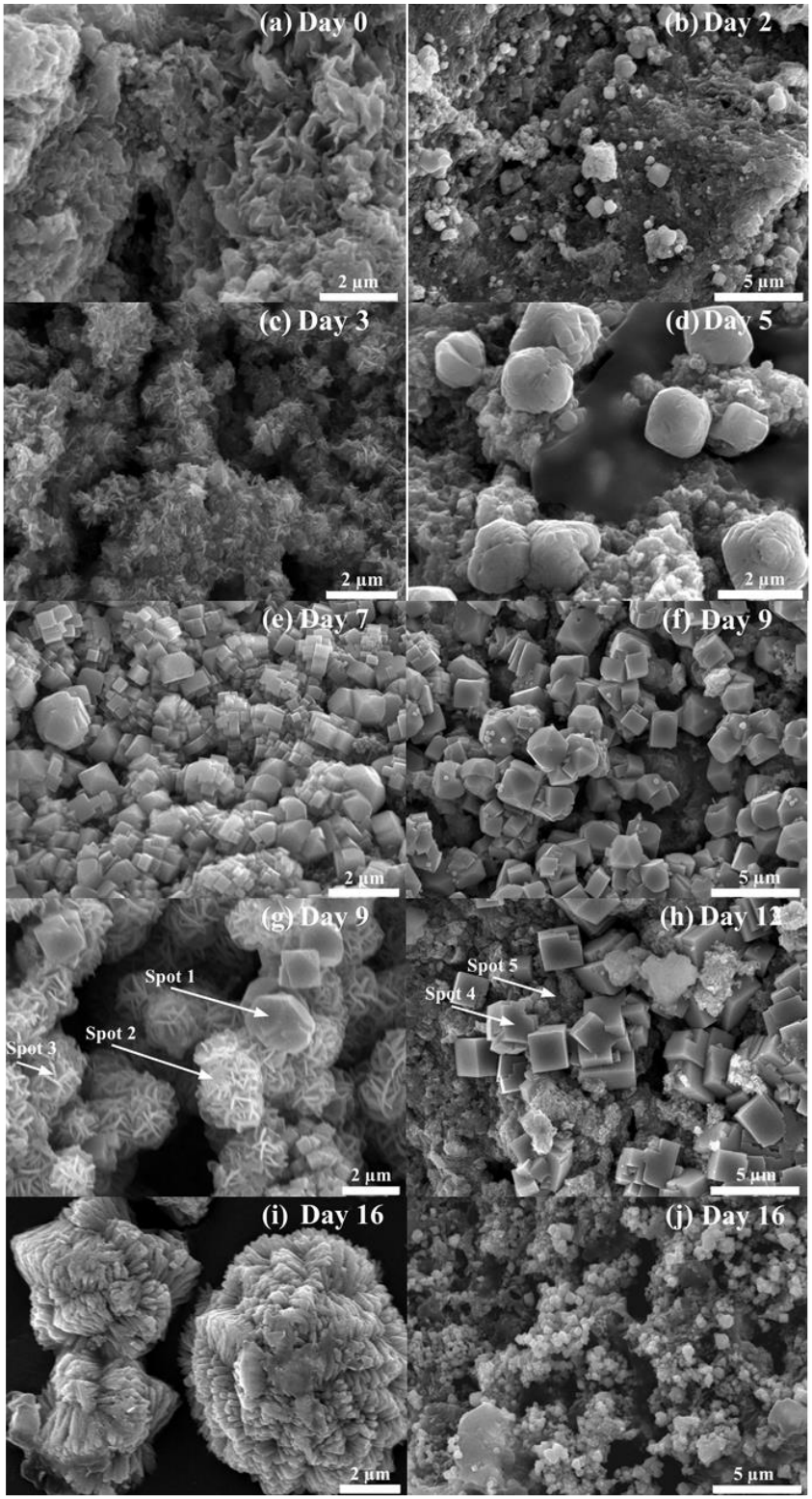


Figure 2.2. SEM images of FeS adhered to PMMA supports after reaction with 0.1 M sulfur at pH 6 and 75-78 ^{o}C.

By days 5, 7, and 9, morphologies consistent with pyrite (cubes, truncated cubes, and octahedra) were abundant (Figures 2.2d, 2.2e, and 2.2f). This is consistent with XRD results that show the transformation of mackinawite to pyrite over approximately five days, with the transient appearance of greigite on day 3 (previously reported in Shao and Butler (2009)). While most day 9 samples with euhedral crystals looked like Figure 2.2f, with regular cubes, truncated cubes, and octahedra, flower-shaped arrangements of flakes or rosettes, were occasionally observed (Figure 2.2g). EDS spot analysis of these rosettes indicated Fe:S ratios (Table 2.1) consistent with pyrite (Spot 2, Figure 2.2g) and mackinawite (Spot 3, Figure 2.2g). Similar flower structures have been reported for mackinawite (Herbert et al., 1998; Veeramani et al., 2013), greigite (Cao et al., 2009), and pyrite (Stanton and Goldhaber, 1991). Spot 1, a truncated cube (Figure 2.2g) had a Fe:S ratio consistent with pyrite (Table 2.1). Cubic crystals with an Fe:S ratio of 1:2.7 were also observed after 12 days (Figure 2.2h, spot 4). These cubes were next to a morphologically indistinct area (Figure 2.2h, spot 5) with an Fe:S ratio consistent with mackinawite or greigite. Together the data suggest transformation of mackinawite to mainly pyrite over 9-12 days, with mackinawite and/or greigite still present at that time. This is generally consistent with the XRD results (previously reported in Shao and Butler (2009)) that reflect average mineral composition, and that would not identify small inclusions of mackinawite and/or greigite at later time periods. The co-location of various forms of iron-sulfur minerals on the PMMA supports is consistent with a solid phase transformation of mackinawite to greigite and pyrite. While EDS spectra also indicated the presence of oxygen in many

samples, it was at molar concentrations less than those of Fe and S (Table 2.1). The presence of oxygen in the samples could be due to transient air exposure during freeze drying or sputter coating, or from the PMMA supports. Crystals typical of iron oxides such as hematite (rhombic) or goethite (needles) were not observed.

Table 2.1. Measured properties of minerals shown in Figure 2.2 (top part of table) and reported or theoretical properties of pure minerals (bottom part of table).

Sample ID	**Spot Number**	**Crystal habit**	**Fe:S:O Molar Ratio (by EDS)**
Day 7 (Fig. 2.2e)	Entire image area	Cube	1:0.8:0
Day 9 (Fig. 2.2g)	1	Truncated cube	1:1.9:0.6
	2	Rosettes of flakes	1:2.2:0.2
	3	Rosettes of flakes	1:1.0:0.8
Day 12 (Fig. 2.2h)	4	Cube	1:2.7:0.1
	5	Morphologically indistinct	1:1.2:0.5
Day 16 (Fig. 2.2i)	Entire image area	Fibrous particles	1:2.5:0
Day 16 (Fig. 2.2j)	Entire image area	Octahedra	1:1.9:0.7
Pure minerals	**Spot number**	**Crystal structure**	**Fe:S:O molar ratio (theoretical)**
Mackinawite	Not applicable	Flakes	Approx. 1:1:0
Greigite	Not applicable	Various	1:1.3:0
Pyrite	Not applicable	Various	1:2:0

Distinct pyrite morphologies were noted in most areas of the day 16 samples. First, clusters or spherulites of fibrous particles (Figure 2.2i) with a Fe:S molar ratio of approximately1:2.5 (Table 2.1) were observed. Wang and Morse (1996) observed spherulites of pyrite with a similar fibrous form at pH 5-6, and reported that they formed under conditions of high supersaturation with respect to pyrite. Second, small grains of less than 100 nm diameter, including octahedra (Figure 2.2j), with a Fe:S molar ratio similar to pyrite (Table 2.1) were also observed. The presence of

these very small crystals with morphologies and Fe:S molar ratios consistent with pyrite at late time periods suggests the possibility that a non-solid-phase pyrite nucleation or crystal growth process occurred in addition to the solid phase transformation of mackinawite described above.

2.4. Conclusions

Monitoring the transformation of mackinawite particles immobilized on PMMA supports allowed collection of varied SEM images of crystals without alteration of their texture or size by pre-imaging preparation steps such as centrifugation or filtration. While the transformation of mackinawite to pyrite was nearly complete over 9-12 days under the conditions of these experiments, EDS results suggest that mackinawite and/or greigite were still present at that time, as has been reported previously (Sweeney and Kaplan, 1973; Wada, 1977; Herbert et al., 1998; Benning et al., 2000; Csakberenyi-Malasics et al., 2012), indicating the coexistence of different iron sulfur mineral phases. While most observed mineralogical changes were consistent with the solid state transformation of mackinawite to greigite and pyrite, the presence of pyrite crystals much smaller than typical precursor mackinawite or greigite crystals at day 16 suggests nucleation of these crystals by a non-solid-state pathway.

This study demonstrates that PMMA supports and commercial adhesives are suitable for studying mineralogical changes in iron-sulfur minerals at mildly elevated temperatures, and that such supports can be used for particles with approximate dimensions ranging from 100 nm to 2 μm. Previous researchers

reported that such a method would not be suitable for particles smaller than 20 µm (Birkefeld et al., 2006), due to complete coating of the particles by adhesive. The experimental setup reported here used can overcome these difficulties. Such PMMA supports can be used to monitor iron-sulfur mineralogical changes in pristine and contaminated environments.

References

Alonso-Azcarate, J., Rodas, M., Fernandez-Diaz, L., Bottrell, S. H., Mas, J. R., and Lopez-Andres, S. 2001. Causes of variation in crystal morphology in metamorphogenic pyrite deposits of the Cameros Basin (N Spain). *Geol J* 36 (2):159-170.

Benning, L. G., Wilkin, R. T., and Barnes, H. L. 2000. Reaction pathways in the Fe-S system below 100 degrees C. *Chem Geol* 167 (1-2):25-51.

Birkefeld, A., Schulin, R., and Nowack, B. 2005. A new in situ method to analyze mineral particle reactions in soils. *Environ Sci Technol* 39 (9):3302-3307.

Birkefeld, A., Schulin, R., and Nowack, B. 2006. In situ investigation of dissolution of heavy metal containing mineral particles in an acidic forest soil. *Geochim Cosmochim Ac* 70 (11):2726-2736.

Birkefeld, A., Schulin, R., and Nowack, B. 2007. In situ transformations of fine lead oxide particles in different soils. *Environ Pollut* 145 (2):554-561.

Butler, E. C., and Hayes, K. F. 1998. Effects of solution composition and pH on the reductive dechlorination of hexachloroethane by iron sulfide. *Environ Sci Technol* 32 (9):1276-1284.

Butler, I. B., and Rickard, D. 2000. Framboidal pyrite formation via the oxidation of iron (II) monosulfide by hydrogen sulphide. *Geochim Cosmochim Ac* 64 (15):2665-2672.

Cao, F., Hu, W., Zhou, L., Shi, W. D., Song, S. Y., Lei, Y. Q., Wang, S., and Zhang, H. J. 2009. 3D Fe_3S_4 flower-like microspheres: High-yield synthesis via a biomolecule-assisted solution approach, their electrical, magnetic and electrochemical hydrogen storage properties. *Dalton T* (42):9246-9252.

Chang, L., Roberts, A. P., Tang, Y., Rainford, B. D., Muxworthy, A. R., and Chen, Q. W. 2008. Fundamental magnetic parameters from pure synthetic greigite (Fe_3S_4). *J Geophys Res-Sol Ea* 113 (B6).

Chen, X. Y., Zhang, X. F., Wan, J. X., Wang, Z. H., and Qian, Y. T. 2005. Selective fabrication of metastable greigite (Fe_3S_4) nanocrystallites and its magnetic properties through a simple solution-based route. *Chem Phys Lett* 403 (4-6):396-399.

Csakberenyi-Malasics, D., Rodriguez-Blanco, J. D., Kis, V. K., Recnik, A., Benning, L. G., and Posfai, M. 2012. Structural properties and transformations of precipitated FeS. *Chem Geol* 294:249-258.

Devey, A. J. 2010. Computer modelling studies of mackinawite, greigite and cubic FeS. UCL (University College London).

Drobner, E., Huber, H., Wachtershauser, G., Rose, D., and Stetter, K. O. 1990. Pyrite rormation linked with hydrogen evolution under anaerobic conditions. *Nature* 346 (6286):742-744.

Fakih, M., Davranche, M., Dia, A., Nowack, B., Petitjean, P., Chatellier, X., and Gruau, G. 2008. A new tool for in situ monitoring of Fe-mobilization in soils. *Appl Geochem* 23 (12):3372-3383.

Giggenba, W. 1972. Optical-spectra and equilibrium distribution of polysulfide ions in aqueous-solution at 20 degrees. *Inorg Chem* 11 (6):1201-1207.

He, Y. T., Wilson, J. T., and Wilkin, R. T. 2008. Transformation of reactive iron minerals in a permeable reactive barrier (biowall) used to treat TCE in groundwater. *Environ Sci Technol* 42 (17):6690-6696.

Herbert, R. B., Pratt, A. R., Blowes, D. W., and Benner, S. G. 1998. Surface oxidation of iron monosulphide: an X-ray photoelectron spectroscopic study. *Mineral. Mag. A* 62:608-609.

Hoffmann, V. 1992. Greigite (Fe_3S_4): magnetic properties and first domain observations. *Phys Earth Planet Inter* 70 (3):288-301.

Horiuchi, S., Wada, H., and Moori, T. 1974. Morphology and imperfection of hydrothermally synthesized greigite (Fe_3S_4). *J Cryst Growth* 24 (Oct):624-626.

Hunger, S., and Benning, L. G. 2007. Greigite: a true intermediate on the polysulfide pathway to pyrite. *Geochem T* 8:1-20.

Lee, S. Y., Baik, M. H., Cho, H. R., Jung, E. C., Jeong, J. T., Choi, J. W., Lee, Y. B., and Lee, Y. J. 2013. Abiotic reduction of uranium by mackinawite (FeS) biogenerated under sulfate-reducing condition. *J Radioanal Nucl Ch* 296 (3):1311-1319.

Lennie, A. R., Redfern, S. A. T., Schofield, P. F., and Vaughan, D. J. 1995. Synthesis and rietveld crystal structure refinement of mackinawite, tetragonal FeS. *Mineral Mag* 59 (397):677-683.

Licht, S., Hodes, G., and Manassen, J. 1986. Numerical-analysis of aqueous polysulfide solutions and Its application to cadmium chalcogenide polysulfide photoelectrochemical solar-cells. *Inorg Chem* 25 (15):2486-2489.

Luther, G. W. 1991. Pyrite synthesis via polysulfide compounds. *Geochim Cosmochim Ac* 55 (10):2839-2849.

Murowchick, J. B., and Barnes, H. L. 1987. Effects of temperature and degree of supersaturation on pyrite morphology. *Am Mineral* 72 (11-12):1241-1250.

Ohfuji, H., and Rickard, D. 2005. Experimental syntheses of framboids - a review. *Earth-Sci Rev* 71 (3-4):147-170.

Prol-Ledesma, R. M., Canet, C., Villanueva-Estrada, R. E., and Ortega-Osorio, A. 2010. Morphology of pyrite in particulate matter from shallow submarine hydrothermal vents. *Am Mineral* 95 (10):1500-1507.

Rickard, D. 1997. Kinetics of pyrite formation by the H_2S oxidation of iron (II) monosulfide in aqueous solutions between 25 and 125 degrees C: The rate equation. *Geochim Cosmochim Ac* 61 (1):115-134.

Rickard, D., and Luther, G. W. 1997. Kinetics of pyrite formation by the H_2S oxidation of iron(II) monosulfide in aqueous solutions between 25 and 125 degrees C: The mechanism. *Geochim Cosmochim Ac* 61 (1):135-147.

Rickard, D. T. 1969. The chemistry of iron sulphide formation at low temperatures. *Stockh Contrib Geol* 20:67-95.

Schoonen, M. A. A., and Barnes, H. L. 1991. Reactions forming pyrite and marcasite from solution. 2. via Fes precursors below 100 Degrees C. *Geochim Cosmochim Ac* 55 (6):1505-1514.

Shao, H. B., and Butler, E. C. 2009. Influence of soil minerals on the rates and products of abiotic transformation of carbon tetrachloride in anaerobic soils and sediments. *Environ Sci Technol* 43 (6):1896-1901.

Snowball, I. F. 1997. The detection of single-domain greigite (Fe_3S_4) using rotational remanent magnetization (RRM) and the effective gyro field (Bg): Mineral magnetic and palaeomagnetic applications. *Geophys J Int* 130 (3):704-716.

Snowball, I. F., and Thompson, R. 1988. The occurrence of greigite in sediments from Loch Lomond. *J Quaternary Sci* 3 (2):121-125.

Stanton, M. R., and Goldhaber, M. B. 1991. An experimental study of goethite sulfidization: relationships to the diagenesis of iron and sulfur. In *Geochemical, Biochemical, and Sedimentological Studies of the Green River Formation, Wyoming, Utah, and Colorado*. U.S. Geological Survey Bulletin.

Sweeney, R., and Kaplan, I. 1973. Pyrite framboid formation: laboratory synthesis and marine sediments. *Econ Geol* 68 (5):618-634.

Taylor, P., Rummery, T. E., and Owen, D. G. 1979. Reactions of iron monosulfide solids with aqueous hydrogen-sulfide up to 160 degrees C. *J Inorg Nucl Chem* 41 (12):1683-1687.

U.S. EPA. 2007. Monitored natural attenuation of inorganic contaminants in ground water, assessment for non-radionuclides including arsenic, cadmium, chromium, copper, lead, nickel, nitrate, perchlorate, and selenium, EPA/600/R- 07/140, vol. 2, Office of Research and Development, National Risk Management Research Laboratory, Cincinnati, Ohio, <http://www.clu-in.org/download/ techfocus/reduction/MNA-inorganics-600R07140.pdf> (accessed 01.08.14).

U.S. EPA. 2009. Identification and characterization methods for reactive minerals responsible for natural attenuation of chlorinated organic compounds in ground water, EPA 600/R-09/115, Office of Research and Development, National Risk Management Research Laboratory, Ada, Oklahoma, <http:// nepis.epa.gov/Adobe/PDF/P1009POU.pdf> (accessed 01.08.14).

Veeramani, H., Scheinost, A. C., Monsegue, N., Qafoku, N. P., Kukkadapu, R., Newville, M., Lanzirotti, A., Pruden, A., Murayama, M., and Hochella, M. F. 2013. Abiotic reductive immobilization of U(VI) by biogenic mackinawite. *Environ Sci Technol* 47 (5):2361-2369.

Wada, H. 1977. The synthesis of greigite from a polysulfide solution at about 100 degree C. *Bull Chem Soc Jpn* 50 (10):2615-2617.

Wang, Q. W., and Morse, J. W. 1996. Pyrite formation under conditions approximating those in anoxic sediments .1. Pathway and morphology. *Mar Chem* 52 (2):99-121.

Wilkin, R. T., and Barnes, H. L. 1996. Pyrite formation by reactions of iron monosulfides with dissolved inorganic and organic sulfur species. *Geochim Cosmochim Ac* 60 (21):4167-4179.

Chapter 3 *

Iron Sulfide Oxidation Products Formed during Reductive Dechlorination of Carbon Tetrachloride

3.1. Introduction

Mackinawite ($Fe_{1+x}S$, where $0 < x < 0.07$) (Vaughan and Craig, 1978), an iron sulfide precipitate formed from dissolved iron and sulfide (Rickard, 1969), is readily oxidized by a variety of natural and anthropogenic species. Oxidation by O_2 transforms FeS into greigite (Fe_3S_4) (Boursiquot et al., 2001; Bourdoiseau et al., 2011), elemental sulfur (Bourdoiseau et al., 2011), goethite (α-FeOOH) (Benning et al., 2000; Boursiquot et al., 2001; Chiriţă et al., 2008; Jeong et al., 2010), lepidocrocite (γ-FeOOH) (Chiriţă et al., 2008; Jeong et al., 2010), hematite (α-Fe_2O_3) (Benning et al., 2000) and magnetite (Fe_3O_4) (Boursiquot et al., 2001). FeS can be oxidized to greigite and pyrite by polysulfides (Sweeney and Kaplan, 1973; Wilkin and Barnes, 1996; Benning et al., 2000; Hunger and Benning, 2007), nitrate produced by oil field bacteria (Lin et al., 2009), chromate (Mullet et al., 2004), and arsenite (Gallegos et al., 2008). Phototrophic iron oxidizing bacteria also oxidize FeS to ferrihydrite concurrent with carbonate reduction (Kappler and Newman, 2004). Several pathways of FeS oxidation have been proposed, including a sulfur addition pathway (Sweeney and Kaplan, 1973; Wilkin and Barnes, 1996; Hunger and Benning, 2007) leading to formation of greigite and pyrite through a solid-state

---

* Reprinted with permission from "Lan, Y. and Butler, E. C. 2016. Iron-sulfide-associated products formed during reductive dechlorination of carbon tetrachloride. *Environ Sci Technol*; DOI 10.1021/acs.est.5b06154" Copyright 2016 American Chemical Society.

mechanism (Hunger and Benning, 2007), and FeS oxidative dissolution, leading to release of Fe(III) that typically precipitates as (hydr)oxides (Buckley and Woods, 1985; Jeong et al., 2010), and enrichment of the FeS surface with S (Buckley and Woods, 1985; Chiriţă et al., 2008).

Mackinawite can also be oxidized by (and thereby reduce) chlorinated aliphatic contaminants such as tetrachloroethylene (PCE), trichloroethylene (TCE), and carbon tetrachloride (CT) (He et al., 2015). The rates and products of chlorinated contaminant reduction by FeS have been carefully studied and compared (He et al., 2015), but the corresponding redox transformation(s) of the FeS surface have not been studied in detail. While He et al. (2010) reported that FeS was transformed into lepidocrocite, goethite, and pyrite by reaction with TCE, they did not determine if such transformations took place in control samples without TCE.

Sulfate- and iron-reducing conditions are often generated in permeable reactive barriers and remediation strategies that promote enhanced abiotic reductive dechlorination (Shen and Wilson, 2007; Air Force Center for Engineering and the Environment, 2008), and favor the formation of FeS (Shen and Wilson, 2007; Chapelle et al., 2009; He et al., 2015; Air Force Center for Engineering and the Environment, 2008). In groundwater systems where dissolved iron or sulfate are limited, the formation of FeS can be achieved by addition of iron (Shen and Wilson, 2007), or sulfur (e.g., magnesium sulfate) to sites with native sulfate reducing soil bacteria (Kennedy et al., 2006). A carbon source (e.g., soybean oil emulsion) can be added when levels of sulfate and iron are high in order to stimulate the formation of FeS (Lee, 2003). However, effective application of FeS in this kind of engineered

remediation system requires an understanding of the FeS-associated products that form during contaminant reductive dechlorination, so that regeneration of FeS can be planned.

The goal of this study was to identify the FeS-associated products formed during reductive dechlorination of CT by FeS. CT was selected for study because it reacts with FeS faster than other common groundwater contaminants such as PCE or TCE (He et al., 2015) allowing completion of a series of experiments in a short time. Both the rate of FeS-mediated reductive dechlorination of CT (Devlin and Müller, 1999) and the products that form when FeS is oxidized by O_2 (Buckley and Woods, 1985; Jeong et al., 2010) vary with pH. Based on this, we hypothesized that the FeS-associated products formed upon reaction with CT would also vary with pH, and thus two environmentally-relevant pH values (7 and 8) were studied.

3.2. Material and methods

3.2.1. General experimental conditions

Unless otherwise noted, all experimental procedures were done in an N_2-filled glove bag (108D X-27-27, Glas-Gol, LLC., Terre Haute, IN) or in an anaerobic chamber (Coy Laboratory Products, Inc., Grass Lake, MI), containing a gas mixture of 95 % N_2 and 5 % H_2 and a Pd catalyst for trace oxygen removal. All aqueous solutions were made with nanopure water (18.0 MΩ-cm resistivity, Barnstead Ultrapure Water System, IA). All liquids (nanopure water, methanol) were sparged with N_2 for 40 min prior to being transferred to the anaerobic chamber and used in experiments. N_2-sparged CT was used in all experiments involving pure

phase CT in excess of its aqueous solubility, since these experiments required addition of a relatively large volume of CT (see below). For experiments where a small total volume of CT was added from a stock solution prepared in N_2-sparged methanol to yield dissolved CT, the CT was not sparged. Using a Henry's law constant for O_2 in CT of 0.06 M atm^{-1} (estimated from Metschl (1924) and Bakalyar et al. (1978)) and the partial pressure of O_2 in air, the calculated final dissolved O_2 concentration in these experiments was 7.3×10^{-7} M, which was more than 10^3 times lower than the FeS concentration, and approximiately 10^3 times lower than the CT concentration, making it insignificant.

FeS was prepared using a method from Rickard (1969) described in the Appendix A1. Tris(hydroxymethyl)aminomethane (Tris) buffer, adjusted with 0.1 M HBr, was used to maintain the solution pH at either pH 7 or 8. The final concentration of the Tris buffer was 0.022 M in all experiments. Sulfur-free Tris was chosen as a pH buffer to avoid interference in XPS analysis of the sulfur 2p electron. HBr was chosen instead of HCl for pH adjustment to allow chloride quantitation.

The goal in all experiments was to maximize the ratio of CT to FeS in order to have the greatest probability of detecting changes at the FeS surface due to reaction with CT. Thus the maximum aqueous concentration of CT and the minimum possible amount of FeS were used in all experiments. This required use of special procedures to recover small amounts (e.g., mg/L) of FeS from aqueous solutions. Furthermore, different experimental setups and slightly different concentrations of CT and FeS were employed for measuring (1) the kinetics of CT

removal and formation of dissolved species, and (2) FeS surface changes using scanning electron microscopy with energy dispersive X-ray spectroscopy (SEM/EDS), transmission electron microscopy (TEM), powder X-ray diffraction (XRD), and X-ray photoelectron spectroscopy (XPS). The concentrations of CT and FeS in all experiments are described below and summarized in Table A1. In all cases, samples that were otherwise identical, but that contained no CT (referred to below as "no-CT controls"), were prepared and analyzed alongside samples with CT to ensure that any observed FeS mineral changes could be attributed to reaction with CT.

3.2.2. Experiments to measure dissolved species over time

Nine mL serum bottles containing 0.003 M FeS in Tris buffer were spiked with a stock solution of 0.1 M CT in methanol to yield a final CT concentration of 6×10^{-4} M CT and minimal headspace. After CT addition, serum bottles were immediately crimp-sealed with Teflon-lined rubber stoppers and aluminum crimp seals and shaken until sampling on a rocking platform shaker (45 rocks per minute). The final concentration of methanol in the samples was 0.56% (v/v).

Prior to analysis for CT, chloroform (CF), dissolved Fe^{+2}, Cl^-, and dissolved S(-II), serum bottles were centrifuged at 615 × g for 20 min, then filtered using a Puradis™ 25 mm disposable filter (0.1 μm polyethersulfone membrane with polypropylene housing, Whatman, Piscataway, NJ). CT and CF were measured by gas chromatography as described in the SI. Forty μL of the filtered supernatant were used to measure dissolved Fe^{+2} using a ferrozine assay (Lovley and Phillips, 1986). Dissolved S(-II) was quantified with an Ag/Ag_2S electrode (Orion 9616BN) using

sulfide antioxidant buffer (containing 2.5 M sodium hydroxide, 0.2 M ethylenediaminetetraacetic acid disodium salt, and 0.2 M L-ascorbic acid). All samples were analyzed for chloride, and samples at the end of each experiment were analyzed for sulfate, both by ion chromatography (Shao and Butler, 2009).

3.2.3. Experiments for FeS mineral characterization

Samples of FeS intended for SEM/EDS analysis were prepared by adhering approximately 0.002 g of dried FeS particles to a 5×20×2.5 mm poly(methyl methacrylate) (PMMA or Plexiglas) chip with Loctite Stik'n Seal Outdoor Adhesive (a synthetic rubber containing hexane and toluene, Henkel Corporation, Rocky Hill, CT) (Birkefeld et al., 2005; Lan and Butler, 2014). These Plexiglas chips with attached FeS particles are referred to below as "FeS chips". The adhesive layer on the FeS chips was thin enough so the majority of the FeS particle surface was exposed to the aqueous solution.

After preparation, one FeS chip was carefully placed with the adhered FeS particles facing up in a 9 mL serum bottle containing 7 mL Tris buffer and a 1 cm layer of glass beads (dia. 3 mm, Fisher Scientific, Pittsburgh, PA). Nanopure water was then added to fill the serum bottle. Then, 50 μL N_2-sparged CT were added to the bottom of the serum bottle without touching the FeS chip using a syringe, and the serum bottle was immediately crimp-sealed and placed without stirring in the anaerobic chamber until the desired sampling time. Serum bottles were not stirred to avoid disturbing this delicate setup. The glass beads prevented direct contact between the particles on the FeS chip and the pure CT phase. The setup (illustrated in Figure A1) allowed undisturbed recovery of a very small mass of FeS particles on

Plexiglas chips that could be directly analyzed by SEM (Lan and Butler, 2014) , and allowed the maximum possible dissolved CT concentration in water. The final dissolved CT concentration in these experiments was $(2.1\pm0.2)\times10^{-3}$ M (determined from the mean of four independent measurements, with the uncertainty corresponding to the standard deviation of the mean), and the estimated FeS concentration was 0.003 M.

One FeS chip, equilibrated in pH 8 buffer without CT for 1 hour, was designated the "time zero" sample. On days 2, 7, and 14, the serum bottles were opened, and the FeS chips (both those with CT and the no-CT controls) were washed with nanopure water three times and left to dry inside the anaerobic chamber. After drying, the chips were transferred to the SEM lab in an air-tight jar, coated with iridium (Ir), and immediately analyzed using a Zeiss NEON high resolution field emission SEM at 10 kV.

FeS particles adhered to Plexiglas chips could not be analyzed by XPS and XRD due to interference from the Plexiglas. So, in order to facilitate recovery of a very small mass of FeS for subsequent XPS and XRD analyses (at least 0.1 g), another set of experiments was done with a small mass of FeS particles enclosed in dialysis tubing in an aqueous CT solution. Specifically, two pieces of 3/8" dialysis tubing (molecular weight cutoff 12,000-14,000 Daltons, Carolina Biological Supply Company, Burlington, NC), together containing a total volume of 7.5 mL 0.2 M FeS slurry (synthesized by mixing 3.75 mL of 0.4 M Na_2S and 3.75 mL of 0.4 M $FeCl_2$ solutions) were prepared inside a glove bag using a pipette. Two short (30 cm) pieces of dialysis tubing were used instead of one long piece for easier handling.

Next, the dialysis tubing was placed in approximately 150 mL Tris buffer (0.022 M) to remove background salts for at least 2 hours before decanting and adding fresh buffer; this step was done three times. Then, the dialysis tubing containing FeS was placed inside a 1 L bottle, modified by a glassblower to have a serum bottle closure, which contained 7.6 mL of pure CT covered by 150 mL of glass beads (Figure A2). The serum bottle was then filled with Tris buffer, leaving no more than approx. 2 mL headspace, crimp-sealed, and kept in the anaerobic chamber without stirring. The total aqueous volume in the serum bottle was 940 mL, including the volume both inside and outside the dialysis tubing. This setup gave a very low FeS concentration of 0.0016 M and a dissolved CT concentration of $(2.1\pm0.2)\times10^{-3}$ M, and allowed recovery of the small mass of FeS particles in the dialysis tubing at the end of the experiment.

After 14 days of reaction between FeS and CT using this setup, we noticed that rust-colored particles formed outside the dialysis tubing at pH 8 (Figure A5B). Thus, at 14 days, the serum bottles at pH 7 and pH 8 were opened inside a glove bag placed in a fume hood (to limit researchers' exposure to volatile CT). The particles inside (at both pH 7 and pH 8) and outside the dialysis tubing (at pH 8 only) were collected separately, transferred to secondary containers, and settled by gravity. For both kinds of particles, the supernatant was removed, and nanopure water was used to wash the particles three times to remove background salts, all inside the glove bag. The particles were transferred into the anaerobic chamber using airtight jars, then centrifuged at 7200 × g for 30 min using a microcentrifuge (Labnet International Inc., Edison, NJ), decanted, and dried. The particles that formed both inside (at both

pH 7 and pH 8) and outside the dialysis tubing (at pH 8 only) were then separately analyzed by XRD using a zero-background holder. Details of XRD analyses are in the SI. In addition, a few drops of the particle-rich suspension that formed outside the dialysis tubing at pH 8 were placed on a holey-carbon grid, dried, and analyzed using a JEOL 2000-FX intermediate voltage TEM capable of selected area electron diffraction (SAED) at 200 kV. About 100 mL of particle-rich solution from outside the dialysis tubing at pH 8 were filtered through a Supor® PES membrane disc filter (0.1 μm, Pall Corp., Port Washington, NY), transferred into the anaerobic chamber using airtight jars, dried, and analyzed using SEM as described above. Finally, the FeS inside the dialysis tubing after reaction with CT at pH 8 was analyzed using XPS, along with a no-CT control, by Evans Analytical Group (East Windsor, NJ). Details are provided in the Appendix A5.

3.3. Results and discussion

3.3.1. Kinetics of CT transformation by FeS

Although the kinetics of CT transformation by FeS have already been studied (He et al., 2015), we quantified CT as a function of time in this study in order to: (1) obtain CT reaction profiles relevant for the experimental conditions used here (i.e., the highest possible ratio of CT to FeS) and (2) simultaneously measure possible dissolved inorganic reaction products such as Fe^{+2} and HS^{-} that might give insight into the products formed at the FeS surface. Measurement of CF was easily accomplished using the same GC method used for CT, so CF data were also collected. No dichloromethane (DCM), which is the product of CF

hydrogenolysis, was detected in the samples, which is not surprising since the pseudo first order rate constant for FeS-mediated reductive transformation of CT is 77 times greater than that for CF (Kenneke and Weber, 2003). A chloride mass balance (Figure A3) indicated that the majority of the CT transformation products were completely dechlorinated (see the Appendix A3 for details). Other documented products of CT reductive dechlorination by FeS and related minerals include carbon monoxide (CO), formate ($HCOO^-$), and carbon disulfide (CS_2), which readily transforms to carbon dioxide (Criddle and McCarty, 1991; Kriegman-King and Reinhard, 1992; Kenneke and Weber, 2003; Shao and Butler, 2009). Products such as these were likely formed in the experiments described here.

As expected (Devlin and Müller, 1999), the transformation of CT by FeS was faster at pH 8 than at pH 7 (Figures 3.1A and 1B). After 14 days, the concentrations of CT and the product CF both appeared to approach a constant level at both pH 7 and 8, (Figures 3.1A and 1B), suggesting the end of the CT dechlorination reaction and completion of any changes to the FeS mineral caused by reaction with CT. Thus, samples for dissolved and solid species characterization were collected from zero to fourteen days.

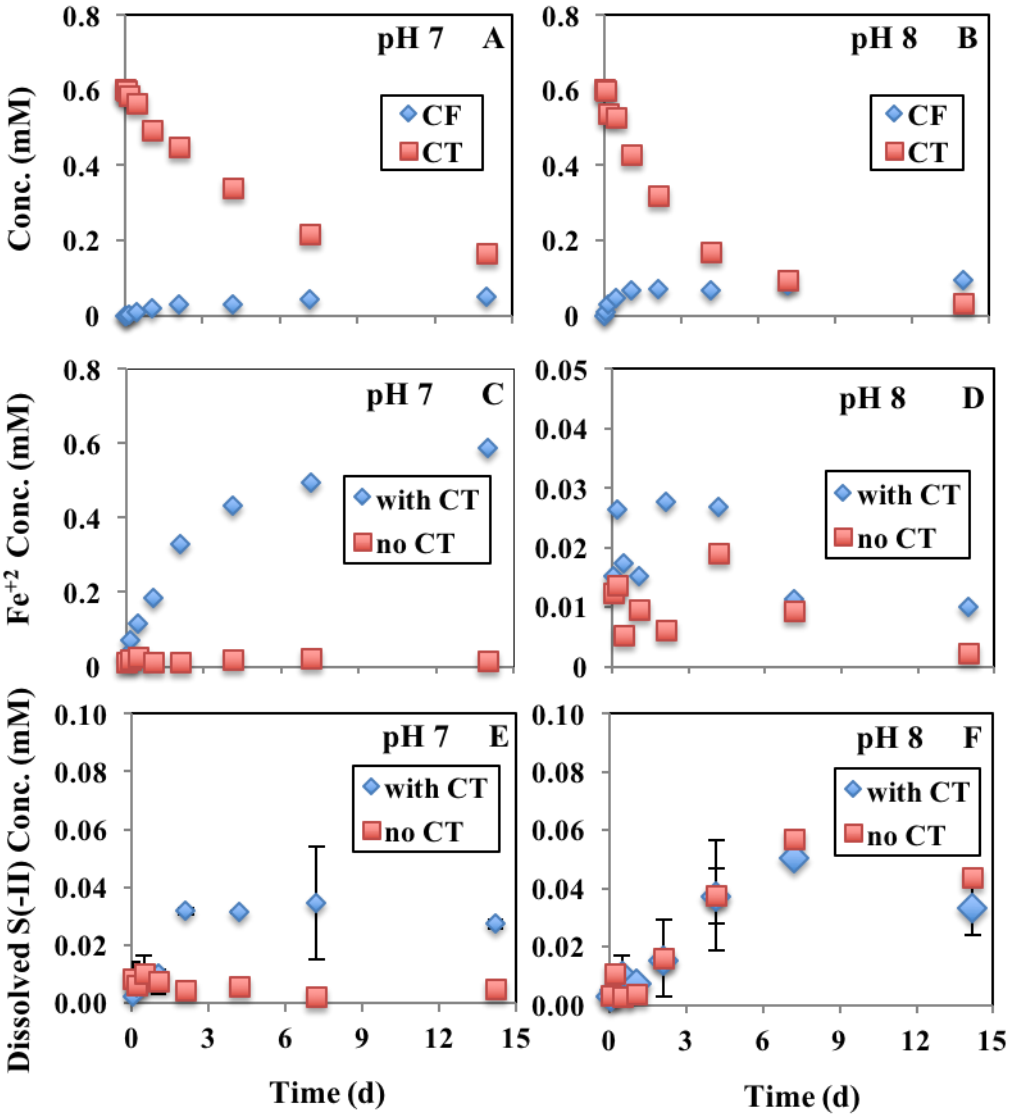


Figure 3.1. Aqueous concentration changes during reaction of FeS with CT. (A, B) CT and CF; (C, D) dissolved Fe^{+2}; (E, F) dissolved S(-II); 0.003 M FeS; 0.022 M Tris buffer; C0, CT =6×10^{-4} M. Error bars (panels E and F) represent the standard deviation of the mean from duplicate analyses. For other parameters (panels A-D), measurements typically agreed within 5%.

At pH 7, dissolved Fe^{+2} increased with time in the sample with CT but not in the no-CT control (Figure 3.1C), indicating that Fe^{+2} was a product of CT reaction with FeS. Transformation of FeS by CT to produce Fe^{+2}, greigite (Fe_3S_4), and other

known CT reaction products (CF (i.e., $CHCl_3$), CO, $HCOO^-$, and CS_2) could take place by FeS oxidative dissolution, as shown below:

$$CCl_4 + 4\ FeS + H^+ \rightarrow Fe_3S_4(s) + CHCl_3 + Fe^{+2} + Cl^- \quad 3.1$$

$$CCl_4 + 4\ FeS + H_2O \rightarrow Fe_3S_4(s) + CO + Fe^{+2} + 4\ Cl^- + 2\ H^+ \quad 3.2$$

$$CCl_4 + 4\ FeS + 2\ H_2O \rightarrow Fe_3S_4(s) + HCOO^- + Fe^{+2} + 4\ Cl^- + 3\ H^+ \quad 3.3$$

$$CCl_4 + 2\ FeS \rightarrow CS_2 + 2\ Fe^{+2} + 4\ Cl^- \quad 3.4$$

In each of these reactions, the positive charge gained by FeS when it donates electrons to CT is balanced by the loss of Fe^{+2} to solution, similar to the well-known oxidative dissolution of FeS by O_2 (Buckley and Woods, 1985; Jeong et al., 2010). Although dissolved Fe^{+2} is rapidly oxidized by dissolved O_2 at pH 7 (Millero, 1985) , CT reacts with dissolved Fe^{+2} very slowly (Curtis and Reinhard, 1994); thus, the Fe^{+2} formed via FeS oxidative dissolution by CT (i.e., via Reactions 3.1-3.4) would be expected to persist in solution at pH 7, which we observed (Figure 3.1C).

Unlike at pH 7, at pH 8 there was no clear difference in dissolved Fe^{+2} over time between samples with CT and the no-CT controls (Figure 3.1D), meaning that either Fe^{+2} was not a product of the reaction between CT and FeS at pH 8, or that if it was a product, it did not remain in solution. Stoichiometry indicates that the solubility of Fe^{+2} with respect to the ferrous hydroxide $Fe(OH)_2(s)$ is 100 times lower at pH 8 compared to pH 7, consistent with precipitation of Fe^{+2} at pH 8. Moreover, the FeS surface is expected to have a greater negative (or less positive) charge at pH 8 versus pH 7 (Wolthers, 2003), so any Fe^{+2} formed by reactions such as 3.1-3.4 above could also have been removed by adsorption at pH 8.

While dissolved S(-II) was clearly a product of the reaction between FeS and CT at pH 7 (Figure 3.1E), at pH 8, there was no difference in dissolved S(-II) over time for the FeS sample that reacted with CT versus the no-CT control (Figure 3.1F). In fact, dissolved S(-II) increased slightly in both the sample with CT and the no-CT control over time at pH 8 (Figure 3.1F), which may have been due to the dissolution or aging of FeS over time. The dissolved S(-II) formed at pH 7 could be due to a reaction such as 3.5 or 3.6, where $Fe(OH)_3(s)$ represents 2-line ferrihydrite (Majzlan et al., 2004).

$$CCl_4 + 2\ FeS + 6\ H_2O \rightarrow 2\ Fe(OH)_3(s) + CHCl_3 + 3\ H^+ + 2\ HS^- + Cl^- \qquad 3.5$$

$$CCl_4 + 2\ FeS + 7\ H_2O \rightarrow 2\ Fe(OH)_3(s) + CO + 6\ H^+ + 2\ HS^- + 4\ Cl^- \qquad 3.6$$

(Reactions 3.5 and 3.6 could also be written showing H_2S as a product instead of HS^-; both are present at approximately equal concentrations at pH 7.). Like Reactions 3.1-3.4, Reactions 3.5 and 3.6 are oxidative dissolution reactions, in which the positive charge gained when FeS donates electrons to CT is balanced by loss of both Fe^{+3} or its hydrolysis product (since Fe^{+3} hydrolysis yields protons). The dissolved Fe(III) thus formed would precipitate at neutral pH to form a Fe(III) (hydr)oxide such as ferrihydrite (Janney et al., 2000). Fe(III) (hydr)oxides are reported to be the oxidation products of FeS minerals oxidation by O_2 (Buckley and Woods, 1985; Pratt et al., 1994; Mycroft et al., 1995; Boursiquot et al., 2001; Jeong et al., 2010; Bourdoiseau et al., 2011). Unlike oxidation of FeS by O_2 (Pratt et al., 1994; Jeong et al., 2010), however, oxidation of FeS by CT yielded no dissolved sulfate.

3.3.2. Characterization of the FeS surface after reaction with CT

In initial SEM analyses, more surface changes were noted at pH 8 than at pH 7, so many subsequent analyses focused on the reaction of FeS with CT at pH 8. First, EDS was done on randomly selected areas on the FeS chips to determine the elemental composition of the particles. The atomic ratios of S and O in the samples were then calculated using the Fe atomic percentage as a reference. For example, the relative ratio of Fe to S in the sample, referred to as "Fe:S" below, is defined as $\left(\frac{\%\,\mathrm{Fe}}{\%\,\mathrm{Fe}}\right):\left(\frac{\%\,\mathrm{S}}{\%\,\mathrm{Fe}}\right)$, where "% Fe" and "% S" are the Fe and S atomic percentages in the sample, respectively.

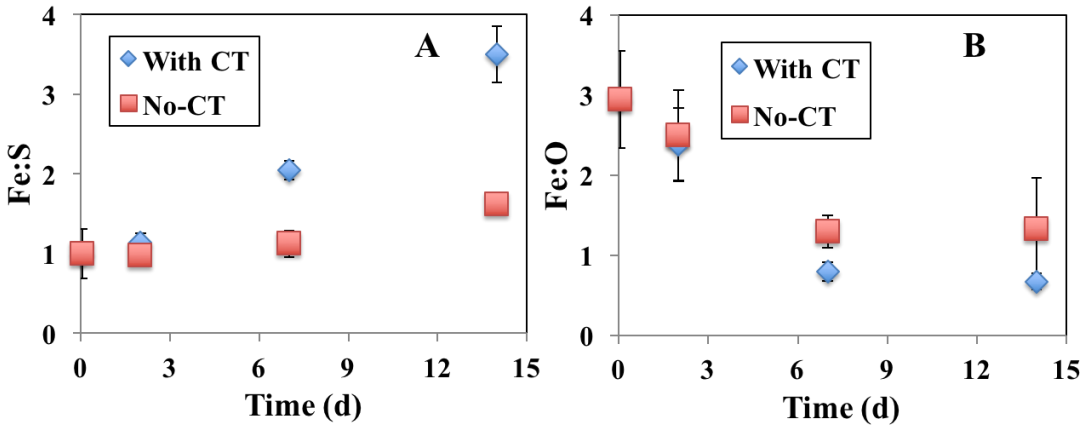


Figure 3.2. Changes in Fe:S and Fe:O during reaction with CT at pH 8; (A) Fe:S and (B) Fe:O. See text for definition of Fe:S and Fe:O. The error bars represent the standard deviation of seven measurements. Conditions: 0.022 M Tris buffer, 0.003 M FeS, $(2.1\pm0.2)\times10^{-3}$ M CT.

In agreement with the stoichiometry of FeS, the value of Fe:S for the no-CT control was 1:(1±0.1) (Figure 3.2A), where the uncertainty in $\left(\frac{\%\,\mathrm{S}}{\%\,\mathrm{Fe}}\right)$ represents the

standard deviation of seven EDS measurements from different areas on the FeS chips. In the no-CT control, the Fe:S value (Figure 3.2A) remained nearly constant over time, but the value of Fe:O (Figure 3.2B) decreased, indicating enrichment with O compared to Fe, which may be due to the development of a (hydr)oxide coating on FeS surface through the interaction with water. Both the increase in Fe:S and the decrease in Fe:O were more substantial in the FeS samples with CT than in the no-CT controls at pH 8 (Figure 3.2); thus these changes in composition can be attributed to reactions with CT. The increase in the relative proportion of O and decrease in the relative proportion of S after reaction with CT could be explained by the formation of a Fe(III) (hydr)oxide on the FeS surface through a reaction such as 3.5 or 3.6.

At pH 7, both the no-CT control and the FeS sample that was exposed to CT were morphologically indistinct by SEM (Figures 3.3A and 3.3B). At pH 8, the no-CT control also had a morphologically indistinct surface after 14 days (Figure 3.3C), but the FeS sample that reacted with CT at pH 8 had clusters of spherical particles with diameters between approximately 50 and 200 nm after 14 days (Figure 3.3D). These clusters appeared to be on top of areas that were otherwise similar in appearance to the no-CT controls. Such spherical particles were observed in most areas of the FeS sample at pH 8 (for example, in ten out of ten randomly selected areas imaged by SEM), but were only occasionally observed at pH 7 (for example, in one or two out of ten randomly selected areas), suggesting they were more abundant at pH 8 than at pH 7.

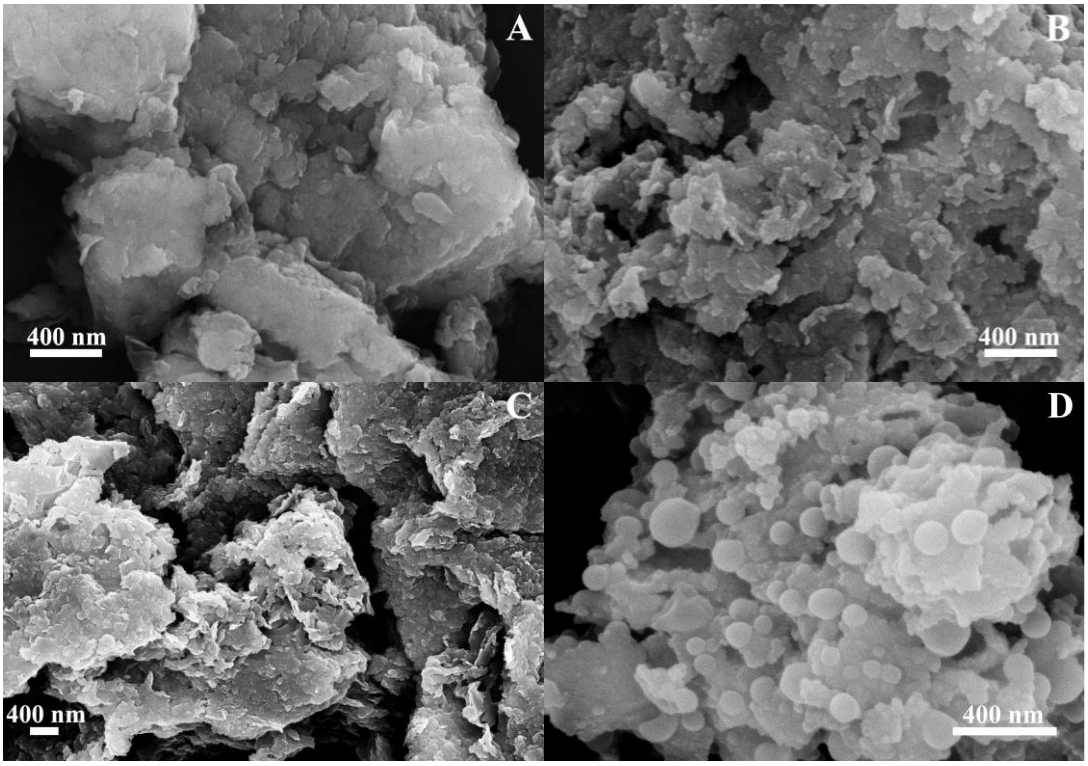


Figure 3.3. SEM images of FeS at 14 days (A) FeS, no-CT control, pH 7; (B) FeS with CT, pH 7; (C) FeS, no-CT control, pH 8; (D) FeS with CT, pH 8. All samples had 0.022 M Tris buffer, 0.003 M FeS, and $(2.1\pm0.2)\times10^{-3}$ M CT.

There were also small differences in the XRD pattern of the FeS samples exposed to CT for 14 days (Figure A4). Small peaks consistent with greigite at $2\theta \approx$ 25 degrees and 36 degrees were present in the XRD pattern of the FeS sample that had reacted with CT at pH 7, but not the no-CT control (Figure A4). For both pH values, the broadening of the peaks at $2\theta \approx 16$, and the increased peak intensity at 52 degrees in FeS samples exposed to CT compared to the peaks in FeS no-CT control, may also be due to the contribution of greigite (Figure A4). The peak broadening in the samples with CT could also be due to oxidative dissolution and size reduction.

Oxidation of FeS to greigite by CT at pH 7 is consistent with our detection of dissolved Fe^{+2} in the reaction of FeS with CT at pH 7 (Figure 3.1C), and might

proceed via a reaction such as 3.1-3.4. The transformation of mackinawite to greigite is a solid state reaction (Hunger and Benning, 2007), in which the structural arrangement of S atoms is maintained, but a fraction of Fe atoms are lost by diffusion to the surface and dissolution, and a fraction of the remaining structural Fe atoms are oxidized to Fe(III) (Wilkin and Barnes, 1996; Lennie et al., 1997). Such a transformation would be largely invisible by SEM, unlike precipitation of new Fe(III) (hydr)oxide particles. No new peaks which corresponded with iron (hydr)oxides were found in the XRD patterns of the samples with CT, meaning that if any iron (hydr)oxides formed, particularly at pH 8 where abundant spherical particles were observed, they were mostly amorphous or poorly crystalline.

Brown/rust-colored particles were observed in the anoxic solution outside the dialysis tubing in samples with CT at pH 8 but not at pH 7, and not in the no-CT controls at either pH value (Figure A5). These particles had a Munsell hue, value, and chroma (Munsell, 1975) of 7.5 YR 5/8. The filtered particles were spherical with diameters ranging from 100 to 400 nm (Figure A6A)—similar in shape and size to those observed on the FeS surface at pH 8 (Figure 3.3D). Fe and O, but not S, were detected in the particles using EDS (not shown), consistent with an iron(III) (hydr)oxide. The powder XRD pattern of these particles contained no peaks (not shown), indicating an amorphous or poorly crystalline material.

Several SAED patterns of local areas on these particles were also collected. While most indicated an amorphous structure, consistent with non-detection of crystalline iron (hydr)oxides by powder XRD, one pattern showed two rings with somewhat indistinct edges (Figure A6B) that was similar to the SAED pattern of

two-line ferrihydrite reported by Janney et al. (2000). The *d*-values calculated by measuring the radius of the most intense areas of the rings were 1.50 Å, and 2.55 Å, which are within the reported *d*-value ranges of two-line ferrihydrite: 1.47-1.50 Å (for the (300) plane) and 2.47-2.59 Å (for the (110) plane) (Chukhov et al., 1974; Drits et al., 1993; Jambor and Dutrizac, 1998; Janney et al., 2000). Thus, based on the *d*-values calculated from the SAED pattern as well as the powder XRD and EDS results, the spherical particles in solution (Figure A6) and on the FeS surface (Figure 3.3D) were most likely a mostly poorly crystalline two-line ferrihydrite, formed through a reaction such as 3.5 or 3.6.

Unlike XRD and EDS, which are bulk analyses, the depth resolution of XPS is on the order of nanometers, making it more sensitive to chemical changes at the FeS surface (Newbury, 1997). Thus, we further investigated changes at the FeS surface after reaction with CT using XPS. Experiments at pH 8 were chosen for XPS analysis because SEM showed more morphological changes at this pH (Figure 3.3). Details of spectra fitting are in the Appendix A5. The Fe $2p_{3/2}$ spectrum of the no-CT control (Figure 3.4A) showed a broad peak with a binding energy maximum at 708 eV, similar in shape to that of pure FeS (Mullet et al., 2002). The curve fitting indicated that the surface contained mainly (in order of abundance) Fe(III)-S, Fe(II)-S, Fe(III)-O, and Fe(II)-O (Figure 3.4A). Other studies reported that the mackinawite surface was composed of both Fe(II)-S and Fe(III)-S (Pratt et al., 1994; Boursiquot et al., 2002; Mullet et al., 2004; Bourdoiseau et al., 2008; Jeong et al., 2010), and that Fe(III)-containing mackinawite may be an intermediate in the oxidation of mackinawite to greigite (Bourdoiseau et al., 2011; White et al., 2015).

The existence of Fe(II)-O and Fe(III)-O in the no-CT control may be due to the reaction of Fe(II)-S and Fe(III)-S with water.

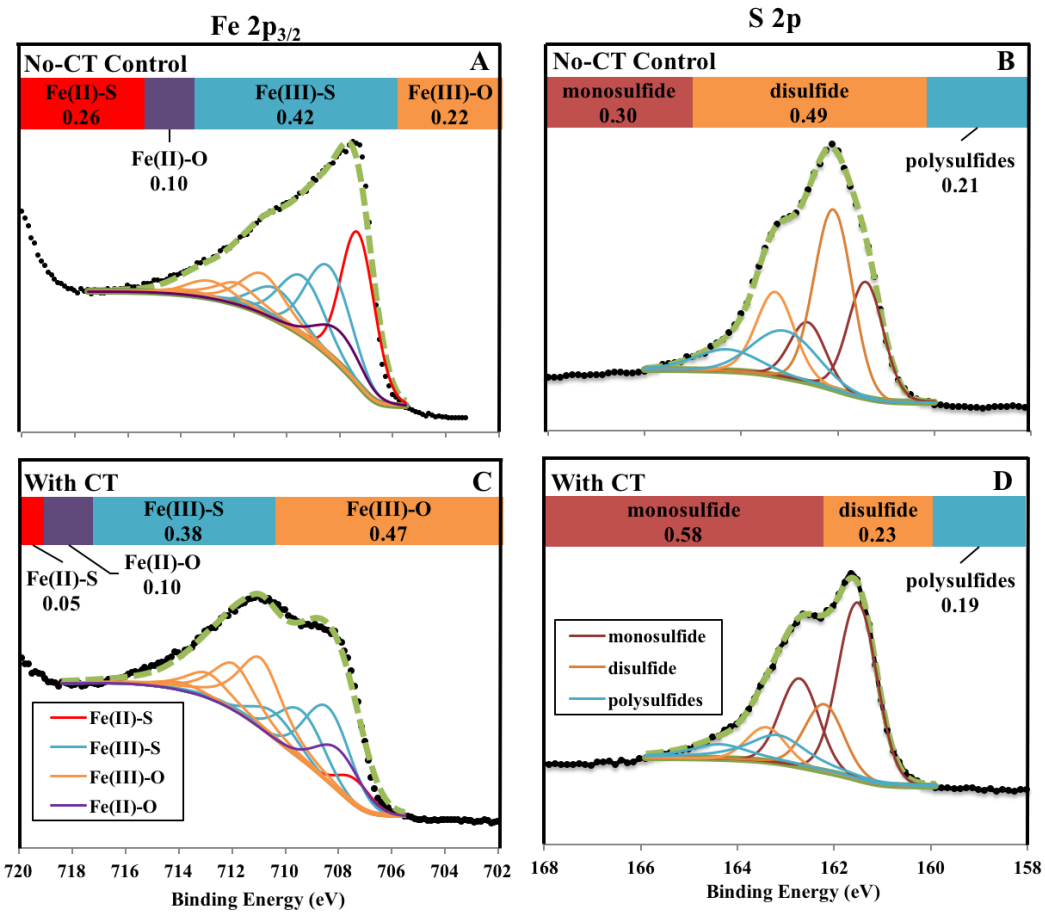


Figure 3.4. The XPS spectra of the FeS surface at pH 8, 14 days. (A) Fe $2p_{3/2}$ spectrum of no-CT control; (B) S 2p spectrum of no-CT control; (C) Fe $2p_{3/2}$ spectrum of FeS with CT; (D) S 2p spectrum of FeS with CT; Black dotted lines are experimental data, and green dashed lines are corresponding fits. The bars on top of each spectrum represent the relative proportions of species. 0.0016 M FeS; 0.022 M Tris buffer; $(2.1\pm0.2)\times10^{-3}$ M CT.

After reaction with CT, the Fe $2p_{3/2}$ peak area shifted to a higher binding energy, indicating oxidation of Fe by CT (Figure 3.4C). While the FeS that reacted with CT had the same components as the no-CT control, the contribution of Fe(II)-S

decreased and the contribution of Fe(III)-O increased after exposure to CT (Figure 3.4A and C), consistent with EDS results that showed an increase in Fe:S and a decrease in Fe:O over time when FeS reacted with CT (Figure 3.2). These XPS results are consistent with oxidation of mackinawite Fe(II)-S surface species to Fe(III)-O in the form of ferrihydrite or an amorphous iron(III) (hydr)oxide (Reactions 3.5 and 3.6).

The S 2p spectra (Figures 3.4B and D) were fit with doublets representing $2p_{1/2}$ and $2p_{3/2}$. FeS had more monosulfide and less disulfide after reacting with CT compared to the no-CT control (Figures 3.4B and D). Neither spectrum (i.e., with or without CT) indicated the presence of S in a state more oxidized than disulfide or polysulfides, including sulfate S(VI) (binding energy: 168.7± 0.2 (Asta et al., 2013)), within the time frame of 14 days, suggesting no oxidation of sulfide, and consistent with the non-detection of sulfate in solution.

XPS results indicate that reaction with CT led to a 33% decrease in Fe, a 38% decrease in S, and a 74% increase in O in the surface region of the FeS sample (Table A2). Such a trend has been noted in other studies (Boursiquot et al., 2001; Boursiquot et al., 2002; Mullet et al., 2004; Jeong et al., 2010), and can be explained by transformation of FeS to, or coverage by, a precipitated iron (hydr)oxide. For such a reaction, the relative percentage of S would decrease due to the transition of bonds from Fe-S to either Fe-O or Fe-OH in iron (hydr)oxide, and the relative percentage of Fe would also decrease due to the transition from a 1:1 ratio of Fe:S in FeS, to an Fe:O ratio of 1:2 (as in FeOOH) or 1:3 (as in $Fe(OH)_3$). This overall change in atomic composition is again consistent with the EDS results (Figure 3.2)

and SEM results (Figure 3.3D) and suggests that the predominant CT oxidation product at the FeS surface at pH 8 is a Fe(III) (hydr)oxide, since transformation of FeS predominantly to greigite (Fe_3S_4) would result in a depletion of Fe and enrichment of S. It is possible, however, that greigite was also formed at pH 8, but was present beneath a precipitated Fe(III) (hydr)oxide at the surface. Depth profile analyses have shown that oxidative dissolution of the iron sulfide mineral pyrrhotite ($Fe_{0.89}S$) by O_2 leads to a stratified surface, with an outermost layer of Fe (hydr)oxide above an iron-deficient and sulfide-rich layer (Buckley and Woods, 1985), in which the iron content decreases with reaction time (Pratt et al., 1994) and increases with depth (Mycroft et al., 1995), until the underlying pristine pyrrhotite is reached at approximately 35 Å (Pratt et al., 1994; Mycroft et al., 1995). Such stratification occurs as a result of diffusion of Fe atoms from the underlying pyrrhotite to the mineral surface (Pratt et al., 1994; Mycroft et al., 1995). While our XPS analysis did not employ depth profiling, and thus could not resolve such layers if they existed, these prior results suggest that an iron-deficient and sulfur-rich mineral like greigite could form as an intermediate in the transformation of FeS to ferrihydrite, and that FeS, greigite, and ferrihydrite could coexist in the surface region of FeS after reaction with CT (Buckley and Woods, 1985; Pratt et al., 1994; Mycroft et al., 1995). Thermodynamic calculations (Figure A7) confirm that FeS and greigite can coexist at pH 7, and that FeS, greigite, and ferrihydrite can coexist at pH 8—both consistent with our observed results. Also consistent with our results, in studying the oxidation of pyrrhotite by O_2, Buckley and Woods (1985) identified an iron deficient sulfide phase or surface region (consistent with greigite) at both

acid and alkaline pH values, and a Fe(III) (hydr)oxide surface phase at only alkaline pH values. The greater abundance of spherical particles of ferrihydrite at pH 8 than at pH 7 could be due to the lower ferrihydrite solubility at the higher pH.

3.3.3. Environmental Implications

This study provides direct evidence that greigite and ferrihydrite form at the FeS surface when it reacts with CT, with greigite the predominant product at pH 7, and ferrihydrite the predominant product at pH 8. Fe(III) (hydr)oxides such as ferrihydrite can be reductively dissolved by S(-II) to form Fe^{+2} that can then react with excess S(-II) to precipitate FeS(s) (Kocar et al., 2010). And Fe^{+2} from greigite dissolution (Cornwell and Morse, 1987; Hunger and Benning, 2007; Rickard and Luther, 2007) can also lead to FeS precipitation (Hunger and Benning, 2007) in the presence of S(-II). This suggests that FeS could be regenerated at contaminated sites by in-situ microbial sulfide generation or addition, after oxidation by chlorinated aliphatic hydrocarbons. No sulfate was formed in the oxidation of FeS by CT, so sulfate addition would be required to initiate microbial sulfate reduction for such FeS regeneration.

Since groundwater remediation applications may have time scales of months to years, more research is needed to understand the transformation and regeneration of these mineral products over longer times than those studied here. For example, dissolved Fe^{+2} can catalyze iron atom exchange and recrystallization (Tishchenko et al., 2015), and alter mineral growth (Williams and Scherer, 2004). In contact with dissolved Fe(II) (Jambor and Dutrizac, 1998) and oxygen (Das et al., 2011), ferrihydrite may transform to hematite, which can undergo further exchange with

dissolved Fe^{+2} (Frierdich et al., 2015). Even very stable Fe(III) hydr(oxides) such as hematite, however, are susceptible to reductive dissolution by dissolved sulfide (Poulton et al., 2004), and thus will re-form reactive FeS under sulfate reducing conditions. And while greigite may age to form pyrite (Benning et al., 2000; Hunger and Benning, 2007), like greigite, pyrite is susceptible to incongruous dissolution, forming Fe(II) (Davison, 1991) that can lead to precipitation of FeS in the presence of sulfide.

References

Air Force Center for Engineering and the Environment, 2008. Final technical protocol for enhanced anaerobic bioremediation using permeable mulch biowalls and bioreactors. prepared by Parsons Engineering. In *Air Force Center for Engineering and the Environment*

Asta, M. P., López, R. P., Ross, G. R., Illera, V., Cama, J., Cotte, M., and Tucoulou, R. 2013. Analysis of the iron coatings formed during marcasite and arsenopyrite oxidation at neutral-alkaline conditions. *Geologica Acta* 11 (4):465-481.

Bakalyar, S. R., Bradley, M. P. T., and Honganen, R. 1978. The role of dissolved gases in high-performance liquid chromatography. *J Chromatogr* 158:277-293.

Benning, L. G., Wilkin, R. T., and Barnes, H. L. 2000. Reaction pathways in the Fe-S system below 100 degrees C. *Chem Geol* 167 (1-2):25-51.

Birkefeld, A., Schulin, R., and Nowack, B. 2005. A new in situ method to analyze mineral particle reactions in soils. *Environ Sci Technol* 39 (9):3302-3307.

Bourdoiseau, J. A., Jeannin, M., Rémazeilles, C., Sabot, R., and Refait, P. 2011. The transformation of mackinawite into greigite studied by Raman spectroscopy. *J Raman Spectrosc* 42 (3):496-504.

Bourdoiseau, J. A., Jeannin, M., Sabot, R., Remazeilles, C., and Refait, P. 2008. Characterisation of mackinawite by Raman spectroscopy: Effects of crystallisation, drying and oxidation. *Corros Sci* 50 (11):3247-3255.

Boursiquot, S., Mullet, M., Abdelmoula, M., Genin, J. M., and Ehrhardt, J. J. 2001. The dry oxidation of tetragonal FeS_{1-x} mackinawite. *Phys Chem Miner* 28 (9):600-611.

Boursiquot, S., Mullet, M., and Ehrhardt, J. J. 2002. XPS study of the reaction of chromium (VI) with mackinawite (FeS). *Surface and Interface Analysis* 34 (1):293-297.

Buckley, A. N., and Woods, R. 1985. X-ray photoelectron spectroscopy of oxidized pyrrhotite surfaces: I. Exposure to air. *Appl Surf Sci* 22:280-287.

Chapelle, F. H., Bradley, P. M., Thomas, M. A., and McMahon, P. B. 2009. Distinguishing iron-reducing from sulfate-reducing conditions. *Ground Water* 47 (2):300-305.

Chiriţă, P., Descostes, M., and Schlegel, M. L. 2008. Oxidation of FeS by oxygen-bearing acidic solutions. *J Colloid Interf Sci* 321 (1):84-95.

Chukhov, F. V., Zvyagin, B. B., Gorshkov, A. I., Yermilova, L. P., and Balashova, V. V. 1974. Ferrihydrite. *Int Geol Rev* 16 (10):1131-1143.

Cornwell, J. C., and Morse, J. W. 1987. The characterization of iron sulfide minerals in anoxic marine sediments. *Mar Chem* 22 (2):193-206.

Criddle, C. S., and McCarty, P. L. 1991. Electrolytic model system for reductive dehalogenation in aqueous environments. *Environ Sci Technol* 25 (5):973-978.

Curtis, G. P., and Reinhard, M. 1994. Reductive dehalogenation of hexachloroethane, carbon tetrachloride, and bromoform by anthrahydroquinone disulfonate and humic acid. *Environ Sci Technol* 28 (13):2393-2401.

Das, S., Hendry, M. J., and Essilfie-Dughan, J. 2011. Transformation of two-line ferrihydrite to goethite and hematite as a function of pH and temperature. *Environ Sci Technol* 45 (1):268-275.

Davison, W. 1991. The solubility of iron sulfides in synthetic and natural waters at ambient temperature. *Aquat Sci* 53 (4):309-329.

Devlin, J. F., and Müller, D. 1999. Field and laboratory studies of carbon tetrachloride transformation in a sandy aquifer under sulfate reducing conditions. *Environ Sci Technol* 33 (7):1021-1027.

Drits, V. A., Sakharov, B. A., Salyn, A. L., and Manceau, A. 1993. Structural model for ferrihydrite. *Clay Minerals* 28 (2):185-207.

Frierdich, A. J., Helgeson, M., Liu, C. S., Wang, C. M., Rosso, K. M., and Scherer, M. M. 2015. Iron atom exchange between hematite and aqueous Fe(II). *Environ Sci Technol* 49 (14):8479-8486.

Gallegos, T. J., Han, Y.-S., and Hayes, K. F. 2008. Model predictions of realgar precipitation by reaction of As (III) with synthetic mackinawite under anoxic conditions. *Environ Sci Technol* 42 (24):9338-9343.

He, Y. T., Wilson, J. T., Su, C., and Wilkin, R. T. 2015. Review of abiotic degradation of chlorinated solvents by reactive iron minerals in aquifers. *Ground Water Monit R* 35 (3):57-75.

He, Y. T., Wilson, J. T., and Wilkin, R. T. 2010. Impact of iron sulfide transformation on trichloroethylene degradation. *Geochim Cosmochim Ac* 74 (7):2025-2039.

Hunger, S., and Benning, L. G. 2007. Greigite: a true intermediate on the polysulfide pathway to pyrite. *Geochem T* 8:1-20.

Jambor, J. L., and Dutrizac, J. E. 1998. Occurrence and constitution of natural and synthetic ferrihydrite, a widespread iron oxyhydroxide. *Chem Rev* 98 (7):2549-2585.

Janney, D. E., Cowley, J. M., and Buseck, P. R. 2000. Transmission electron microscopy of synthetic 2-and 6-line ferrihydrite. *Clays Clay Miner* 48 (1):111-119.

Jeong, H. Y., Han, Y.-S., Park, S. W., and Hayes, K. F. 2010. Aerobic oxidation of mackinawite (FeS) and its environmental implication for arsenic mobilization. *Geochim Cosmochim Ac* 74 (11):3182-3198.

Kappler, A., and Newman, D. K. 2004. Formation of Fe (III)-minerals by Fe (II)-oxidizing photoautotrophic bacteria. *Geochim Cosmochim Ac* 68 (6):1217-1226.

Kennedy, L. G., Everett, J. W., Becvar, E., and Defeo, D. 2006. Field-scale demonstration of induced biogeochemical reductive dechlorination at Dover Air Force Base, Dover, Delaware. *J Contam Hydrol* 88 (1-2):119-136.

Kenneke, J. F., and Weber, E. J. 2003. Reductive dehalogenation of halomethanes in iron-and sulfate-reducing sediments. 1. Reactivity pattern analysis. *Environ Sci Technol* 37 (4):713-720.

Kocar, B. D., Borch, T., and Fendorf, S. 2010. Arsenic repartitioning during biogenic sulfidization and transformation of ferrihydrite. *Geochim Cosmochim Ac* 74 (3):980-994.

Kriegman-King, M. R., and Reinhard, M. 1992. Transformation of carbon tetrachloride in the presence of sulfide, biotite, and vermiculite. *Environ Sci Technol* 26 (11):2198-2206.

Lan, Y., and Butler, E. C. 2014. Monitoring the transformation of mackinawite to greigite and pyrite on polymer supports. *Appl Geochem* 50:1-6.

Lee, M. D., Lieberman, M.T., Beckwith, W.J., Borden, R.C., Everett, J., Kennedy, L., Gonzales, J.R., . 2003. Pilots to enhance trichloroethene reductive dechlorination and ferrous sulfide abiotic transformation. the Seventh International In Situ and On-Site Bioremediation Symposium, Orlando, Florida, June 2–5.

Lennie, A. R., Redfern, S. A. T., Champness, P. E., Stoddart, C. P., Schofield, P. F., and Vaughan, D. J. 1997. Transformation of mackinawite to greigite: An in situ X-ray powder diffraction and transmission electron microscope study. *Am Mineral* 82 (3):302-309.

Lin, S., Krause, F., and Voordouw, G. 2009. Transformation of iron sulfide to greigite by nitrite produced by oil field bacteria. *Appl Microbio Biotechnol* 83 (2):369-376.

Lovley, D. R., and Phillips, E. J. 1986. Organic matter mineralization with reduction of ferric iron in anaerobic sediments. *Appl Environ Microbiol* 51 (4):683-689.

Majzlan, J., Navrotsky, A. l., and Schwertmann, U. 2004. Thermodynamics of iron oxides: Part III. Enthalpies of formation and stability of ferrihydrite ($\sim Fe(OH)_3$), schwertmannite ($\sim FeO(OH)_{3/4}(SO_4)_{1/8}$), and ε-Fe_2O_3. *Geochim Cosmochim Ac* 68 (5):1049-1059.

Metschl, J. 1924. The supersaturation of gases in water and certain organic liquids. *J of Phys Chem* 28 (5):417-437.

Millero, F. J. 1985. The effect of ionic interactions on the oxidation of metals in natural waters. *Geochim Cosmochim Ac* 49 (2):547-553.

Mullet, M., Boursiquot, S., Abdelmoula, M., Genin, J. M., and Ehrhardt, J. J. 2002. Surface chemistry and structural properties of mackinawite prepared by reaction of sulfide ions with metallic iron. *Geochim Cosmochim Ac* 66 (5):829-836.

Mullet, M., Boursiquot, S., and Ehrhardt, J.-J. 2004. Removal of hexavalent chromium from solutions by mackinawite, tetragonal FeS. *Colloid Surface A* 244 (1-3):77-85.

Munsell, A. H. 1975. Munsell soil color charts. *Baltimore, Maryland*.

Mycroft, J. R., Nesbitt, H. W., and Pratt, A. R. 1995. X-ray photoelectron and Auger electron spectroscopy of air-oxidized pyrrhotite: Distribution of oxidized species with depth. *Geochim Cosmochim Ac* 59 (4):721-733.

Newbury, D. E. 1997. Chemical compositional mapping by microbeam analysis at the micrometer scale and finer. *Microelectron J* 28 (4):489-508.

Poulton, S. W., Krom, M. D., and Raiswell, R. 2004. A revised scheme for the reactivity of iron (oxyhydr)oxide minerals towards dissolved sulfide. *Geochim Cosmochim Ac* 68 (18):3703-3715.

Pratt, A. R., Muir, I. J., and Nesbitt, H. W. 1994. X-Ray photoelectron and Auger-electron spectroscopic studies of pyrrhotite and mechanism of air oxidation. *Geochim Cosmochim Ac* 58 (2):827-841.

Rickard, D., and Luther, G. W. 2007. Chemistry of iron sulfides. *Chem Rev* 107 (2):514-562.

Rickard, D. T. 1969. The chemistry of iron sulphide formation at low temperatures. *Stockh Contrib Geol* 20:67-95.

Shao, H., and Butler, E. C. 2009. The relative importance of abiotic and biotic transformation of carbon tetrachloride in anaerobic soils and sediments. *Sediment Contam* 18 (4):455-469.

Shen, H., and Wilson, J. T. 2007. Trichloroethylene removal from groundwater in flow-through columns simulating a permeable reactive barrier constructed with plant mulch. *Environ Sci Technol* 41 (11):4077-4083.

Sweeney, R., and Kaplan, I. 1973. Pyrite framboid formation; laboratory synthesis and marine sediments. *Econ Geol* 68 (5):618-634.

Tishchenko, V., Meile, C., Scherer, M. M., Pasakarnis, T. S., and Thompson, A. 2015. Fe^{2+} catalyzed iron atom exchange and re-crystallization in a tropical soil. *Geochim Cosmochim Ac* 148:191-202.

Vaughan, D. J., and Craig, J. R. 1978. *Mineral chemistry of metal sulfides*: Cambridge University Press.

White, L. M., Bhartia, R., Stucky, G. D., Kanik, I., and Russell, M. J. 2015. Mackinawite and greigite in ancient alkaline hydrothermal chimneys: Identifying potential key catalysts for emergent life. *Earth Planet Sci Lett* 430:105-114.

Wilkin, R. T., and Barnes, H. L. 1996. Pyrite formation by reactions of iron monosulfides with dissolved inorganic and organic sulfur species. *Geochim Cosmochim Ac* 60 (21):4167-4179.

Williams, A. G. B., and Scherer, M. M. 2004. Spectroscopic evidence for Fe(II)-Fe(III) electron transfer at the iron oxide-water interface. *Environ Sci Technol* 38 (18):4782-4790.

Wolthers, M. 2003. Geochemistry and environmental mineralogy of the iron-sulfur-arsenic system. Ph.D, Utrecht Univ.

Chapter 4

Iron Sulfide Oxidation Products Formed during Reductive Dechlorination of Trichloroethylene and Tetrachloroethylene

4.1. Introduction

Because of its reducing capability, FeS has been widely studied in the degradation of trichloroethylene (TCE) and tetrachloroethylene (PCE) (He et al., 2015). TCE and PCE have been commonly detected in groundwater systems due to their usage in commercial and industrial applications (Moran et al., 2007). Besides biological transformation of TCE and PCE, many reactive iron minerals have been employed in the degradation of TCE and PCE in both laboratory and field studies, among these minerals, FeS shows the strongest reactivity (He et al., 2015). Laboratory studies showed that FeS can transform PCE to TCE, cis-DCE, and 1,1,-DCE via hydrogenolysis, to dichloroacetylene, chloroacetylene, and acetylene via reductive β-elimination, and to 1,1-DCE via α-elimination (Butler and Hayes, 1999; Jeong and Hayes, 2007). Similar to PCE, TCE can be transformed by FeS to chloroacetylene and acetylene via reductive β-elimination, and by hydrogenolysis to 1,1-DCE and *cis*-DCE (Butler and Hayes, 1999; Jeong and Hayes, 2007).

In engineered systems designed for groundwater remediation, sulfate and iron-reducing conditions are often favored in permeable reactive barriers (Shen and Wilson, 2007) and enhanced reductive dechlorination sites, and these conditions favor the formation of FeS (He et al., 2015). For example, adding Fe(II) to simulated sulfur-rich groundwater successfully generated FeS, and the resulting FeS enhanced reductive transformation of TCE (Hyun and Hayes, 2009). In groundwater

systems where concentrations of dissolved iron or dissolved sulfate are limited, the formation of FeS can be achieved by adding iron oxide (He et al., 2015) or sulfate salt (Kennedy et al., 2006a; Kennedy et al., 2006b) to remediation locations containing sulfate reducing bacteria, and consequently enhance the dechlorination of TCE and PCE (Shen and Wilson, 2007). Despite the well-characterized dechlorination rates and organic dechlorination products, the corresponding FeS-associated products during the dechlorination of TCE and PCE have not been well studied. He et al. (2010) reported that the FeS-associated products were lepidocrocite, goethite, and pyrite during the reaction with TCE, however, they did not report whether such oxidation took place in the control samples without TCE. In Chapter 3, we reported that FeS was oxidized and transformed to greigite and ferrihydrite by carbon tetrachloride (CT). TCE and PCE are more frequently used in industry and detected in groundwater system compared to CT (Doherty, 2000a, b; Moran et al., 2007). Thus, it is crucial to understand the FeS oxidation products formed during the reductive degradation of TCE and PCE.

By fully understanding the FeS-associated products formed during reactions with TCE and PCE, the application and regeneration of FeS can be properly designed in remediation sites. The objective of the research described in this chapter was to identify the FeS-associated products during the dechlorination of TCE and PCE by FeS. The rates of FeS-mediated reductive dechlorination of TCE and PCE increased with the increase of pH (Butler and Hayes, 1999; Liang et al., 2007), indicating faster products formation can be observed at higher pH values (for

example, pH 8). Based on this, we chose to study the mineralogical changes of FeS during the dechlorination of TCE and PCE by FeS at pH 8.

4.2. Material and methods

4.2.1. General experimental conditions

All experimental procedures were done in an anaerobic chamber (Coy Laboratory Products., Inc., Grass Lake MI) maintained with a gas mixture of 95% N_2 and 5% H_2 and a Pd catalyst to remove trace amounts of oxygen, or a glove bag (108D X-27-27, Glas-Gol, LLC., Terre Haute, IN) filled with N_2. All liquids (nanopure water, methanol, TCE, and PCE) were sparged with N_2 for at least 30 minutes before being transferred to the anaerobic chamber. All aqueous solutions were made with nanopure water (18.0 MΩ-cm resistivity, Barnstead Ultrapure Water System, IA). The solid chemical reagents and glassware were equilibrated in the anaerobic chamber overnight before use to remove trace amount of oxygen attached to them.

4.2.2. FeS synthesis

FeS was prepared using ferrous iron and sulfide solutions (Rickard, 1969), details can be found in Appendix A1. Briefly, in experiments that measured the kinetics of TCE and PCE dechlorination by FeS, 1.15 mL of 0.025 M $FeCl_2$ solution and 1.15 mL of 0.025 M Na_2S solution were added to a 9 mL serum bottle containing 1 mL of tris(hydroxymethyl)aminomethane (Tris) buffer (adjusted with 0.1 M HBr to pH 8), and diluted with nanopure water to 9 mL, and this yielded minimal headspace. FeS precipitates were left inside the anaerobic chamber for

three days. During these three days, FeS particles were washed with Tris buffer (22 mM) three times to remove background salts. The final concentrations were 3.0 mM FeS and 22 mM Tris buffer.

4.2.3. Experiments to measure dissolved species over time

Nine mL serum bottles containing 3.0 mM FeS in pH 8 Tris buffer (prepared following the procedures in the previous section) were spiked with TCE and PCE stock solutions. The resulting concentrations were (0.46±0.01) mM PCE and (3.55±0.08) mM TCE (Table 4.1). TCE is more soluble than PCE in water, so a higher TCE concentration was able to be achieved. The serum bottles were immediately crimp-sealed with Teflon-lined rubber stoppers and aluminum crimp seals, and placed on a rocking platform shaker (45 rocks per minute). At desired time, serum bottles were centrifuged at 615 × g for 20 min, then filtered using a Puradis^{TM} 25 mm disposable filter (0.1 μm polyethersulfone membrane with polypropylene housing, Whatman, Piscataway, NJ). PCE, TCE, and *cis*-DCE were measured using a Shimadzu gas chromatograph (GC-17A) with an electron capture detector and a 30 m J&W Scientific DB-624 column (30 m×0.53 mm×3 μm). Details of the sample treatments and GC method can be found in Appendix A2. A split ratio of 10:1 was used during the measurement. Dissolved Fe^{+2} was measured using a ferrozine assay (Lovely and Phillips, 1986). Dissolved S(-II) was quantified with an Ag/Ag_2S electrode (Orion 9616BN) using sulfide antioxidant buffer (containing 2.5 M sodium hydroxide, 0.2 M ethylenediaminetetraacetic acid disodium salt, and 0.2 M L-ascorbic acid). All samples were analyzed for chloride and sulfate by ion chromatography (Shao and Butler, 2009). Samples containing

FeS (3.0 mM) in pH 8 buffer without PCE and TCE were treated and measured exactly the same way as the reacted FeS samples, and were used as controls (referred to below as "FeS control"). All samples were prepared in duplicate, each independent sample was measured twice, and the resulting concentrations averaged.

Table 4.1*. Concentrations used in different experimental setups.

	FeS (mM)	TCE (mM)	PCE (mM)
Experiments to measure dissolved species over time (kinetic experiments)	3.0	3.55±0.08	0.46±0.01
Experiments to monitor surface morphology changes (SEM analysis with FeS chips, Figure A1)	3.0	10.3±0.3	1.5±0.1
Experiment to study mineral phases and surface species changes (XRD, TEM/SAED, and XPS analyses, dialysis tubing setup, Figure A2)	1.6	10.3±0.3	1.5±0.1

* The uncertainties represent the standard deviation of the mean of two independent samples for the kinetic experiments (n=2) or three independent samples for the others (n=3).

4.2.4. Experiments for FeS mineral characterization

In order to detect the most significant FeS surface changes happened due to reactions with TCE and PCE, high TCE and PCE concentrations and low FeS concentration were used to maximize the molar ratio of TCE and PCE to FeS in the experiments for FeS mineral characterization. After the reaction, the reacted FeS samples (referred to below as "FeS with TCE" and "FeS with PCE"), as well as the FeS controls, were analyzed using high resolution transmission electron microscopy (HRTEM) with energy dispersive X-ray spectroscopy (EDS), powder X-ray

diffraction (XRD), X-ray photoelectron spectroscopy (XPS), and scanning electron microscopy (SEM) with EDS.

To monitor the surface morphology changes of FeS during reactions with TCE and PCE, we used the experimental setup using FeS chips reported in Chapter 2. The preparation of FeS chips and the experimental setup followed the procedures described in Chapter 3, except 50 μL N_2-sparged TCE and PCE were added to the serum bottles, instead of CT. The experimental setup was demonstrated in Figure A1 and the concentrations used can be found in Table 4.1. The FeS concentration was estimated, and equaled 3.0 mM. At desired time, the serum bottles were opened, the FeS chips were washed with nanopure water and dried inside the anaerobic chamber. FeS chips were transferred to the SEM lab inside an air tight jar, coated with iridium, and analyzed using a Zeiss NEON high resolution field emission SEM.

The FeS samples for TEM, XRD, and XPS analyses were prepared with a small amount of FeS particles enclosed in two pieces of dialysis tubing in aqueous TCE and PCE solutions. Details of the experimental setup were given in Chapter 3. Instead of CT, 7 mL pure phases of N_2-sparged TCE and PCE were added to the 1 L serum bottles containing FeS particles enclosed in dialysis tubing. The total volume, including FeS slurry, pH buffer, and TCE and PCE, was 985 mL. The final concentrations in this setup (demonstrated in Figure A2) were 1.6 mM FeS and 22 mM Tris buffer (Table 4.1).

The final concentration was (1.5±0.1) mM PCE and (10.3±0.3) mM TCE in the experimental setups using FeS chips and dialysis tubing (Table 4.1). The concentrations were measured from the aqueous phase in the serum bottles

containing 9 mL nanopure water, pure phase of TCE and PCE, and minimal headspace. The uncertainties are one standard deviation of the mean of three independent samples. The TCE and PCE concentrations were higher than those used in the aforementioned kinetic experiments, because pure phases of TCE and PCE existed in the systems using FeS chips and dialysis tubing. We did not use pure phases of TCE and PCE in the kinetic experiments because this approach did not give instantly reproducible concentrations after the addition of pure phases of TCE and PCE to the solutions.

At seven weeks, the serum bottles containing FeS particles enclosed in dialysis tubing were opened inside a glove bag. Seven weeks was chosen because at this time both organic and inorganic products formed during the reactions between FeS with TCE and PCE were detected, indicating the FeS surface was reacted. The particles inside the dialysis tubing were collected in secondary containers. The FeS particles were settled by gravity, the supernatant was removed, and nanopure water was used to wash the FeS particles three times to remove the background salts, all inside a glove bag. The washed FeS particles were transferred into the anaerobic chamber using airtight jars, centrifuged at 7200 × g for 30 min using a microcentrifuge (Labnet International Inc., Edison, NJ), decanted, and dried inside the anaerobic chamber. A subset of the dried particles was transferred to the XRD lab inside air-tight jars, and analyzed by a Rigaku Ultima IV powder X-ray diffractometer using a zero-background holder. Details of XRD analysis can be found in Appendix A4. A second subset of the dried particles was stored in sealed serum bottles under an atmosphere of 95% N_2 and 5% H_2, and shipped via next

morning delivery to Evans Analytical Group, East Windsor, NJ. Upon receipt, the FeS particles were opened inside a glove bag and transferred to the XPS chamber under nitrogen in an inert transfer vessel. The analysis was done with a PHI 5701 LSci instrument, a monochromatic Al K_α source (1486.6 eV) and an analysis area of 2.0 × 0.8 mm. Both survey spectra and high energy resolution spectra (Fe $2p_{3/2}$, S 2p, O 1s, C 1s) were collected. Charge correction was done with C 1s species set at 284.8 eV. A third subset of the dried FeS particles was placed on holey-carbon grids, transferred to the HRTEM lab in sealed serum bottles under an atmosphere of 95% N_2 and 5% H_2, and analyzed using a JEOL 2010-F field emission HRTEM at 200 kV. The HRTEM image processing, including the calculation of d-spacing between the layers, as well as the generation of diffraction patterns using the fast Fourier transformation (FFT), were completed using Gatan Microscopy Suite® (GMS, version 2.32, Gatan, Inc., Pleasanton, CA) and DiffTools (Mitchell, 2008). One example of the d-spacing calculation can be found in Appendix B1 and Figure B1. SAED patterns were analyzed using ImageJ, a public domain, Java-based image processing program developed by National Institutes of Health.

4.3. Results and discussion

4.3.1. Kinetics of TCE and PCE transformation by FeS

Although the kinetics of TCE and PCE transformation by FeS have been well studied and reviewed (He et al., 2015), we quantified TCE and PCE as a function of time in order to obtain reaction profiles relevant for the experimental conditions used in this study, and to measure possible inorganic reaction products

such as dissolved Fe(II) and Cl^- (Figure 4.1), which might provide evidence for the products formed on FeS surface. In this study, we maximized the molar ratios of PCE:FeS and TCE:FeS, and this maximized the possibility of detecting the most significant FeS surface changes during reactions with TCE and PCE. A very low FeS concentration (3.0 mM, 0.264 g/L) was used, as well as very high PCE and TCE concentrations, and the molar ratio of PCE:FeS and TCE:FeS equaled 0.5 and 3.4, respectively. Compared to other studies, these two ratios are extremely high. Additionally, not all FeS is accessible, only the surface of FeS particles is involved in the dechlorination because of the surface-mediated nature of the dechlorination of TCE and PCE by FeS. Thus, the experimental setup used in our studies made large degrees of TCE and PCE dechlorination unlikely.

A larger portion of PCE was lost than that of TCE (Figures 4.1A and B), because the Henry's Law constant of PCE (18 atm/M) is higher than that of TCE(10 atm/M) (Gossett, 1987), so PCE is more volatile. All the dissolved S(-II) concentrations (not shown) were below the detection limits (0.05 mM). The Henry's Law constant of H_2S (10 atm/M) (Morel and Hering, 1993) is very close to that of TCE. It is possible that dissolved S(-II) might have been formed but then volatilized. Despite the volatilization losses in the samples with FeS and the controls, differences in dissolved Fe^{+2} (Figures 4.1C and D) and Cl^- (Figures 4.1E and F) were still observed. Although the concentrations of dissolved Fe^{+2} were scattered, the dissolved Fe^{+2} concentrations differences between the reacted samples and the controls increased with time. This suggests that dissolved Fe^{+2} is a product formed during the dechlorination (Figures 4.1C and D). The dissolved Fe^{+2} in the control

samples may be due to the dissolution of FeS. Transformation of FeS by TCE and PCE to produce dissolved Fe^{+2}, greigite (Fe_3S_4), and dechlorination products (using cis-DCE and TCE as examples of dechlorination products for TCE and PCE, respectively) could take place by oxidative dissolution of FeS, as shown below:

$$4\ FeS(s) + C_2HCl_3 + H^+ \rightarrow Fe_3S_4(s) + Fe^{+2} + C_2H_2Cl_2 + Cl^- \quad 4.1$$

$$4\ FeS(s) + C_2Cl_4 + H^+ \rightarrow Fe_3S_4(s) + Fe^{+2} + C_2HCl_3 + Cl^- \quad 4.2$$

In each reaction, the positive charge gained by FeS when it donates electrons to TCE or PCE is balanced by the loss of Fe^{+2} to solution (Buckley and Woods, 1985; Jeong and Hayes, 2007).

Measurement of cis-DCE was easily accomplished using the same GC method used for PCE and TCE, so cis-DCE data were collected. We detected TCE (0.002 mM, accounts for 0.5% of the initial PCE amount) as a dechlorination product of PCE, and cis-DCE (0.008 mM, accounts for 0.2% of the initial TCE amount) as a dechlorination product of TCE after seven weeks. Another dechlorination product detected was Cl^- (Figures 4.1E and F). More Cl^- and Fe^{+2} were produced during the degradation of TCE by FeS ($[Cl^-]$=0.084 mM, $[Fe^{+2}]$=0.031 mM) compared to the degradation of PCE by FeS ($[Cl^-]$=0.055 mM, $[Fe^{+2}]$=0.020 mM) at seven weeks, indicating more TCE was reacted with FeS. We assumed that if any dechlorination products were detected, the FeS surface reacted with TCE and PCE undoubtedly. Therefore, at seven weeks, when dechlorination products were detected, the samples for solid characterization were collected and analyzed.

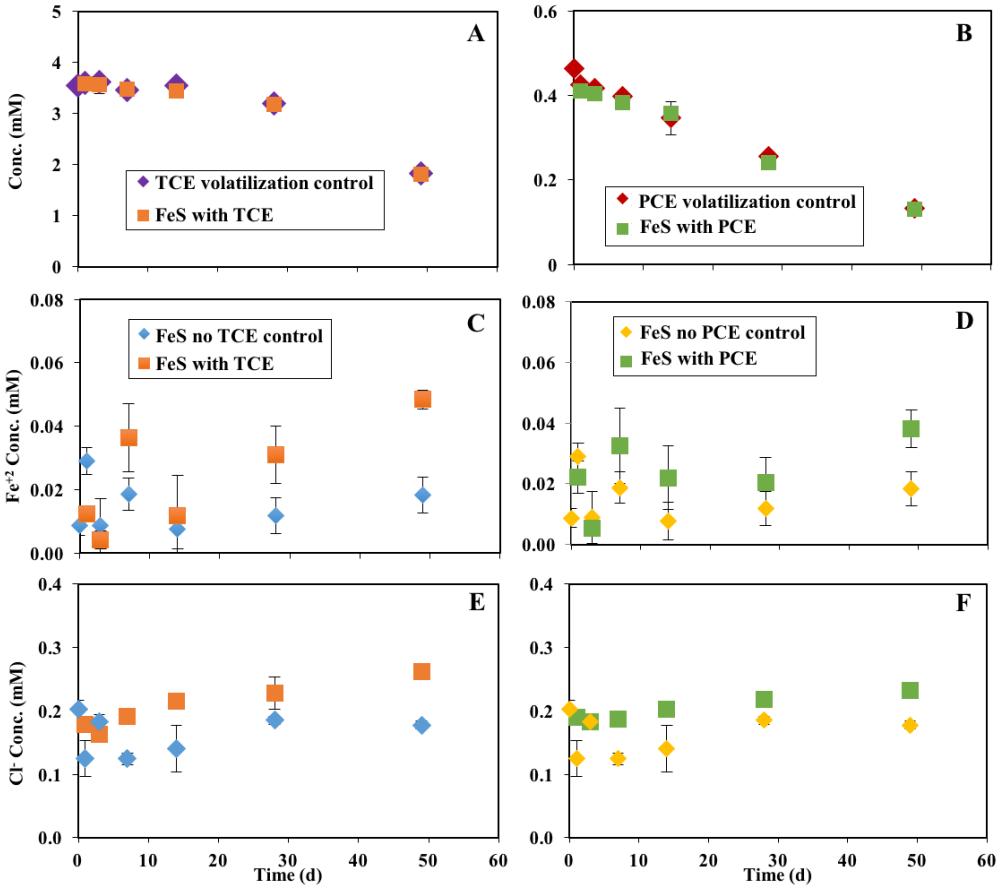


Figure 4.1. Aqueous concentration changes during reaction of FeS with TCE and PCE. (A) TCE; (B) PCE; (C) and (D) dissolved Fe^{+2}; (E) and (F) Cl^-. 3 mM FeS, 22 mM Tris buffer, pH 8. $C_{0,\,TCE}$ =(3.55±0.08) mM, $C_{0,\,PCE}$ =(0.46 ±0.01) mM. Error bars represent the standard deviation of the mean from two independent samples (each independent sample was measured twice). TCE volatilization control in (A) and PCE volatilization control in (B) were samples containing TCE and PCE only, without FeS, and they were used to monitor volatilization losses.

4.3.2. Characterization of the FeS surface after reaction with TCE and PCE

XRD was used to investigate the changes in mineral phases of the solids after reaction with TCE and PCE. No changes were found among the FeS control and two FeS samples that reacted with TCE and PCE, and all three samples indicate merely peaks from mackinawite (Figure 4.2). The results suggested either the newly formed FeS-associated products were amorphous and did not produce crystalline

diffraction peaks or the changes only happened on the very surface of FeS and could not be detected by XRD. The detection limits of XRD was estimated to be 2.0% to 4% by weight (Smith, 1999). In actual practice, the detection limits may be even higher depending on the chemistry, size, and crystallinity of the samples. Given the possibilities the oxidation products may be poorly crystalline or may have small particles sizes (such as ferrihydrite detected in Chapter 3), it is likely that the changes were below the detection limits.

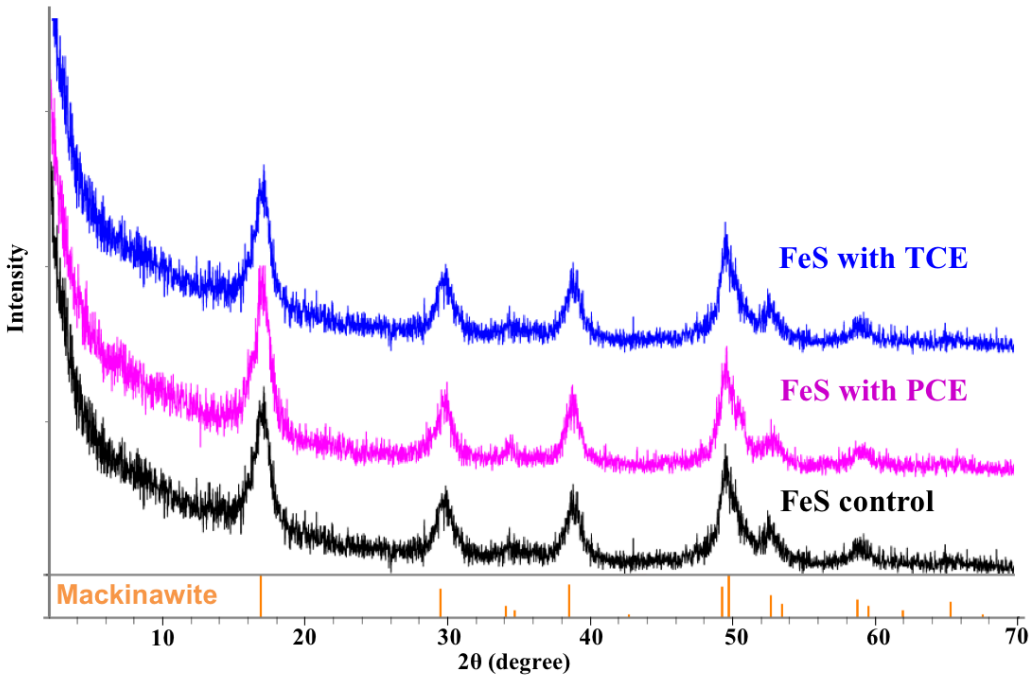


Figure 4.2. XRD patterns of the FeS with TCE sample, the FeS with PCE sample, and the FeS control sample, pH 8, seven weeks.

In order to study changes in atomic composition and mineralogical structure of the samples, HRTEM with EDS and selected area electron diffraction (SAED) were employed. EDS data were collected from randomly selected particles within

each kind of FeS sample. For example, 16 particles in the FeS control sample were analyzed, 12 particles were analyzed in the FeS with TCE sample, and 16 particles in the FeS with PCE sample were analyzed. The sizes of the particles that have been analyzed ranged from 20 nm to 150 nm. These measurements served as survey analyses and provided the average atomic percent of the samples. The detected atomic percent of O, Fe, and S were summed, normalized to 100% in total, and reported in Figure 4.3. The O atomic percent in FeS with TCE sample (15%) is twice the amount of that in the FeS control sample (7%). The O atomic percent in the FeS with PCE sample (10%) increased 40%, compared to the FeS control sample. The increase in O percent was greater in the FeS with TCE sample, compared to that in the FeS with PCE sample. This may be due to that more TCE was reacted with FeS compared to PCE, which agrees with the results in the kinetic experiments (Figure 4.1). An increase of O on the FeS surface was observed in previous studies (Boursiquot et al., 2001; Boursiquot et al., 2002; Mullet et al., 2004; Jeong et al., 2010), indicating the possibility of the formation of iron (hydr)oxides. This is consistent with the FeS oxidation product by CT at pH 8, which is reported in Chapter 3. Possible reactions of FeS transformation to iron (hydr)oxides during the reaction with TCE and PCE are listed as follows, where $Fe(OH)_3$ represents 2-line ferrihydrite, a typical poorly crystalline iron (hydr)oxides (Majzlan et al., 2004):

$$2\ FeS(s) + C_2HCl_3 + 6\ H_2O \rightarrow 2\ Fe(OH)_3(s) + 2\ HS^- + 3\ H^+ + C_2H_2Cl_2 + Cl^- \quad 4.3$$

$$2\ FeS(s) + C_2Cl_4 + 6\ H_2O \rightarrow 2\ Fe(OH)_3(s) + 2\ HS^- + 3\ H^+ + C_2HCl_3 + Cl^- \quad 4.4$$

Beside the increase of O, consistent decreases of Fe and S on the FeS surface after reaction with TCE and PCE were observed compared to the FeS control,

although these decreases did not appear to be statistically significant (Figure 4.3). The decrease of Fe percent may be due to the transformation from a 1:1 ratio of Fe:S in FeS, to a 1:2 ratio of Fe:O in FeOOH or a 1:3 ratio of Fe:O in $Fe(OH)_3$ (as shown in Reactions 4.3 and 4.4).

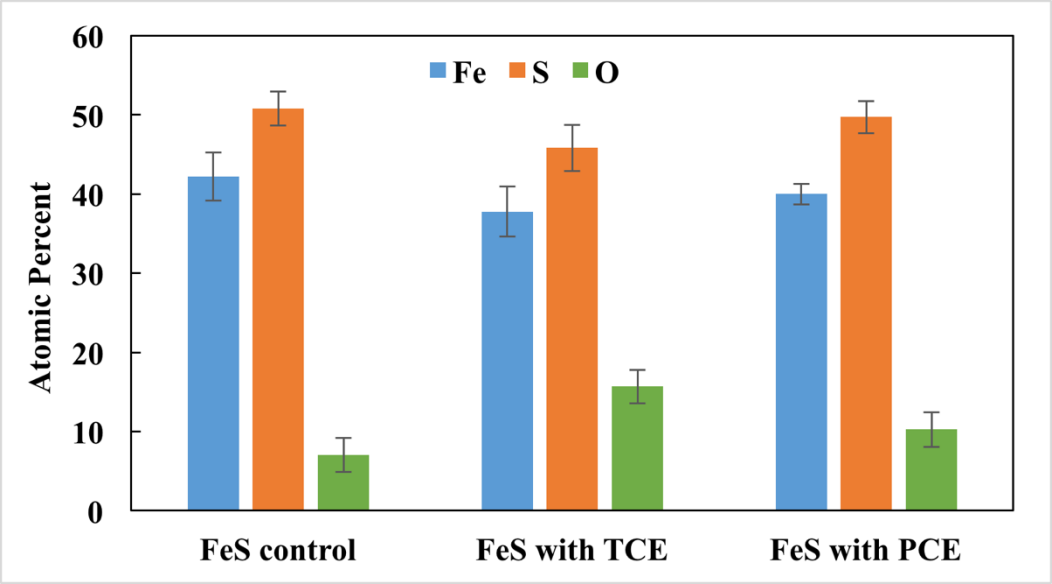


Figure 4.3. Atomic percent of O, Fe, and S. pH 8, seven weeks. Normalized to 100% of the elements reported, unreported elements include C and Cu from the holey carbon grids. EDS does not detect H or He. The error bars represent the standard deviation of several (n) measurements (FeS control, n=16; FeS with TCE, n=12; FeS with PCE, n=16).

HRTEM analysis did not show morphology changes among the FeS control (Figure 4.4A), FeS with TCE (Figure 4.5A), and FeS with PCE (Figure 4.6A) at seven weeks. All the samples contained nanoparticles that were irregularly shaped, or plate-like, and strongly aggregated. Similar characteristics have been observed in the synthesized FeS samples (Jeong et al., 2008; Csakberenyi-Malasics et al., 2012). Part of the particles oriented with the (001) plane parallel to the grid (indicated by // on the HRTEM images), while the rest oriented with the (001) plane perpendicular

to the grid (indicated by ⊥ on the HRTEM images). Figures 4.4B and 4.4C showed the aggregated plate-like particles in the FeS control sample at high magnification. The perpendicular particles (⊥-particles) showed the layered structure of FeS, and the measured d-spacing equaled 5 Å (Figure 4.4C), indicating the (001) lattice fringes. Another d-spacing ~ 3 Å was also observed, corresponding to the (101) lattice fringes (Figure 4.4C). Similar d-spacings were observed in other randomly selected areas (~10 areas) on the FeS particles in the FeS control sample (not shown). The d-spacings may vary to some extent, but are typical between 2.9~ 3 Å, and 5.0~5.1 Å. No d-spacings of other minerals were found in the randomly selected areas of the FeS control sample. This is consistent with the no detection of peaks from other minerals besides mackinawite in the XRD patterns (Figure 4.2).

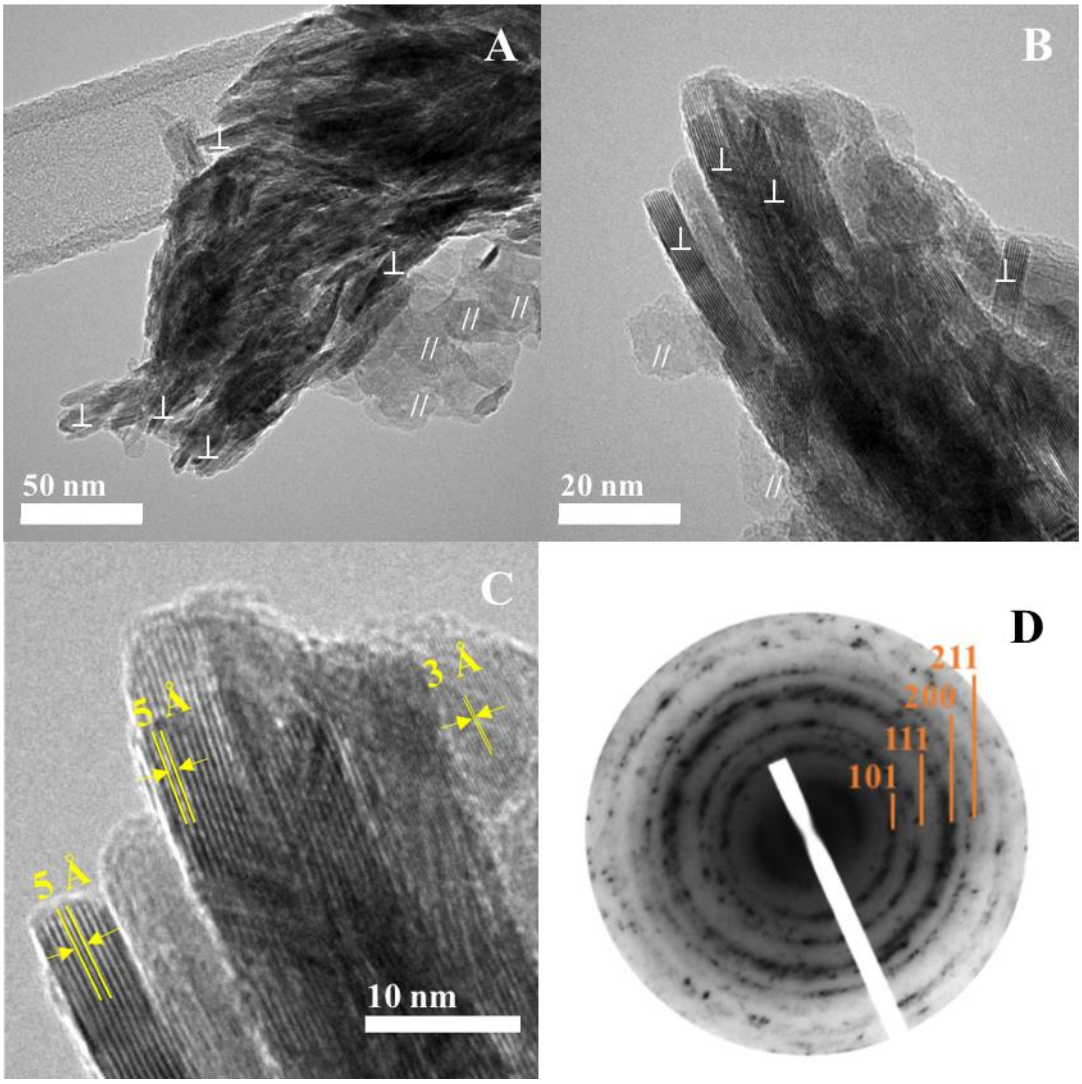


Figure 4.4. FeS control sample, pH 8, seven weeks. (A), (B) and (C) HRTEM images, and (D) SAED pattern of (A). Diffraction rings produced by mackinawite are marked by Miller indices in orange. In (A) and (B), FeS particles lying with the (001) plane parallel and perpendicular to the TEM grid are indicated by // and ⊥, respectively.

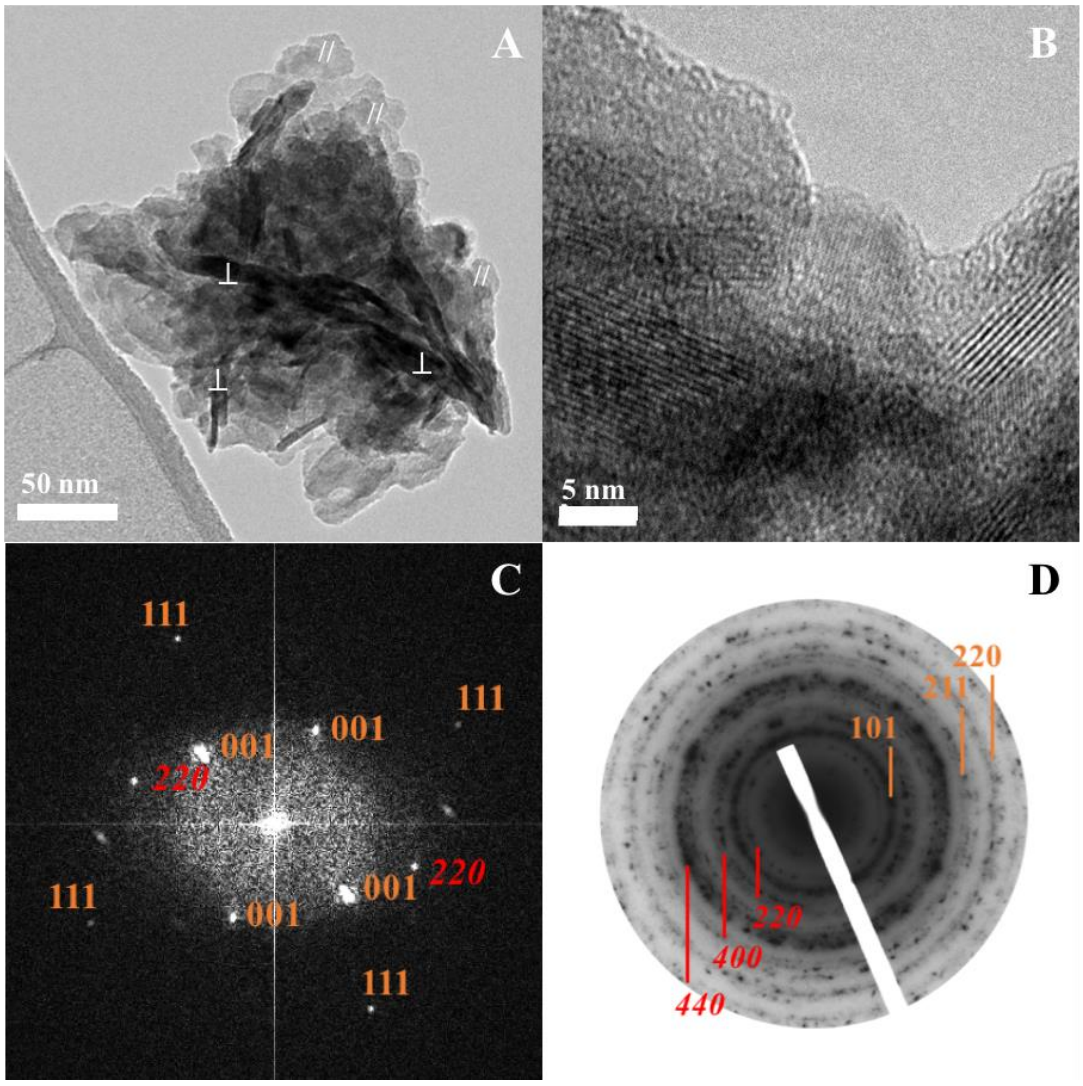


Figure 4.5. FeS with TCE sample, pH 8, seven weeks. (A) and (B) HRTEM image; (C) corresponding FFT pattern of (B). (D) SAED pattern of (A); SAED shows the presence of minor greigite (rings produced by mackinawite and greigite are marked by Miller indices in orange and red, respectively). The diffraction maxima of the FFT pattern (C) was indexed to those of FeS and greigite in orange and red, respectively. In (A), FeS particles lying with the (001) plane parallel and perpendicular to the TEM grid are indicated by // and ⊥, respectively.

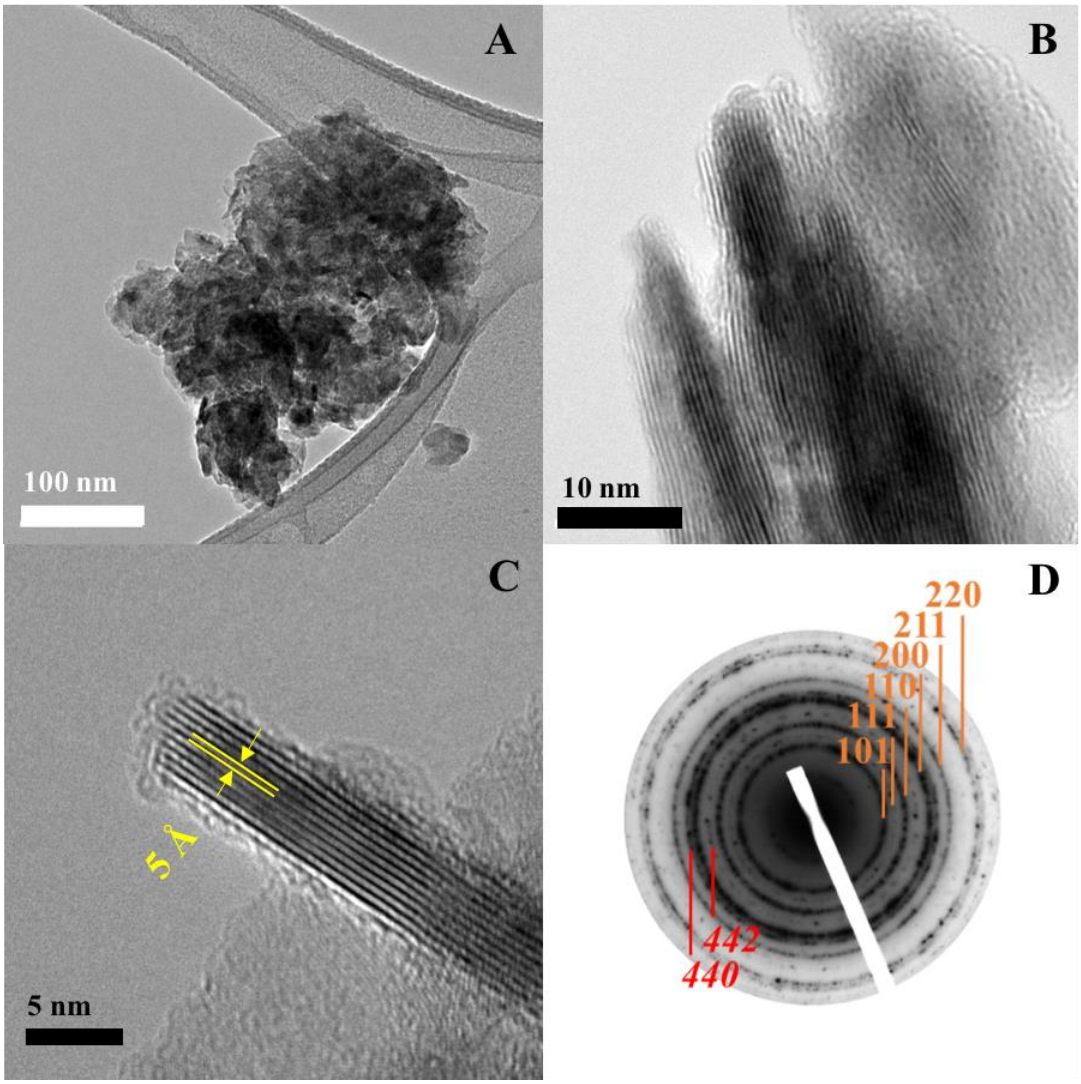


Figure 4.6. FeS with PCE sample, pH 8, seven weeks. (A), (B) and (C) HRTEM images, and (D) SAED pattern of (A). SAED shows the presence of minor greigite (rings produced by mackinawite and greigite are marked by Miller indices in orange and red, respectively).

Three SAED patterns were collected from three randomly selected particles in the FeS control sample. Because all three SAED patterns for the FeS control sample give the same information about the crystal structures, one SAED pattern (Figure 4.4D) is reported. All the SAED pattern of FeS control exhibited weak and diffuse rings, as well as individual spots, produced by FeS, which were marked by

Miller indices in red. This indicates the FeS control sample contains both well-crystalline FeS particles and randomly oriented poorly-crystalline particles (Posfai et al., 1998). Only a few spots but no distinct ring was observed for the (001) plane of FeS.

All the SAED patterns of FeS with TCE sample showed rings corresponding to both FeS and greigite (Posfai et al., 1998), and one example is reported (Figure 4.5D). The rings produced by greigite were not present in the FeS control sample. This suggests greigite is one of the FeS-associated products formed during reaction with TCE, which is consistent with the formation of greigite shown in Reaction 4.1. Although the increase of O percent in the FeS with TCE and PCE samples (Figure 4.3) suggested the possibility of iron (hydr)oxides formation, no rings produced by iron (hydr)oxides were observed in the SAED patterns of the FeS with TCE and PCE samples. Iron (hydr)oxides may be too amorphous or poorly crystalline to produce clear diffracting rings, and/or the weak rings they produce may overlap with the rings produced by mackinawite and greigite. For example, the SAED pattern of two-line ferrihydrite formed upon oxidation of FeS by CT, which is reported in Figure A6B, has two very broad rings: 1.47-1.50 Å (for the (300) plane) and 2.47-2.59 Å (for the (110) plane) (Drits et al., 1993; Jambor and Dutrizac, 1998). These two rings overlap with the rings produced by the (211) plane from mackinawite (1.56 Å) and the (400) plane from greigite (2.47 Å). In this case, even if ferrihydrite was present, its diffraction rings would be too broad and diffuse to be seen, compared to the bright and intense rings produced by mackinawite and greigite. The capture of the diffraction rings produced by two-line ferrihydrite

requires an extremely long exposure time. For example, Janney et al. (2000) used long exposure times ranging from 90 seconds to 180 seconds. The exposure time used in this study was 11 seconds, which would have made it hard to capture the diffraction rings produced by two-line ferrihydrite, even if it was formed in the samples after reaction with TCE and PCE. Figure 4.5C shows FFT pattern obtained from Figure 4.5B using DMS. FFT can provide information of the reciprocal d-spacings presented in HRTEM images. Figure 4.5C also confirmed the presence of greigite in the FeS with TCE sample, consistent with the detection of greigite in Figure 4.5D.

Similar to the SAED patterns of the FeS with TCE sample, all the SAED patterns of the FeS with PCE sample showed rings from mackinawite and greigite (Posfai et al., 1998), and a representative pattern is shown in Figure 4.6D. The formation of greigite is consistent with reaction 4.2. In addition, compared to the FeS control sample (Figures 4.4B and 4.4C), the sheets of the FeS with PCE sample showed pits on the edge of sheets (Figures 4.6B and 4.6C). This may be due to the dissolution of FeS surface. Similar to this well-known oxidative dissolution (Buckley and Woods, 1985; Jeong et al., 2010), the reactions of FeS with TCE and PCE appear to involve oxidative dissolution.

The surface morphology of FeS samples was analyzed using SEM. The experimental setup contained FeS chips and pure phase of TCE and PCE (Figure A1). This setup maximized the molar ratio of TCE and PCE to FeS and avoided altering the surface morphology during sample collection. Small amounts of round particles (but not perfectly round) were observed on the FeS surface after reaction

with TCE (Figures B5 and B6) and PCE (Figures B7 and B8). Similar round particles were also found on the surface of the FeS control sample at the same time (Figures B3 and B4), although in far fewer amounts. No such particles were observed in the FeS control sample that was being placed in pH 8 Tris buffer for 1 hour (Figure B2). EDS data was collected on the round particles and the areas next to them, which contained no such particles (referred to as "the background"). The elemental compositions of the round particles and the background were indistinguishable. Based on the data, it is not possible to reach a conclusion whether these round particles are FeS oxidation products by TCE and PCE. EDS were collected on randomly selected larger areas (not on the small round particles) in order to obtain an average atomic composition of the samples (Figure B9, n=5-6). No changes that were statistically significant were observed among the FeS control and the two FeS samples reacted with TCE and PCE. The O percent in FeS with TCE sample (32 days, Figure B9B) was slightly higher than the FeS control, as well as the FeS with PCE sample. This observation is similar to the EDS results at seven weeks, which were collected using TEM (Figure 4.3). The time (32 days, ~4.5 weeks) is shorter than the time of the EDS results collected using TEM (seven weeks). Thus, it is reasonable fewer changes were observed.

We further investigated the changes on the FeS surface after reaction with TCE and PCE using XPS. XPS is a surface sensitive technique which has a depth resolution on the order of nanometers (1-12 nm). The XPS high resolution scans of the FeS control, FeS with PCE, and FeS with TCE all showed the presence of carbon, nitrogen, oxygen, sulfur, and iron (Table 4.2). Nitrogen is introduced by the

adsorption of Tris buffer ($C_4H_{11}NO_3$) and N_2 in the atmosphere. The FeS surface showed enrichment of Fe and S, as well as the decrease of O, after reaction with TCE and PCE (Table 4.2). The decrease of O observed here is opposite to the EDS results obtained using SEM and TEM. We compared the changes in the atomic ratios of S and O in the samples which were calculated using the Fe atomic percentage as a reference (Table B2, details of the calculation can be found in Chapter 3). The values of Fe:S were similar in the samples that reacted with TCE and PCE versus the control (by both EDS and XPS). However, the values of Fe:O went down in the EDS measurements, while the Fe:O values went up in the XPS measurements. This suggests that the bulk of the samples contained more O after reactions with TCE and PCE compared to the control, while the surface of the samples contained less O compared to the control. One possibility is that the bulk FeS sample was oxidized during the reaction with TCE and PCE, resulting in differences in composition between the bulk and the surface. We do not have a more specific conclusion based on the data.

Table 4.2*. Atomic percent (in %) obtained from XPS high energy resolution spectra

Sample	C	N	O	S	Fe
FeS control	22.0	1.7	16.2	32.4	27.7
FeS with TCE	19.6	1.9	12.6	35.8	30.2
FeS with PCE	17.6	1.9	12.5	35.5	32.5

* This table was copied from a report by Evans Analytical Group (2015), East Windsor, NJ. Atomic percent were normalized to 100% of the elements detected. XPS does not detect H or He.

All the XPS spectra were fit following the procedures described below. First, the ranges of binding energies of possible peaks were estimated by studying the shapes of the raw spectra. Second, the estimated ranges were entered into XPSpeak 4.1 to constrain the positions of the peaks. The binding energy of each peak was calculated by the software, and the best fit of the data was the one that gave the best goodness of fitting (Kwok, 2000). Last, peaks were ascribed to possible species by comparing the calculated binding energies of the peaks to those of the species reported in the literature.

The S 2p spectra were fit using three sets of doublets ($2p_{1/2}$ and $2p_{3/2}$), and the doublets were separated by a spin-orbit splitting of 1.2 eV, and the S $2p_{1/2}$ peak was set to half the area of the S $2p_{3/2}$ peak (Mullet et al., 2002; Wan et al., 2014). After reaction with TCE and PCE, the S 2p spectra shifted to a higher binding energy, indicating oxidation of S by TCE and PCE (Figure 4.7). The oxidation of S may be explained by the formation of more oxidized iron sulfides, such as greigite. Li et al. (2008) studied the transformation of preoxidized mackinawite (2 hours in synthetic air) to greigite after reaction with H_2S, upon the formation of greigite (indicated by XRD results), the S 2p spectrum shifted to a higher binding energy. This shift is similar to what we observed in our XPS results, and this may suggest the formation of greigite on FeS surface after reaction with PCE and TCE. This agrees with our TEM results, as well as Reactions 4.1 and 4.2. There are two possible ways to interpret the fit, which are discussed below, but the fit is nearly the same regardless of what the peaks are called.

In Figure 4.7, the best fit of the data was for the following S $2p_{3/2}$ binding energy: peak S1 at 161.5± 0.1 eV, peak S2 at 162.1 eV, and peak S3 at 163.0± 0.1 eV. The peaks are consistent with the reported binding energies for different S surface species: monosulfide (S^{-2}), disulfide (S_2^{-2}), and polysulfides (S_n^{-2}, $2<n<8$), respectively (Boursiquot et al., 2002; Mullet et al., 2002; Wan et al., 2014) (Table B1). With this approach, the results suggested that there were more disulfide and polysulfides and less monosulfide on the FeS surface after reaction with TCE and PCE compared to the FeS control (Figure 4.7, Table B1). This indicated the formation of S-S bonds at the expense of monosulfide. Two possible reactions are:

$$S^{2-} + S^{2-} \rightarrow S_2^{2-} + 2\,e^- \quad 4.5$$

$$S_{n-1}{}^{2-} + S^{2-} \rightarrow S_n^{2-} + 2\,e^- \quad 4.6$$

These two reactions can donate electrons to the reductive dechlorination of TCE and PCE. Oxidized sulfur species, such as disulfide and polysulfides, are the oxidation products formed during the oxidation of FeS to pyrite (He et al., 2010), as well as the oxidation of pyrrhotite by oxygen (Pratt et al., 1994). During the oxidation of FeS by synthetic air, upon the formation of greigite, the peaks which increased in magnitude were consistent with disulfide and polysulfides in terms of binding energies (Li et al., 2008).

An alternative way to interpret the S spectra fitting is to associate the doublets with iron sulfide minerals (Figure B10). The fitting approach is similar to the aforementioned one, with slight differences in the binding energies. Lennie and Vaughan (1996) reported that the binding energy of S $2p_{3/2}$ peak of mackinawite is 161.8 eV, which may correspond to peak S1 in Figure 4.7; the binding energy of S

$2p_{3/2}$ peak of pyrite is 162.5 eV, which is slightly lower than the binding energy of peak S2 in Figure 4.7. Greigite is an intermediate product formed during the transformation of FeS to pyrite (Benning et al., 2000; Hunger and Benning, 2007; Lan and Butler, 2014), yet no binding energy of S $2p_{3/2}$ peak of greigite was reported. It may be due to the difficulty of separating greigite from FeS, pyrite, and iron (hydr)oxides, which are possible co-occurring minerals during the sample preparations (Rickard and Luther, 2007). We assume the S $2p_{3/2}$ binding energy of greigite is between those of FeS and pyrite, thus the binding energy of S $2p_{3/2}$ peak of greigite was constrained between 161.8 eV and 162.5 eV (Li et al., 2008). The final S $2p_{3/2}$ binding energy of greigite was calculated by XPSpeak 4.1, which gave the best fit of data among the given range. The calculated S $2p_{3/2}$ binding energy of greigite equals 162.1 eV, which is consistent with peak S2 in Figure 4.7. The results from this fit suggested after reaction with TCE and PCE (Figure 10B and 10C), the peak corresponds to greigite and pyrite increased, compared to the FeS control sample (Figure 10A). This indicated the FeS surface may contain more oxidized species such as those in greigite and pyrite. The two approaches gave similar goodness of fit and both suggested the formation of more oxidized iron sulfide minerals, such as greigite, on FeS surface after reaction with TCE and PCE. The results agree with the detection of greigite using SAED.

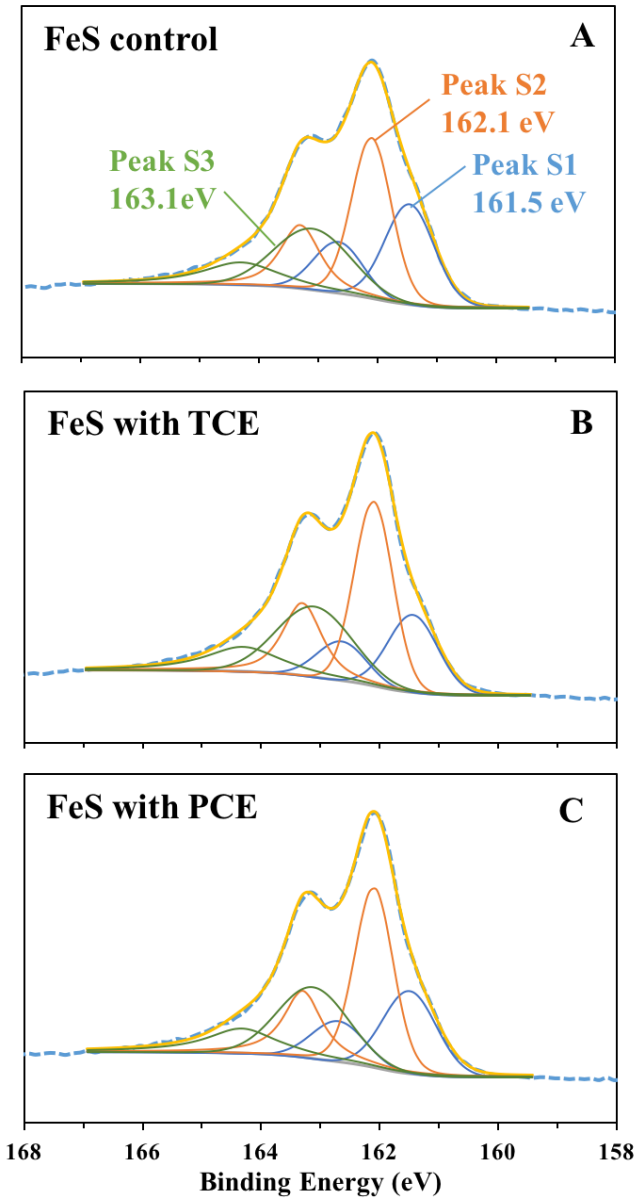


Figure 4.7. The S 2p XPS spectra of FeS surface (peaks correspond to S species), pH 8, seven weeks. (A) FeS control; (B) FeS with TCE; (C) FeS with PCE. Blue dotted lines are experimental data, and yellow lines are corresponding fits.

The shapes of Fe $2p_{3/2}$ spectra of three samples (Figure B11) were very similar, all resemble the reported shape of Fe $2p_{3/2}$ spectrum in lab synthesized FeS (Mullet et al., 2002). The fitting approach for Fe $2p_{3/2}$ spectra reported in Chapter 3

was used to fit the spectra, however, no evidence of Fe oxidation was observed. This may because a very small amount of FeS was reacted.

Compared to the O 1s spectrum of the FeS control sample (Figure 4.8A), the O 1s spectra of the FeS samples reacted with TCE (Figure 4.8B) and PCE (Figure 4.8C) had shoulders on the higher binding energy side. The O 1s spectra were fitted with three peaks centered at 530.0 eV (peak O1), 531.6 eV (peak O2), and 533.2 eV (peak O3). Peak O1 and peak O2 decreased in magnitude, and peak O3 increased in magnitude in the FeS with TCE and PCE samples (Figures 4.8B and 4.8C), compared to the FeS control sample (Figure 4.8A) (Table B1). Peak O1 and peak O2 are ascribed to Fe-O and Fe-OH, respectively (Knipe et al., 1995; Mullet et al., 2002). Peak O3 may be ascribed to Fe-OH_2 or O-C species (Knipe et al., 1995; Mullet et al., 2002). The increase in O-C species corresponds with the increase of C-O species discussed later in this chapter. It is not possible to distinguish these possibilities based on the data here.

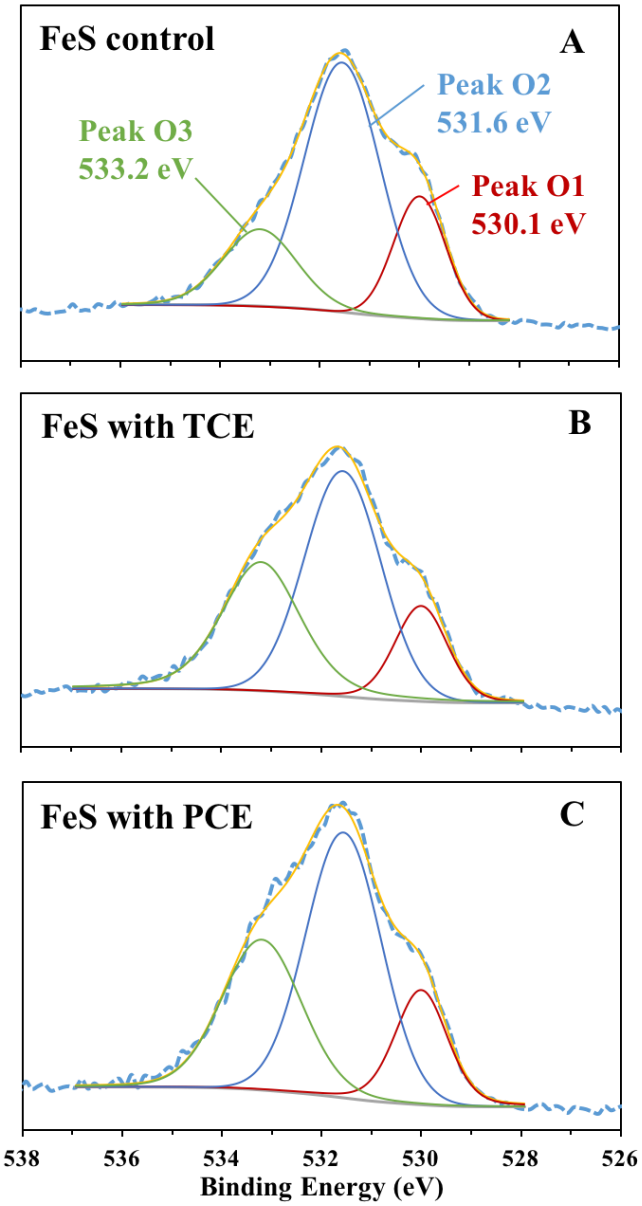


Figure 4.8. The O 1s XPS spectra of FeS surface, pH 8, seven weeks. (A) FeS control; (B) FeS with TCE; (C) FeS with PCE. Blue dotted lines are experimental data, and yellow lines are corresponding fits.

Although most studies of the FeS surface treated C detected on the FeS surface as adventitious carbon or contamination (Mycroft et al., 1995; Boursiquot et al., 2001; Mullet et al., 2002; He et al., 2010), and did not discuss it further, noticeable changes of some carbon species were observed in our study (Figure 4.9,

Table B1). The C 1s spectra were fit with four peaks (Figure 4.9). Peak C1 (282.3 eV) is ascribed to a metal carbide species, and peak C4 (288.5), a highly oxidized carbon species, is ascribed to carbonate or a carboxylate functional group (Miller et al., 2002). These two peaks did not show systematic changes. After reaction with TCE and PCE, peak C3 (286.3 eV) increased in magnitude, while peak C2 (284.8 eV) decreased in magnitude (Figures 4.9B and 4.9C). Peak C2 is ascribed to a hydrocarbon species or a C-C species (Miller et al., 2002). Peak C3 may be ascribed to a C-O species, its increase after reaction with TCE and PCE is consistent with the increase of the O-C species (peak O3) in the O 1s spectra (Figures 4.9B and 4.9C). The possible carbon sources in the samples include Tris buffer, PCE and TCE (Weerasooriya and Dharmasena, 2001), carbonate (or dissolved HCO_3^-) (Miller et al., 2002), and ions of CO, CHO and CO_2 from the XPS vacuum chambers (Miller et al., 2002). In our samples, the unchanged carbide species (peak C1) and carbonate or a carboxylate functional group (peak C4) in all samples may be due to contamination or dissolved carbonate. The decrease in peak C2 and the increase in peak C3 after reactions with TCE and PCE may be due to the oxidation of C-C and/or C-H to C-O species. Although TCE and PCE may adsorb on the FeS surface (Weerasooriya and Dharmasena, 2001), no chloride was detected on the surface (Table 4.2). Thus, the oxidized C species does not come from TCE and PCE. It is possible that Tris buffer is being oxidized, because the concentration of Tris buffer (22 mM) is much higher than the concentrations of TCE and PCE, and this make it more likely a carbon source.

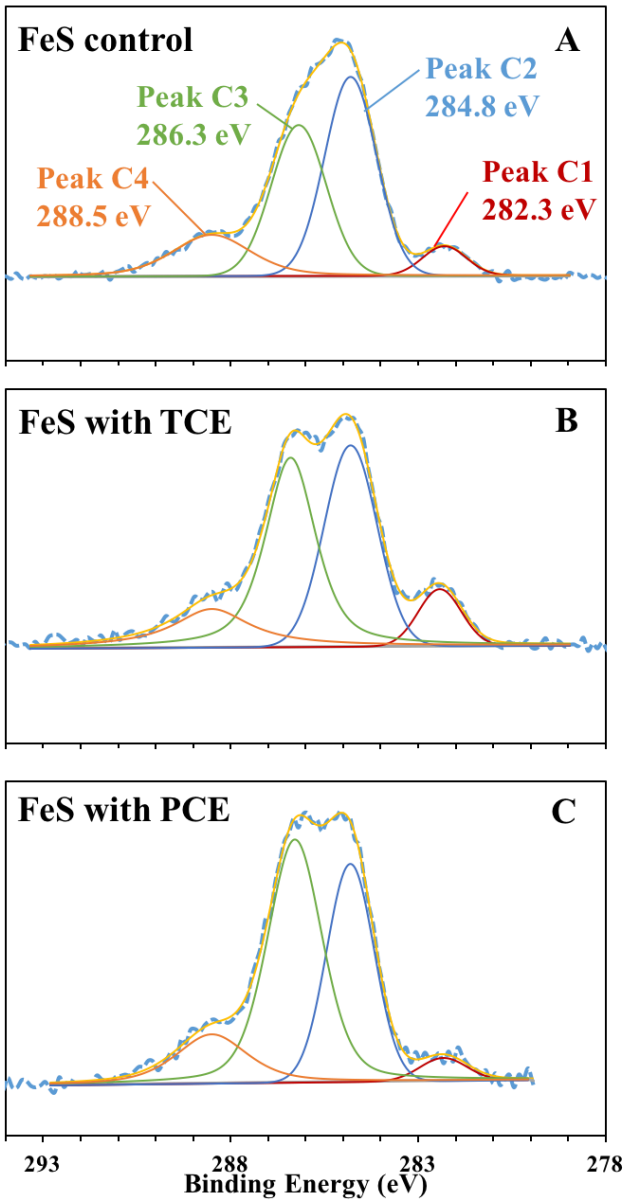


Figure 4.9. The C 1s XPS spectra of FeS surface, pH 8, seven weeks. (A) FeS control; (B) FeS with TCE; (C) FeS with PCE. Blue dotted lines are experimental data, and yellow lines are corresponding fits.

4.4. Conclusion

In this chapter, we studied the oxidation products of FeS formed during reaction with TCE and PCE. Microscopic and spectroscopic solid analytical techniques were employed in the characterization of the FeS-associated products.

These techniques gave in-depth analyses of the FeS oxidation products by TCE and PCE from the bulk mineral particles to the surface species. After reaction with TCE and PCE, SAED results indicated the formation of greigite in the samples. XPS results suggested that the S species on the FeS surface were oxidized by TCE and PCE, while no oxidation of the Fe species was observed. The oxidation of S species may be due to the formation of greigite (Li et al., 2008). The formation of greigite as an oxidation product is consistent with FeS oxidation product by CT, as reported in Chapter 3. Unlike the oxidation of FeS by CT, ferrihydrite was not detected as an oxidation product of FeS by TCE and PCE at seven weeks. It is possible that greigite forms prior to ferrihydrite. It is also possible that the oxidation of FeS by TCE and PCE in seven weeks reacted to a lesser degree compared to the oxidation of FeS by CT in two weeks.

Greigite dissolution produces dissolved Fe^{+2}. Dissolved Fe^{+2} can react with excess S(-II) to precipitate FeS(s). The results indicate that FeS can be regenerated by addition of sulfate to sites under sulfate-reducing conditions.

References

2015. X-Ray photoelectron spectroscopy (XPS)/electron spectroscopy for chemical analysis (ESCA) surface analysis report. East Windsor, NJ: Evans Analytical Group.

Benning, L. G., Wilkin, R. T., and Barnes, H. L. 2000. Reaction pathways in the Fe-S system below 100 degrees C. *Chem Geol* 167 (1-2):25-51.

Boursiquot, S., Mullet, M., Abdelmoula, M., Genin, J. M., and Ehrhardt, J. J. 2001. The dry oxidation of tetragonal FeS_{1-x} mackinawite. *Phys Chem Miner* 28 (9):600-611.

Boursiquot, S., Mullet, M., and Ehrhardt, J. J. 2002. XPS study of the reaction of chromium (VI) with mackinawite (FeS). *Surface and Interface Analysis* 34 (1):293-297.

Buckley, A. N., and Woods, R. 1985. X-Ray photoelectron-spectroscopy of oxidized pyrrhotite surfaces .1. Exposure to Air. *Appl Surf Sc* 22-3 (May):280-287.

Butler, E. C., and Hayes, K. F. 1999. Kinetics of the transformation of trichloroethylene and tetrachloroethylene by iron sulfide. *Environ Sci Technol* 33 (12):2021-2027.

Csakberenyi-Malasics, D., Rodriguez-Blanco, J. D., Kis, V. K., Recnik, A., Benning, L. G., and Posfai, M. 2012. Structural properties and transformations of precipitated FeS. *Chem Geol* 294:249-258.

Doherty, R. E. 2000a. A history of the production and use of carbon tetrachloride, tetrachloroethylene, trichloroethylene and 1,1,1-trichloroethane in the United States: Part 1 - Historical background; Carbon tetrachloride and tetrachloroethylene. *Environ Forensics* 1 (2):69-81.

Doherty, R. E. 2000b. A history of the production and use of carbon tetrachloride, tetrachloroethylene, trichloroethylene and 1,1,1-trichloroethane in the United States: Part 2 - Trichloroethylene and 1,1,1-trichloroethane. *Environ Forensics* 1 (2):83-93.

Drits, V. A., Sakharov, B. A., Salyn, A. L., and Manceau, A. 1993. Structural model for ferrihydrite. *Clay Minerals* 28 (2):185-207.

Gossett, J. M. 1987. Measurement of henrys law constants for C1 and C2 chlorinated hydrocarbons. *Environ Sci Technol* 21 (2):202-208.

He, Y. T., Wilson, J. T., Su, C., and Wilkin, R. T. 2015. Review of abiotic degradation of chlorinated solvents by reactive iron minerals in aquifers. *Ground Water Monit R* 35 (3):57-75.

He, Y. T., Wilson, J. T., and Wilkin, R. T. 2010. Impact of iron sulfide transformation on trichloroethylene degradation. *Geochim Cosmochim Ac* 74 (7):2025-2039.

Hunger, S., and Benning, L. G. 2007. Greigite: a true intermediate on the polysulfide pathway to pyrite. *Geochem T* 8:1-20.

Hyun, S. P., and Hayes, K. F. 2009. Feasibility of using in situ FeS precipitation for TCE degradation. *J Environ Eng-Asce* 135 (10):1009-1014.

Jambor, J. L., and Dutrizac, J. E. 1998. Occurrence and constitution of natural and synthetic ferrihydrite, a widespread iron oxyhydroxide. *Chem Rev* 98 (7):2549-2585.

Janney, D. E., Cowley, J. M., and Buseck, P. R. 2000. Transmission electron microscopy of synthetic 2-and 6-line ferrihydrite. *Clays Clay Miner* 48 (1):111-119.

Jeong, H. Y., Han, Y. S., Park, S. W., and Hayes, K. F. 2010. Aerobic oxidation of mackinawite (FeS) and its environmental implication for arsenic mobilization. *Geochim Cosmochim Ac* 74 (11):3182-3198.

Jeong, H. Y., and Hayes, K. F. 2007. Reductive dechlorination of tetrachloroethylene and trichloroethylene by mackinawite (FeS) in the presence of metals: Reaction rates. *Environ Sci Technol* 41 (18):6390-6396.

Jeong, H. Y., Lee, J. H., and Hayes, K. F. 2008. Characterization of synthetic nanocrystalline mackinawite: Crystal structure, particle size, and specific surface area. *Geochim Cosmochim Ac* 72 (2):493-505.

Kennedy, L. G., Everett, J. W., Becvar, E., and Defeo, D. 2006a. Field-scale demonstration of induced biogeochemical reductive dechlorination at Dover Air Force Base, Dover, Delaware. *J Contam Hydrol* 88 (1-2):119-136.

Kennedy, L. G., Everett, J. W., and Gonzales, J. 2006b. Assessment of biogeochemical natural attenuation and treatment of chlorinated solvents, Altus Air Force Base, Altus, Oklahoma. *J Contam Hydrol* 83 (3-4):221-236.

Knipe, S. W., Mycroft, J. R., Pratt, A. R., Nesbitt, H. W., and Bancroft, G. M. 1995. X-Ray photoelectron spectroscopic study of water-adsorption on iron sulfide minerals. *Geochim Cosmochim Ac* 59 (6):1079-1090.

Kwok, R. W. M., XPSPEAK v.4.1. Manual, Hong Kong.

Lan, Y., and Butler, E. C. 2014. Monitoring the transformation of mackinawite to greigite and pyrite on polymer supports. *Appl Geochem* 50:1-6.

Lennie, A. R., and Vaughan, D. J. 1996. Spectroscopic studies of iron sulfide formation and phase relations at low temperatures. *Mineral Spectroscopy: A Tribute to Roger G. Burns* 5:117-131.

Li, Y., van Santen, R. A., and Weber, T. 2008. High-temperature FeS-FeS_2 solid-state transitions: Reactions of solid mackinawite with gaseous H_2S. *J Solid State Chem* 181 (11):3151-3162.

Liang, X., Dong, Y., Kuder, T., Krumholz, L. R., Philp, R. P., and Butler, E. C. 2007. Distinguishing abiotic and biotic transformation of tetrachloroethylene

and trichloroethylene by stable carbon isotope fractionation. *Environ Sci Technol* 41 (20):7094-7100.

Majzlan, J., Navrotsky, A. l., and Schwertmann, U. 2004. Thermodynamics of iron oxides: Part III. Enthalpies of formation and stability of ferrihydrite (~$Fe(OH)_3$), schwertmannite (~$FeO(OH)_{3/4}(SO_4)_{1/8}$), and ε-$Fe_2O_3$. *Geochim Cosmochim Ac* 68 (5):1049-1059.

Miller, D. J., Biesinger, M. C., and McIntyre, N. S. 2002. Interactions of CO_2 and CO at fractional atmosphere pressures with iron and iron oxide surfaces: one possible mechanism for surface contamination? *Surface and Interface Analysis* 33 (4):299-305.

Mitchell, D. R. G. 2008. DiffTools: Electron diffraction software tools for DigitalMicrograph ™. *Microsc Res Techniq* 71 (8):588-593.

Moran, M. J., Zogorski, J. S., and Squillace, P. J. 2007. Chlorinated solvents in groundwater of the United States. *Environ Sci Technol* 41 (1):74-81.

Morel, F. M., and Hering, J. G. 1993. *Principles and applications of aquatic chemistry*: John Wiley & Sons.

Mullet, M., Boursiquot, S., Abdelmoula, M., Genin, J. M., and Ehrhardt, J. J. 2002. Surface chemistry and structural properties of mackinawite prepared by reaction of sulfide ions with metallic iron. *Geochim Cosmochim Ac* 66 (5):829-836.

Mullet, M., Boursiquot, S., and Ehrhardt, J. J. 2004. Removal of hexavalent chromium from solutions by mackinawite, tetragonal FeS. *Colloid Surface A* 244 (1-3):77-85.

Mycroft, J. R., Nesbitt, H. W., and Pratt, A. R. 1995. X-Ray photoelectron and Auger electron spectroscopy of air-oxidized pyrrhotite - Distribution of oxidized species with depth. *Geochim Cosmochim Ac* 59 (4):721-733.

Posfai, M., Buseck, P. R., Bazylinski, D. A., and Frankel, R. B. 1998. Reaction sequence of iron sulfide minerals in bacteria and their use as biomarkers. *Science* 280 (5365):880-883.

Pratt, A. R., Muir, I. J., and Nesbitt, H. W. 1994. X-Ray photoelectron and Auger-electron spectroscopic studies of pyrrhotite and mechanism of air oxidation. *Geochim Cosmochim Ac* 58 (2):827-841.

Rickard, D., and Luther, G. W. 2007. Chemistry of iron sulfides. *Chem Rev* 107 (2):514-562.

Rickard, D. T. 1969. The chemistry of iron sulphide formation at low temperatures. *Stockh Contrib Geol* 20:67-95.

Shen, H., and Wilson, J. T. 2007. Trichloroethylene removal from groundwater in flow-through columns simulating a permeable reactive barrier constructed with plant mulch. *Environ Sci Technol* 41 (11):4077-4083.

Smith, F. 1999. *Industrial applications of X-ray diffraction*. Boca Raton, FL: CRC Press.

Wan, M., Shchukarev, A., Lohmayer, R., Planer-Friedrich, B., and Peiffer, S. 2014. Occurrence of surface polysulfides during the interaction between ferric (hydr)oxides and aqueous sulfide. *Environ Sci Technol* 48 (15):8932-8932.

Weerasooriya, R., and Dharmasena, B. 2001. Pyrite-assisted degradation of trichloroethene (TCE). *Chemosphere* 42 (4):389-396.

Chapter 5

Conclusions and Recommendations

5.1. Conclusions

This doctoral dissertation investigated the oxidation products of mackinawite (FeS) formed during dechlorination of chlorinated aliphatic contaminants. This project identified the FeS-associated products formed during reactions with carbon tetrachloride (CT), trichloroethylene (TCE), and tetrachloroethylene (PCE). The conclusions from this project provide insights into the design and application of FeS in the in situ remediation of CT, TCE, and PCE, as well as help to evaluate the possibility of FeS in situ regeneration. Specific conclusions of each task are described below.

Task 1: Monitor the transformation of FeS to greigite and pyrite under geochemical conditions similar to those in pristine or contaminated aquifers

In the first task, the transformation of FeS to greigite and pyrite was studied using immobilized FeS particles. Poly (methyl methacrylate) (PMMA) supports and silicone-based adhesive are suitable for studying mineralogical changes in iron-sulfur minerals at mildly elevated temperatures in pristine and contaminated environments. Such supports can be used for particles with dimensions ranging from 100 nm to 2 μm. With the use of the PMMA supports, the mineralogical changes that happened on the mineral surface can be monitored without altering the crystal structures and sizes.

At mildly elevated temperature, FeS transforms to greigite and pyrite. The similarities in sizes between most crystals over the course of the transformation

from FeS to pyrite, as well as the coexistence of solids with morphologies and elemental compositions characteristic of FeS, greigite, and pyrite, are consistent with a solid state transformation. Much smaller pyrite crystals were formed, which may have resulted from direct nucleation from solution.

Task 2: Characterize the FeS oxidation products formed upon reductive dechlorination of CT

In the second task, the FeS-associated products formed during reaction between FeS and CT at pH 7 and 8 were studied. Greigite is the major product formed during reaction between FeS and CT at pH 7. At pH 8, reaction of FeS with CT led to the formation of poorly crystalline two-line ferrihydrite with diameters between 50-400 nm on the FeS surface and in solution; far fewer such particles were observed at pH 7. During the reactions with CT, Fe(II)-S species was oxidized into Fe(III)-O and Fe(III)-S, while no evidence for the S oxidation was observed within two weeks.

Task 3: Characterize the FeS oxidation products formed upon reductive dechlorination of TCE and PCE

In the third task, the oxidation products of FeS during reaction with TCE and PCE at pH 8 were studied. Results indicated that the FeS oxidation products by TCE and PCE were mainly greigite. Different from the FeS oxidation by CT, S species on the FeS surface was oxidized during the dechlorination of TCE and PCE by FeS, while no oxidation of Fe species was observed in seven weeks. The bulk of the samples contained more O after reactions with TCE and PCE compared to the control, while the surface of the samples contained less O compared to the control.

Both ferrihydrite and Fe^{+2}, which is a product of greigite dissolution, can react with dissolved HS^- to form FeS, suggesting that, after oxidation by chlorinated aliphatic contaminants, FeS can be regenerated by addition or microbial generation of sulfide.

5.2. Recommendations for future work

The results from this dissertation advanced our understanding of the FeS oxidation products formed during reductive dechlorination of CT, TCE, and PCE using FeS. Beside the regeneration of FeS from the FeS oxidation products formed during reductive dechlorination, recommended future work includes but is not limited to (1) investigating the dechlorination ability of stabilized FeS; and (2) characterizing the surface of greigite. Details of the recommended future work are discussed below.

5.2.1. Dechlorination ability of stabilized FeS

The size of synthesized FeS usually falls into a range of 20-400 nm (Wolthers et al., 2003). The sizes of FeS particles can grow larger due to flocculation, and make the particles subject to settling. Large FeS particles may not be suitable to use in the in situ remediation sites, such as permeable reactive barriers, due to the poor deliverability of large FeS particles. A stabilizer can improve the dispersion of nanoparticles through creating a layer on nanoparticles that can either produce stronger repulsion between FeS particles (and between FeS particles and surrounding soil materials), or impede particle attractions. Low-cost polysaccharides, such as starch and carboxymethyl cellulose, have been found highly effective in

stabilizing nanoparticles (He et al., 2007; Xiong et al., 2009; He et al., 2010; Liu et al., 2015).

Stabilized FeS has been reported to immobilize mercury in field soil and sediment (Xiong et al., 2009; Gong et al., 2012), and effectively remove Cr(VI) (Wang et al., 2011). Stabilized Fe-Pd nanoparticles were reported to enhance the dechlorination of TCE in soil and groundwater (He et al., 2007). Very little is known about the dechlorination ability of stabilized FeS particles. The reductive dechlorination ability of stabilized FeS can be tested by conducting lab-scale experiments.

5.2.2. Surface characterization of greigite

The surface characteristics of FeS and pyrite have been well studied, including surface morphology and surface species (Wang and Morse, 1996; Herbert et al., 1998; Wolthers et al., 2003). However, the surface characteristic of greigite, the intermediate product formed during the transformation from FeS to pyrite, has not been well studied. This may be due to the difficulty of separating greigite from FeS, pyrite, and iron (hydr)oxides, which are possible co-occurring minerals during greigite formation (Li et al., 2008). In Chapter 2, it is also reported that greigite, FeS, and ferrihydrite coexist in the surface region of FeS after reaction with CT. The greigite synthesis methods need to be controlled and tested carefully, in order to obtain high purity greigite. Surface characterization of greigite may include studies on the bonding environment and the binding energies of surface components of greigite using X-ray photoelectron spectroscopy. It would also be interesting to compare the differences among greigite samples that are prepared under different

temperatures. Because temperature was reported to be an important factor during the transformation from FeS to greigite and pyrite (Hunger and Benning, 2007), thus it may also influence the surface chemistry of greigite. It would be beneficial to compare the bonding environment and the binding energies of surface components of mackinawite, greigite, and pyrite. The possible differences may provide evidence for the oxidation kinetics of Fe species and S species during the transformation from mackinawite to pyrite, with greigite as an intermediate product.

References

Gong, Y. Y., Liu, Y. Y., Xiong, Z., Kaback, D., and Zhao, D. Y. 2012. Immobilization of mercury in field soil and sediment using carboxymethyl cellulose stabilized iron sulfide nanoparticles. *Nanotechnology* 23 (29):294007.

He, F., Zhao, D. Y., Liu, J. C., and Roberts, C. B. 2007. Stabilization of Fe-Pd nanoparticles with sodium carboxymethyl cellulose for enhanced transport and dechlorination of trichloroethylene in soil and groundwater. *Ind Eng Chem Res* 46 (1):29-34.

He, F., Zhao, D. Y., and Paul, C. 2010. Field assessment of carboxymethyl cellulose stabilized iron nanoparticles for in situ destruction of chlorinated solvents in source zones. *Water Res* 44 (7):2360-2370.

Herbert, R. B., Benner, S. G., Pratt, A. R., and Blowes, D. W. 1998. Surface chemistry and morphology of poorly crystalline iron sulfides precipitated in media containing sulfate-reducing bacteria. *Chem Geol* 144 (1-2):87-97.

Hunger, S., and Benning, L. G. 2007. Greigite: a true intermediate on the polysulfide pathway to pyrite. *Geochem T* 8:1-20.

Li, Y., van Santen, R. A., and Weber, T. 2008. High-temperature FeS-FeS_2 solid-state transitions: Reactions of solid mackinawite with gaseous H_2S. *J Solid State Chem* 181 (11):3151-3162.

Liu, W., Tian, S., Zhao, X., Xie, W., Gong, Y., and Zhao, D. 2015. Application of stabilized nanoparticles for in situ remediation of metal-contaminated soil and groundwater: A critical aeview. *Current Pollution Reports* 1 (4):280-291.

Wang, Q. W., and Morse, J. W. 1996. Pyrite formation under conditions approximating those in anoxic sediments .1. Pathway and morphology. *Mar Chem* 52 (2):99-121.

Wang, X., Liu, J., Zhao, D., and Song, X. 2011. Preparation of CMC-stabilized FeS nanoparticles and their enhanced performance for Cr (VI) Removal. *Adv Mat Res* 287:96-99.

Wolthers, M., Van der Gaast, S. J., and Rickard, D. 2003. The structure of disordered mackinawite. *Am Mineral* 88 (11-12):2007-2015.

Xiong, Z., He, F., Zhao, D. Y., and Barnett, M. O. 2009. Immobilization of mercury in sediment using stabilized iron sulfide nanoparticles. *Water Res* 43 (20):5171-5179.

Appendix A

Supporting Information for Chapter 3

A1. FeS synthesis

In experiments that measured the kinetics of CT transformation by FeS and the formation of dissolved reaction products, 1.15 mL of 0.025 M Na_2S solution and 1.15 mL of 0.025 M $FeCl_2$ solution were added into a serum bottle containing 1 mL of Tris buffer, diluted with nanopure water to 9 mL to avoid headspace, then left inside the anaerobic chamber for three days. During these three days, the FeS was washed three times to remove background salts by carefully removing 6 mL of the supernatant, adding 6 mL of fresh pH buffer, and shaking the serum bottles for 30 s. The fresh buffer was allowed to equilibrate with FeS overnight before being removed and replaced.

A2. Analytical methods

For GC analysis, 30 μL of the filtered supernatant were added to 970 μL of isooctane (Fisher, ACS grade) in 2 mL GC autosampler vials. Vials were sealed with screw caps containing Teflon lined septa and placed on an oscillating shaker (50 reversals per min) for 15 min. CT and CF were measured in the isooctane extract using a Shimadzu gas chromatograph (GC-17A) with an electron capture detector and a 30 m J&W Scientific DB-624 column (30 m×0.53 mm×3 μm), One microliter of the isooctane phase was analyzed by the GC-17A. The initial GC oven temperature was 40 °C, ramped at a rate of 5 °C per min to 55 °C, and then ramped at a rate of 30 °C per min to 180 °C. The injector temperature was 250 °C, and the detector temperature was 200 °C. Helium was the carrier gas and argon/methane

was the makeup gas. Isooctane-extracted samples were prepared in duplicate, each duplicate sample was measured once, and the concentrations averaged.

A3. Chloride mass balance

Dissolved Cl^- is formed from the dechlorination reactions shown in Reactions 3.1-3.6 in the main part of the paper. For all known CT dechlorination products except CF (and DCM, which was not detected), dechlorination of one mole of CT leads to four moles of Cl^-, while transformation of CT to CF yields one mole of Cl^-. Based on this, a mass balance on Cl^- can be written:

$$[Cl^-]_t = 4[CT]_0 - 4[CT]_t - 3[CF]_t \qquad \text{S1}$$

where the subscripts "t" and "0" denote concentrations at times t and zero, respectively. The first term on the right hand side of this equation represents the Cl^- released to solution from CT dechlorination, while the second and third terms represent the Cl^- still "contained" in unreacted CT and in CF. Plots of the right hand side versus the left hand side of Equation S1 (Figure A3) have slopes close to one for both pH 7 and 8, indicating that most products of CT dechlorination were completely dechlorinated. Small deviations from slopes of one could be due to incomplete recovery of Cl^- due to adsorption, or volatilization losses of unreacted CT (Hanoch, 2003).

A4. Characterization of FeS by XRD

XRD analyses were performed in the School of Geology and Geophysics at the University of Oklahoma using a Rigaku Ultima IV powder X-ray diffractometer. Cu-K-alpha radiation (40 kV, 44 mA) was used with a graphite monochromator and scintillation detector to maximize resolution. Data was collected with a start and end

angle 5°/2θ and 70°/2θ respectively, step size of 0.02° (2θ), and 2 seconds per step. Data analysis was completed using JADE with the ICDD (International Centre for Diffraction Data) powder diffraction file 4+ (PDF4+) database.

A5. Characterization of FeS by XPS and XPS spectra analysis

Prior to analysis, the dried FeS particles were stored in sealed serum bottles, enclosed in three plastic zip bags under an atmosphere of 95% N_2 and 5% H_2, and shipped via next morning delivery to Evans Analytical Group, East Windsor, NJ. Upon receipt, the FeS particles were opened inside a glove bag and transferred to the XPS chamber under nitrogen in an inert transfer vessel. The analysis was done with a PHI 5701 LSci instrument, a monochromatic Al K_α source (1486.6 eV) and an analysis area of 2.0 × 0.8 mm. Both survey spectra and high energy resolution spectra (Fe $2p_{3/2}$, S 2p, O 1s, C 1s, N 1s, Br 3d) were collected. Charge correction was done with C 1s species, set at 284.8 eV.

The XPS spectra were fit using XPSpeak41, and the background was subtracted using a Shirley baseline technique. The Fe $2p_{3/2}$ spectrum (Figure 3.4A and 3.4C) were fit using Fe(II)-S, Fe(II)-O, Fe(III)-S, and Fe(III)-O. Fe(II)-S has no multiplets but one peak that was set at 707.3 eV according to Herbert et al. (1998). The single peak of Fe(II)-O was set at 708 eV (Mullet et al., 2002). Fe(III)-S and Fe(III)-O were decomposed into four peaks each, and each peak in the resulting multiplets was separated by 1 eV (Mullet et al., 2002). The peak with the lowest binding energy in the Fe(III)-S multiplets was set to 708.5 eV, while the peak with the lowest binding energy in the Fe(III)-O multiplets was set to 711.0±0.1 eV (Boursiquot et al., 2002). The full width at half-maximum of the Fe(III) peaks was

set at 2.0 eV, and the ratios of the peak areas to the main peak were set to 0.66, 0.35, and 0.11 (Boursiquot et al., 2002).

The S 2p spectra (Figure 3.4B and 3.4D) were fit with doublets ($2p_{1/2}$ and $2p_{3/2}$) that were separated by a spin-orbit splitting of 1.2 eV, and the S $2p_{1/2}$ peak was set to half the area of the S $2p_{3/2}$ peak. The S 2p spectra were fit using three species: monosulfide (S^{-2}) at 161.5 eV, disulfide (S_2^{-2}) at 162.2 eV, and polysulfides (S_n^{-2}, $2<n<8$) (Rickard and Luther, 2007) at 163.1 eV (Mullet et al., 2002; Wan et al., 2014).

A6. Eh-pH diagram

An Eh-pH diagram was constructed using HSC Chemistry 6, considering the solid phases species detected in our experiments, including FeS, greigite, and ferrihydrite, as well as dissolved Fe(II), Fe(III), and S(-II), all at 25°C (Figure A7). Pyrite and Fe(III) (hydr)oxides other than ferrihydrite, such as goethite and hematite, were not considered. The total concentrations of Fe(II) and S(-II) used in the experiments for XRD, TEM/SAED and XPS (1.6×10^{-3} M) were assumed. Values of ΔG_f^0 used to construct the diagram are listed in Table A3. The stability fields for the metastable minerals greigite and ferrihydrite shown in the diagram (and detected in our experiments) were only present when more thermodynamically stable minerals (e.g., pyrite, goethite, and hematite) were excluded.

A7. Coexistence of FeS and $FeCO_3$ in sulfate-reducing conditions

As part of the thermodynamic analysis of stable and metastable minerals in the Fe(II)-S(-II) system, MINEQL+ v. 4.6 was used to identify the conditions where $FeCO_3$(s) might precipitate along with FeS(s) and thereby constitute an important

Fe(II) solid phase. A total Fe(II) concentration of 5×10^{-5} M and a total S(II) concentration of 3×10^{-4} M were selected from reported concentrations at iron-reducing and sulfate-reducing sites (Chapelle et al., 2009). FeS(s) and $FeCO_3$(s) were set as "dissolved solids" that would precipitate only above their respective solubility limits. The total carbonate concentration $[CO_3]_{total}$ was set to an environmentally relevant concentration of 10^{-3} M, and the simulated pH was varied from 0-14. Under these conditions—specifically an excess of S(-II) to Fe(II) — $FeCO_3$(s) does not coexist with FeS(s) (Figure A8) due to the strong driving force for FeS(s) formation.

Table A1. Concentrations of FeS and CT used in different experimental setups

	FeS (mM)	CT (mM)
Experiments to measure dissolved species over time (kinetic experiments)	3	0.6
Experiments to monitor surface morphology changes (SEM analysis with FeS chips, Fig. S1)	3	2.1
Experiment to study mineral phases and surface species changes (XRD, TEM/SAED, and XPS analyses, dialysis tubing setup, Fig. S2)	1.6	2.1

Table A2*. Relative atomic percentage** (in %) obtained from XPS high energy resolution spectra of FeS surface after reaction with CT for 14 days at pH 8. 0.0016 M FeS; 0.022 M Tris buffer; $(2.1\pm0.2)\times10^{-3}$ M CT.

Sample	C	N	O	S	Fe	Br
FeS no-CT control	18.5	2	19.4	33.8	26.3	<0.1
FeS with CT	23.5	3.3	33.8	21	17.7	0.8

*This table was reproduced with permission from Evans Analytical Group, East Windsor, NJ (2015).
**Normalized to 100% of the elements detected. XPS does not detect H or He. N and Br were from the Tris buffer. A less than symbol "<" indicates accurate quantification cannot be made due to weak signal intensity. C is adventitious carbon.

Table A3*. Standard state free energies of formation used for Eh-pH diagram for the Fe-S-H_2O system at 25°C (Figure A7).

	ΔG_f^0 (kJ/mol)
FeS (s) (mackinawite)	-88.43 (Benning et al., 2000)
Fe_3S_4 (s) (greigite)	-290.40 (Benning et al., 2000)
$Fe(OH)_2$ (s)	-486.50
$Fe(OH)_3$ (s) (2-line ferrihydrite)	-708.50 (Majzlan et al., 2004)
Fe^{+2}	-82.88
Fe^{+3}	-8.56
$FeOH^+$	-277.40
$FeOH^{+2}$	-233.30
$Fe(OH)_2^+$	-450.50
$Fe(OH)_3^0$	-648.30
$Fe(OH)_4^-$	-833.83
H_2S (aq)	-27.70
HS^-	12.20
S^{-2}	85.90
H_2O (l)	-237.14

*Unless otherwise stated, all data are from Drever (1997).

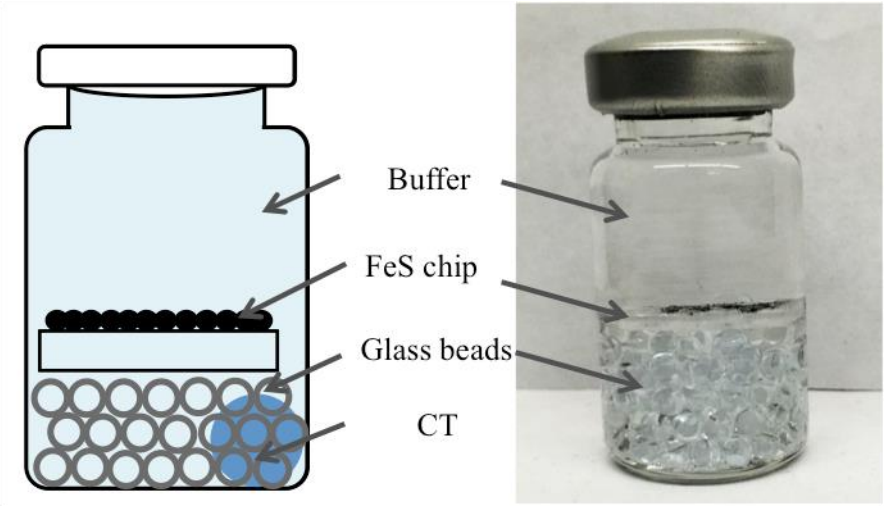


Figure A1. Experimental setup for preparing samples for SEM analysis using FeS chips. CT is transparent and not visible in the photo on the right.

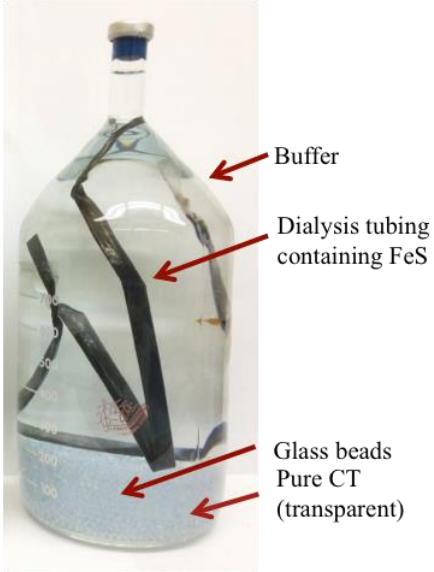


Figure A2. Experimental setup for XRD, TEM/SAED, and XPS analyses.

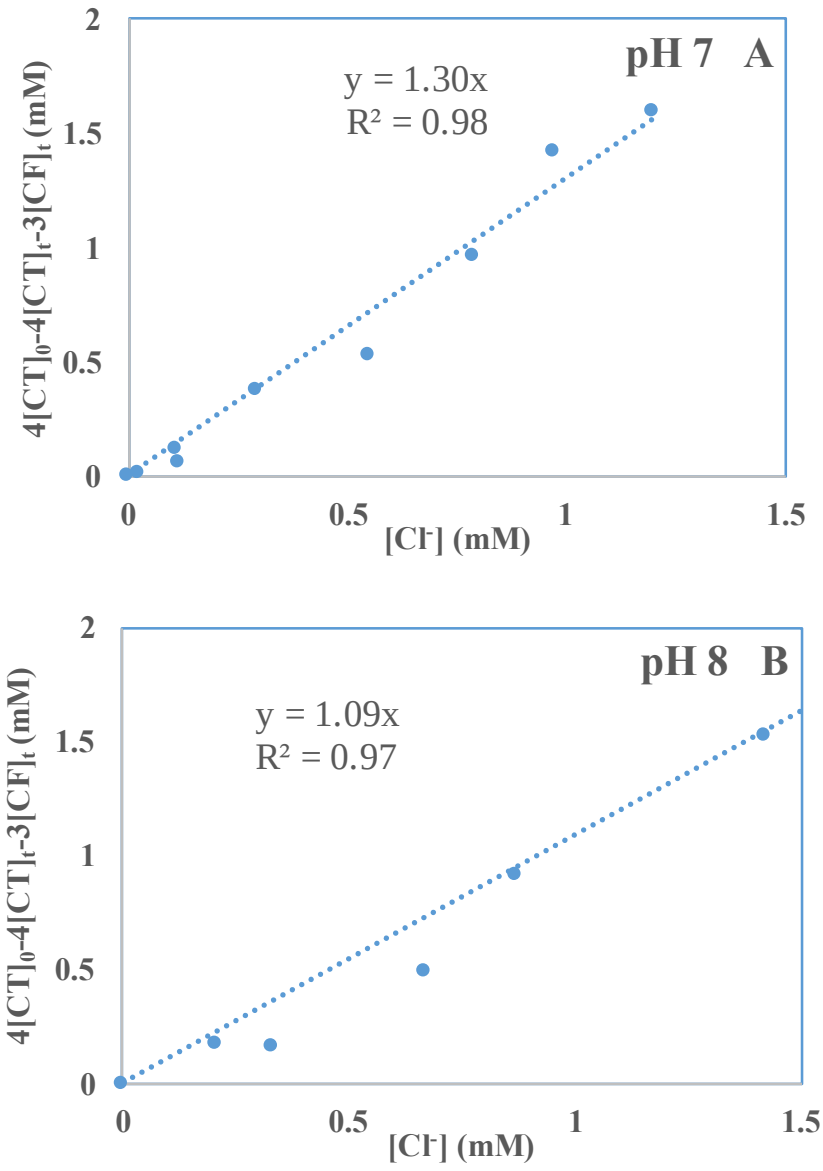


Figure A3. Plots of $4[CT]_0 - 4[CT]_t - 3[CF]_t$ versus $[Cl^-]$ during CT reduction at (A) pH 7 and (B) pH 8. 0.003 M FeS; 0.022 M Tris buffer; $C_{0,\,CT} = 6\times10^{-4}$ M.

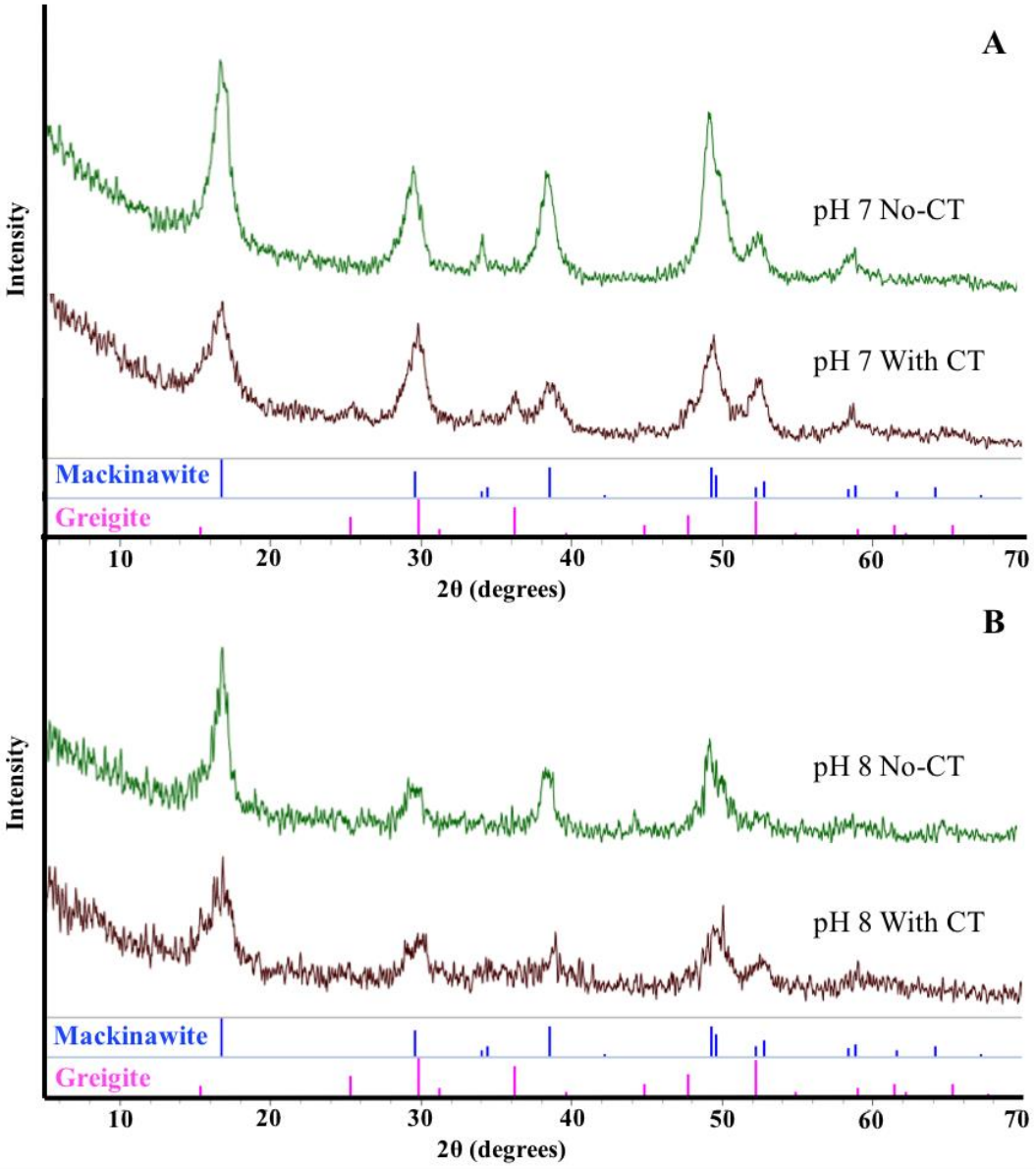


Figure A4. XRD patterns of FeS samples (14 days) (A) pH 7; (B) pH 8. 0.0016 M FeS; 0.022 M Tris buffer; $(2.1\pm0.2)\times10^{-3}$ M CT. Data for mackinawite and greigite are from the International Centre for Diffraction Data (ICDD) powder diffraction file 4+ (PDF4+) database.

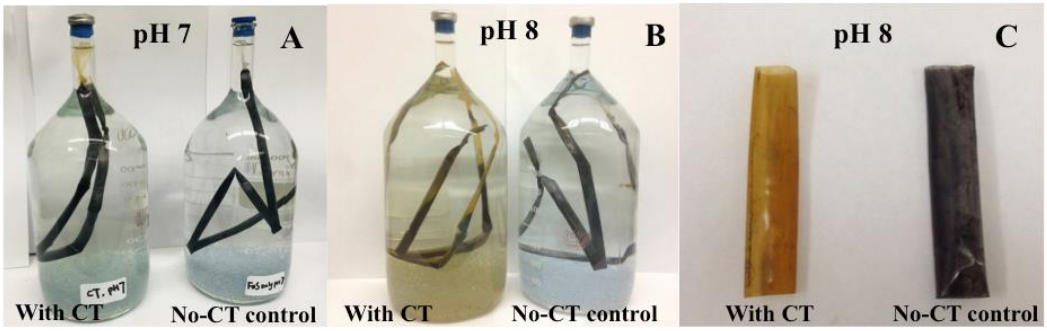


Figure A5. Color comparisons of FeS experiment systems and dialysis tubing at 14 days. (A) pH 7; (B) pH 8; (C) dialysis tubing at pH 8. 0.022 M Tris buffer, 0.0016 M FeS, $(2.1\pm0.2)\times10^{-3}$ M CT.

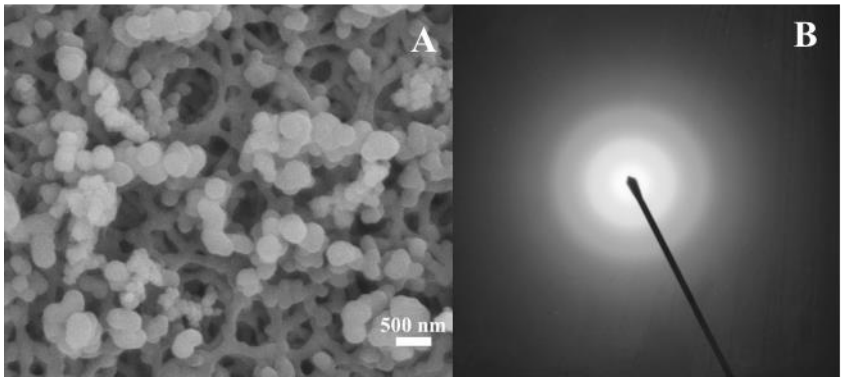


Figure A6. Particles from outside the dialysis tubing after reaction with CT at pH 8 for 14 days. (A) SEM image of particles on filter paper; (B) SAED pattern. 0.0016 M FeS; 0.022 M Tris buffer; $(2.1\pm0.2)\times10^{-3}$ M CT.

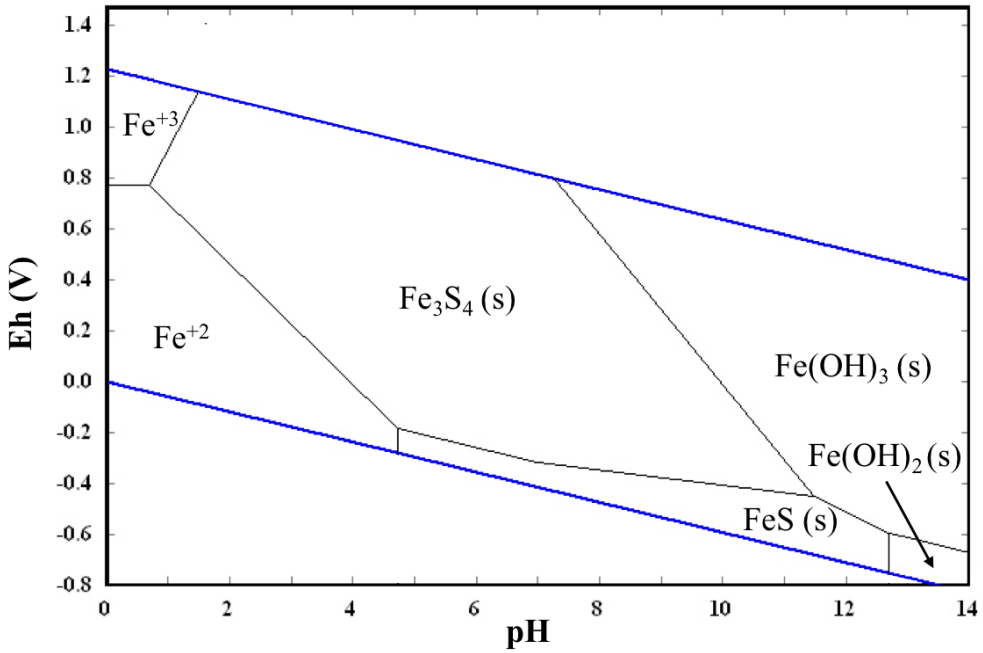


Figure A7. Eh-pH diagram for the Fe-S-H_2O system at 25°C, assuming ferrihydrite as the ferric (hydr)oxide phase, and $[Fe]_{total}= [S]_{total}=1.6\times10^{-3}$ M (which equals to the FeS concentration used in experiments for XPS, XRD, TEM, and SAED analyses). Blue lines are boundaries for the stability field of H_2O.

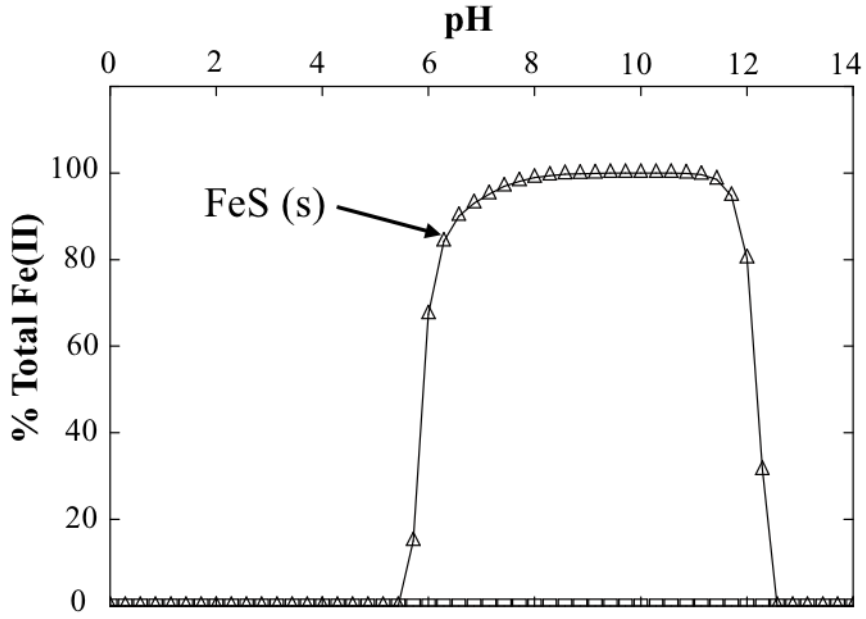


Figure A8. FeS(s) concentration as percent of total Fe(II). Total carbonate concentration $[CO_3]_{total} = 10^{-3}$ M, total Fe(II) = 5×10^{-5} M, and total S(-II) = 3×10^{-4} M. Both FeS(s) and $FeCO_3$(s) were considered in the equilibrium calculations, but $FeCO_3$(s) never equaled a value above zero, and is therefore invisible in this figure. Dissolved species are not shown for clarity.

References

2015. X-Ray photoelectron spectroscopy (XPS)/electron spectroscopy for chemical analysis (ESCA) surface analysis report. East Windsor, NJ: Evans Analytical Group.

Benning, L. G., Wilkin, R. T., and Barnes, H. L. 2000. Reaction pathways in the Fe-S system below 100 degrees C. *Chem Geol* 167 (1-2):25-51.

Boursiquot, S., Mullet, M., and Ehrhardt, J. J. 2002. XPS study of the reaction of chromium (VI) with mackinawite (FeS). *Surf Interface Anal* 34 (1):293-297.

Chapelle, F. H., Bradley, P. M., Thomas, M. A., and McMahon, P. B. 2009. Distinguishing iron-reducing from sulfate-reducing conditions. *Ground Water* 47 (2):300-305.

Drever, J. I. 1997. *The geochemistry of natural waters. 3rd, ed.*: Prentice Hall New Jersey.

Hanoch, R. J. 2003. Abiotic reductive dechlorination of carbon tetrachloride by iron sulfide coatings on iron minerals. Master, University of Oklhoma

Herbert, R. B., Benner, S. G., Pratt, A. R., and Blowes, D. W. 1998. Surface chemistry and morphology of poorly crystalline iron sulfides precipitated in media containing sulfate-reducing bacteria. *Chem Geol* 144 (1-2):87-97.

Majzlan, J., Navrotsky, A., and Schwertmann, U. 2004. Thermodynamics of iron oxides: Part III. Enthalpies of formation and stability of ferrihydrite ($\sim Fe(OH)_3$), schwertmannite ($\sim FeO(OH)_{3/4}(SO4)_{1/8}$), and ε-Fe_2O_3. *Geochim Cosmochim Ac* 68 (5):1049-1059.

Mullet, M., Boursiquot, S., Abdelmoula, M., Genin, J. M., and Ehrhardt, J. J. 2002. Surface chemistry and structural properties of mackinawite prepared by reaction of sulfide ions with metallic iron. *Geochim Cosmochim Ac* 66 (5):829-836.

Rickard, D., and Luther, G. W. 2007. Chemistry of iron sulfides. *Chem Rev* 107 (2):514-562.

Wan, M., Shchukarev, A., Lohmayer, R., Planer-Friedrich, B., and Peiffer, S. 2014. Occurrence of surface polysulfides during the interaction between ferric (hydr)oxides and aqueous sulfide. *Environ Sci Technol* 48 (15):8932-8932.

Appendix B

Supporting Information for Chapter 4

B1. D-spacing calculation.

The calculation of d-spacing between the layers using the intensity profiles was completed using Gatan Microscopy Suite® (GMS, version 2.32, Gatan, Inc., Pleasanton, CA). Figure B1A was obtained from the FeS with PCE sample. To calculate the d-spacing between the atomic layers (Figure B1A), an intensity profile of the layers inside the yellow box is shown in Figure B1B. The valleys in Figure B1B correspond with the atomic layers, and each peak represents one d-spacing between two atomic layers. As shown in Figure B1B, the length of eight peaks equals 4 nm, each peak is 5 Å long (4 nm divided by 8, 1 nm equals 10 Å). Thus, the d-spacing of atomic layers inside the yellow box equals 5 Å.

Table B1. Atomic percent (in %) of surface species on the FeS surface

	Binding Energy (eV)*	FeS control (%)	FeS with TCE (%)	FeS with PCE (%)
Sulfur Species (Figure 4.7)				
peak S1	161.5	30.6	23.5	25.9
peak S2	162.1	40.6	43.9	43.4
peak S3	163.1	28.8	32.6	30.7
Oxygen Species (Figure 4.8)				
peak O1	530.0	20.4	15.9	16.9
peak O2	531.6	60.3	50.3	51.0
peak O3	533.2	19.3	33.8	32.1
Carbon Species (Figure 4.9)				
peak C1	282.3	5.5	8.3	3.3
peak C2	284.8	43.6	35.9	31.5
peak C3	286.3	34.9	40.6	46.2
peaks C4	288.5	16.0	15.2	19.0

* Binding energy is accurate ± 0.2 eV.

Table B2. Changes in Fe:S and Fe:O in FeS samples during reaction with TCE and PCE at pH 8.

	XPS	SEM-EDS*	TEM-EDS**
FeS control			
Fe:S	0.9	1.0	0.8
Fe:O	1.7	3.9	6.0
FeS with TCE			
Fe:S	0.8	1.0	0.8
Fe:O	2.4	2.4	2.4
FeS with PCE			
Fe:S	0.9	0.9	0.8
Fe:O	2.6	3.5	3.9

*EDS results obtained using SEM, 32 days, n=5-7.
**EDS results obtained using TEM, 7 weeks, n=12-16.

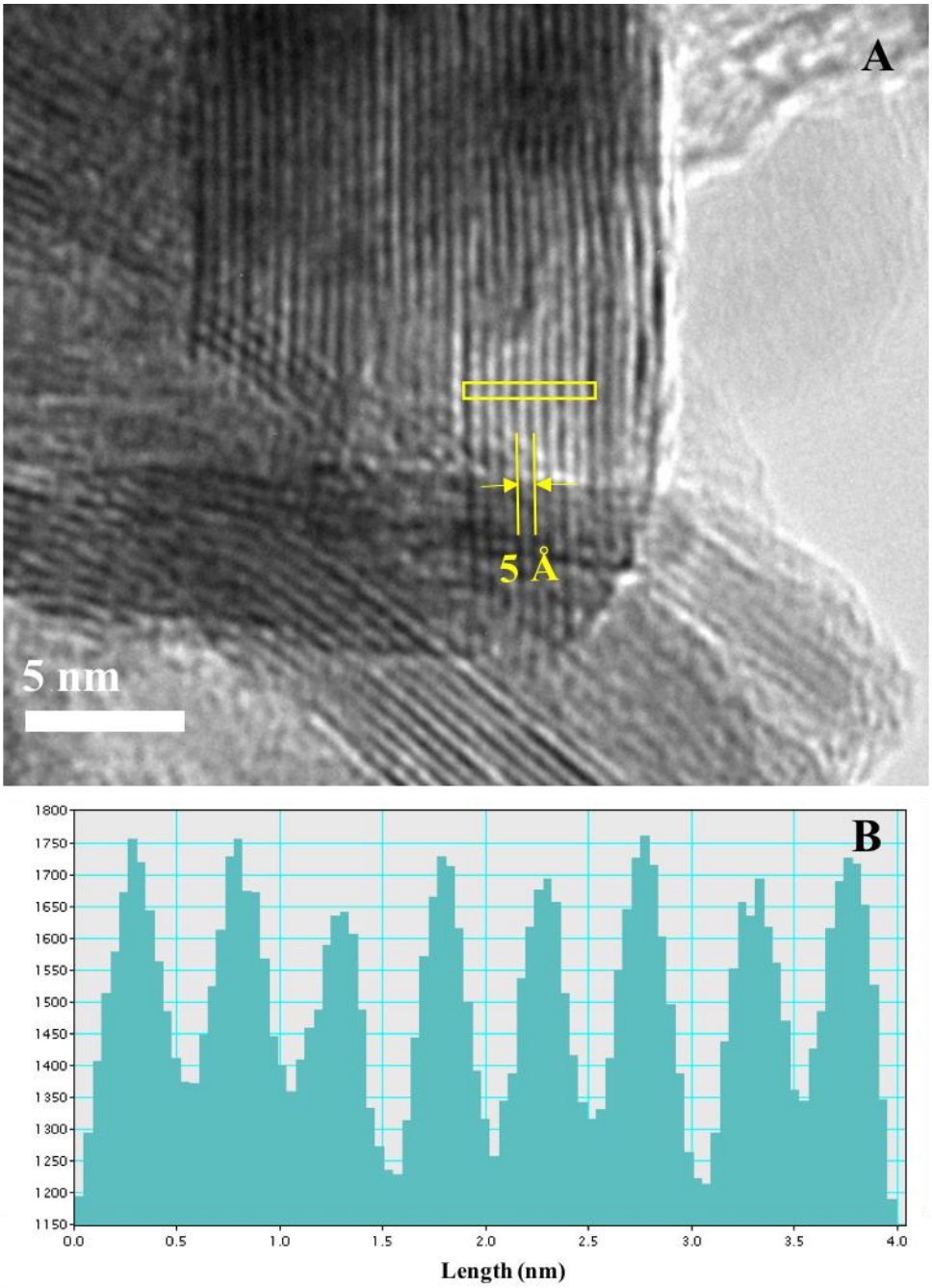


Figure B1. Calculation of d-spacing using HRTEM images obtained from FeS with PCE sample using Gatan Microscopy Suite® (version 2.32, Gatan, Inc., Pleasanton, CA). (A) HRTEM image of FeS with PCE, pH 8, seven weeks; (B) intensity profile from the atomic layers shown inside the yellow box in (A).

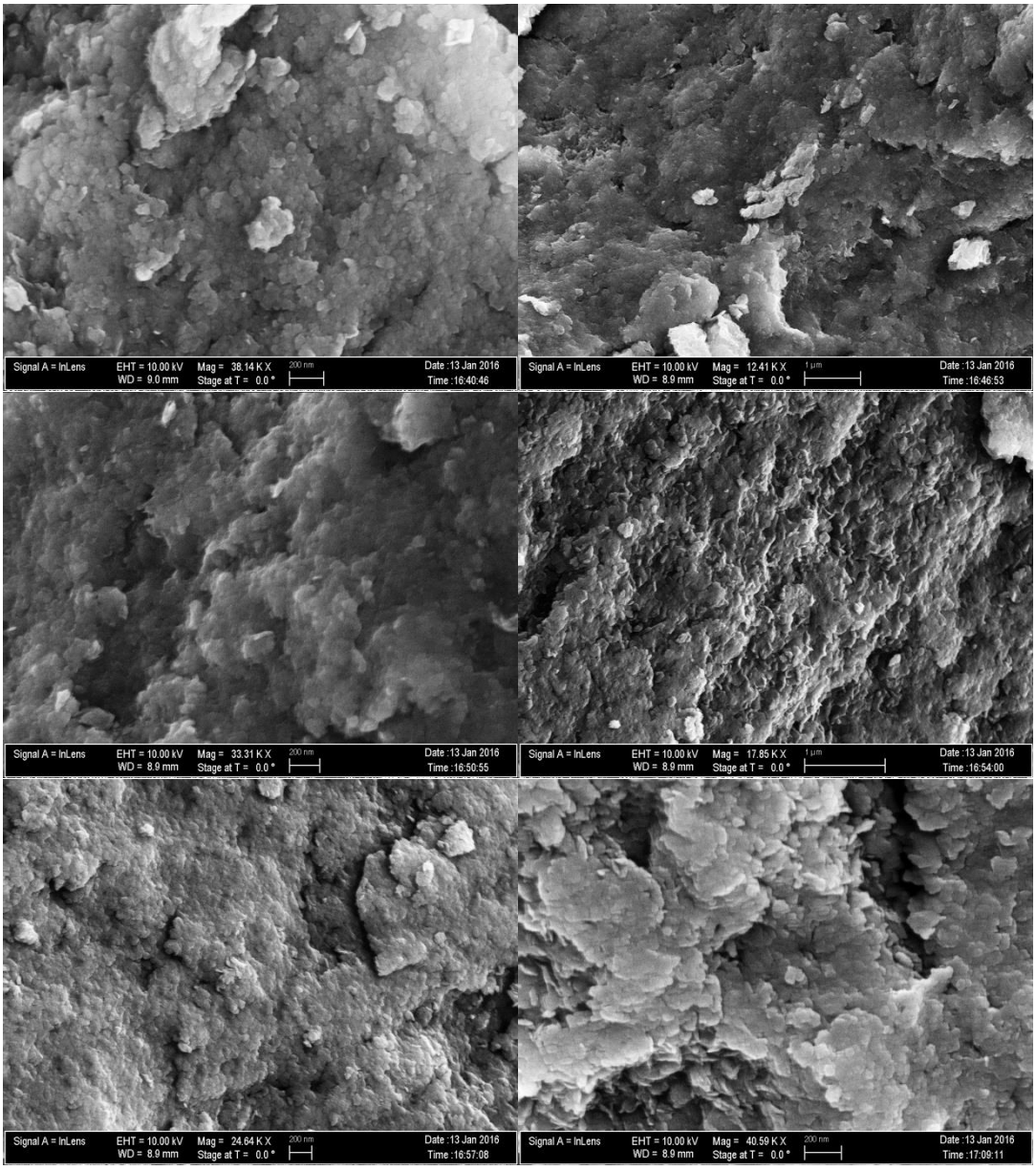


Figure B2. SEM images of the surface of FeS control sample, pH 8, 1 hour.

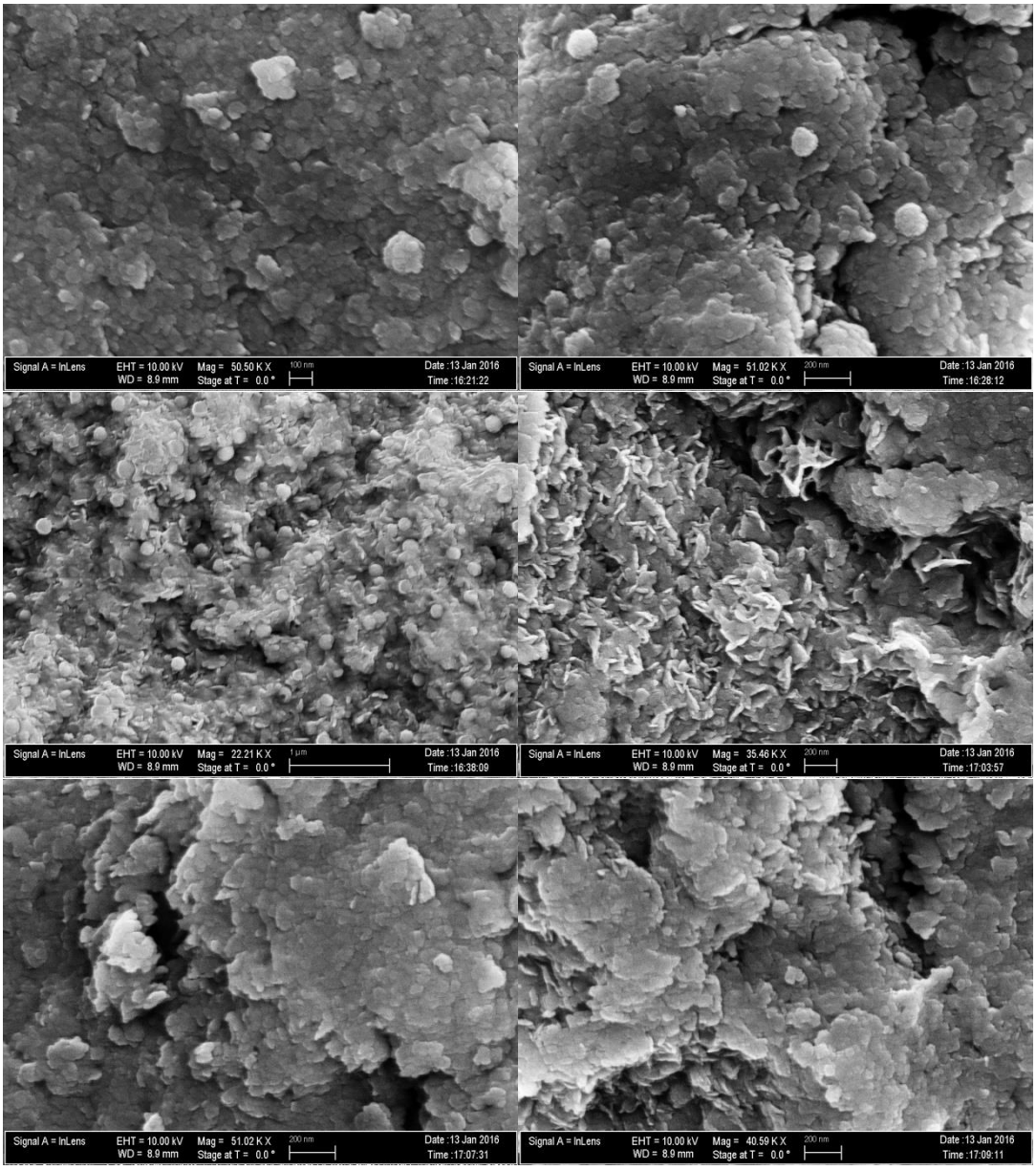


Figure B3. SEM images of the surface of FeS control sample, pH 8, 16 days.

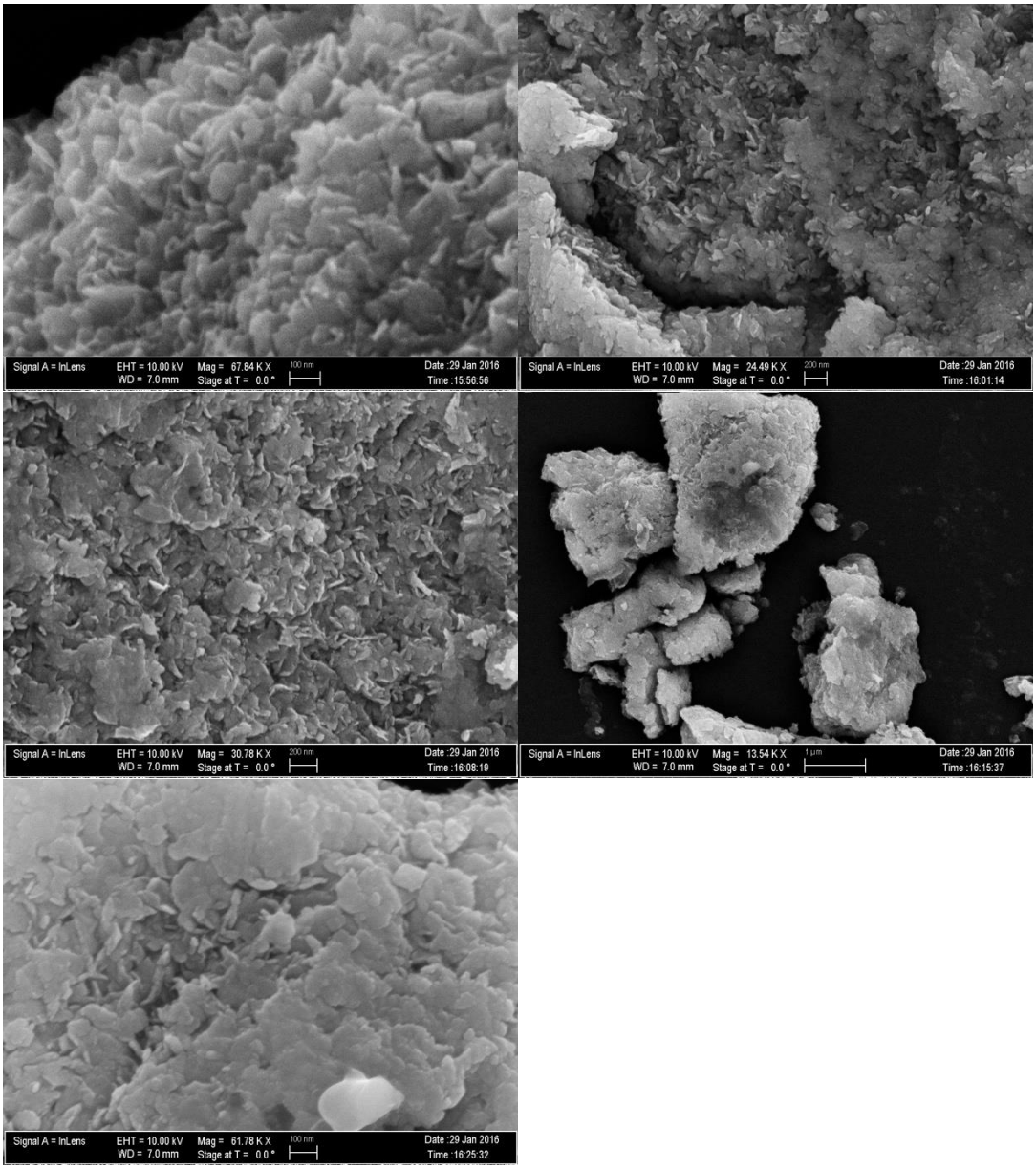


Figure B4. SEM images of the surface of FeS control sample, pH 8, 32 days.

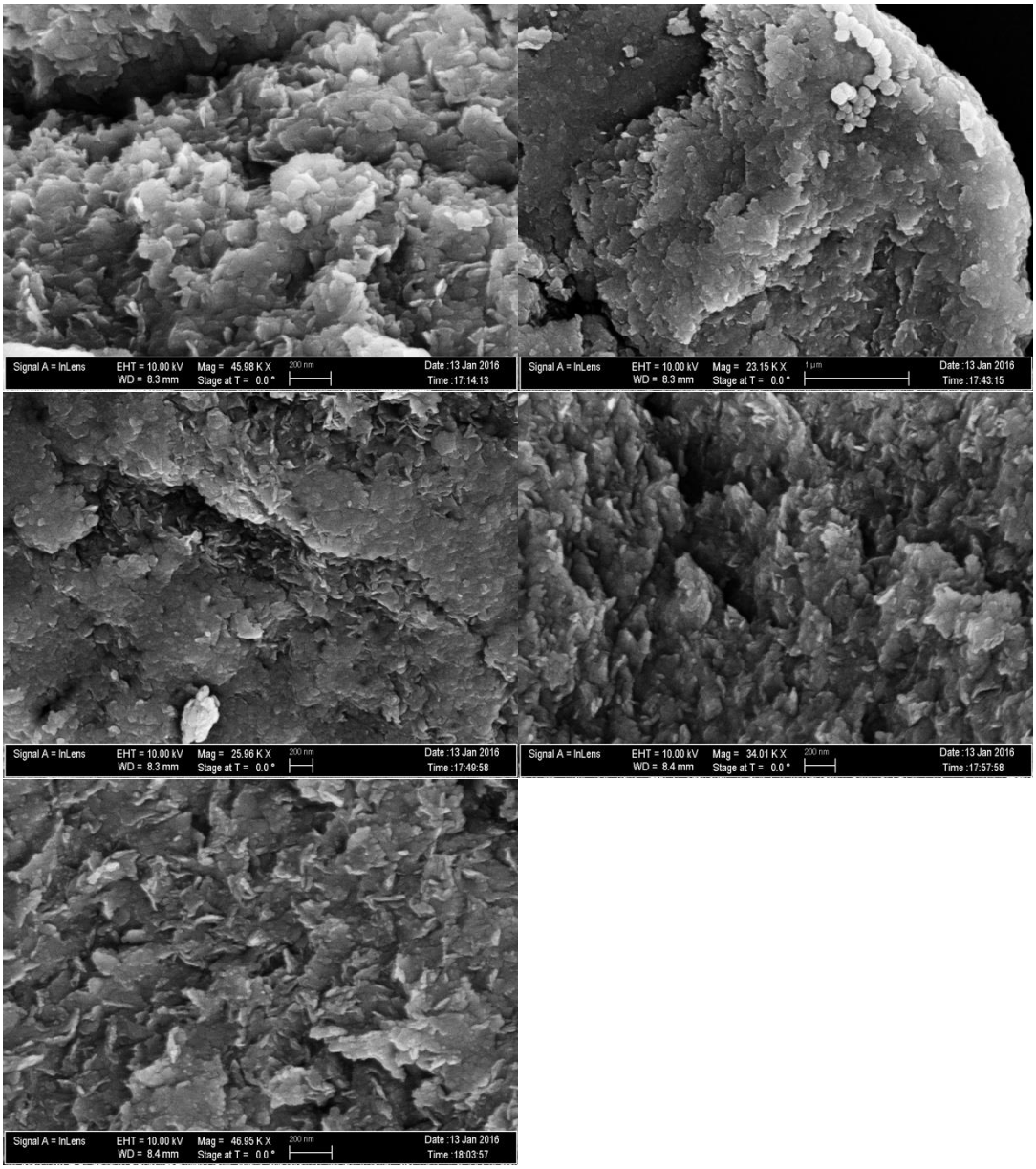


Figure B5. SEM images of the surface of FeS with TCE sample, pH 8, 16 days.

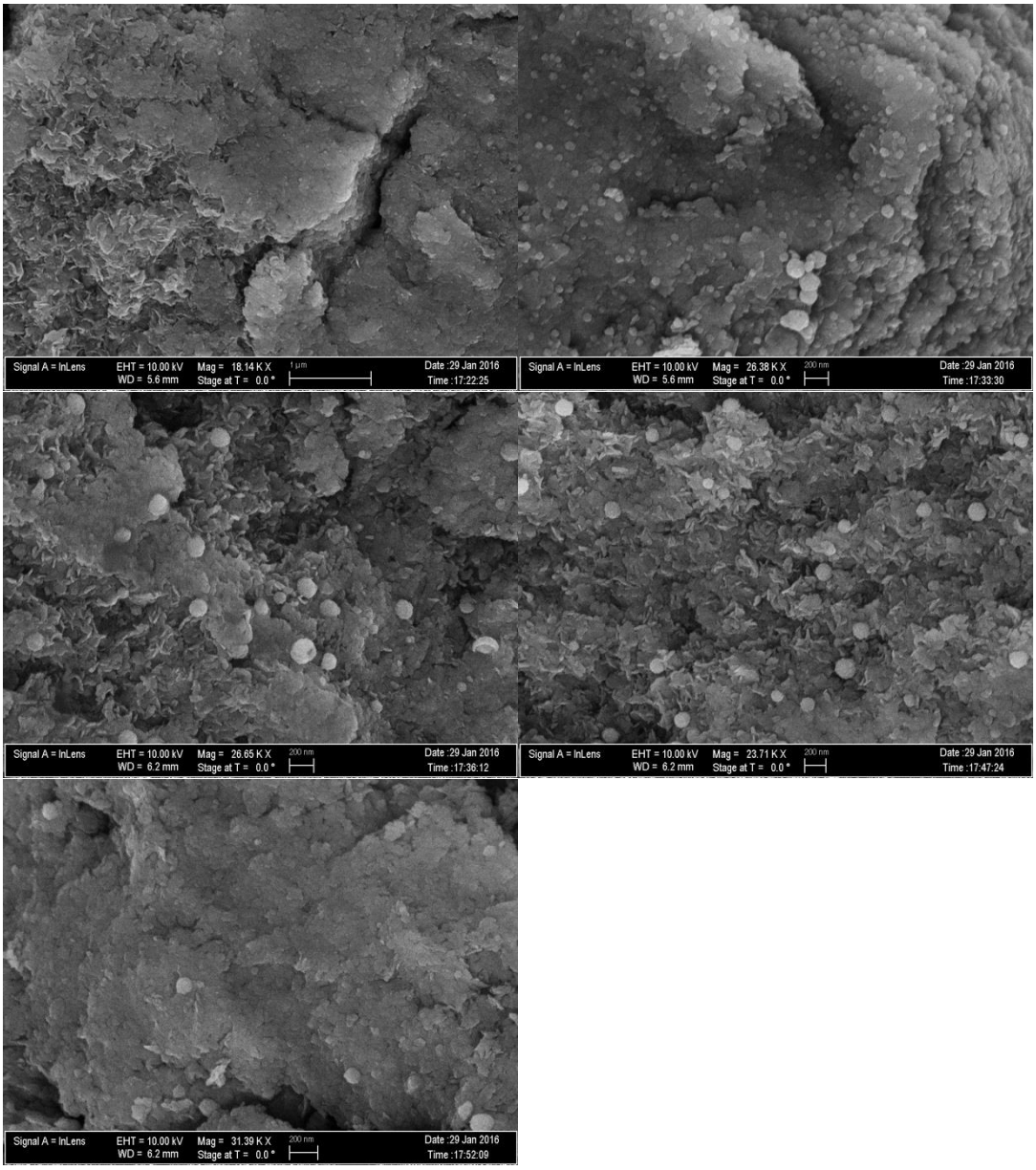


Figure B6. SEM images of the surface of FeS with TCE sample, pH 8, 32 days.

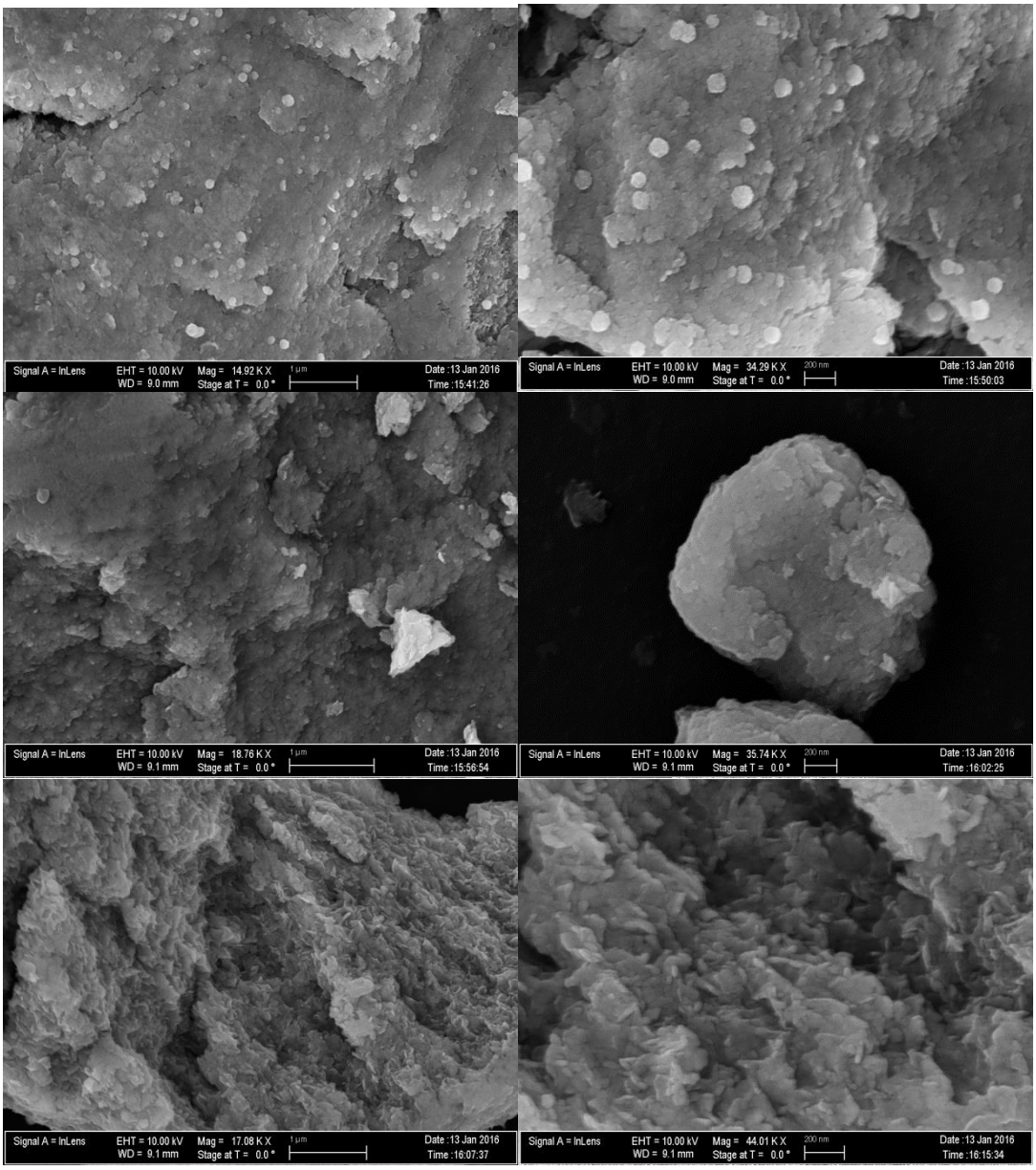


Figure B7. SEM images of the surface of FeS with PCE sample, pH 8, 16 days.

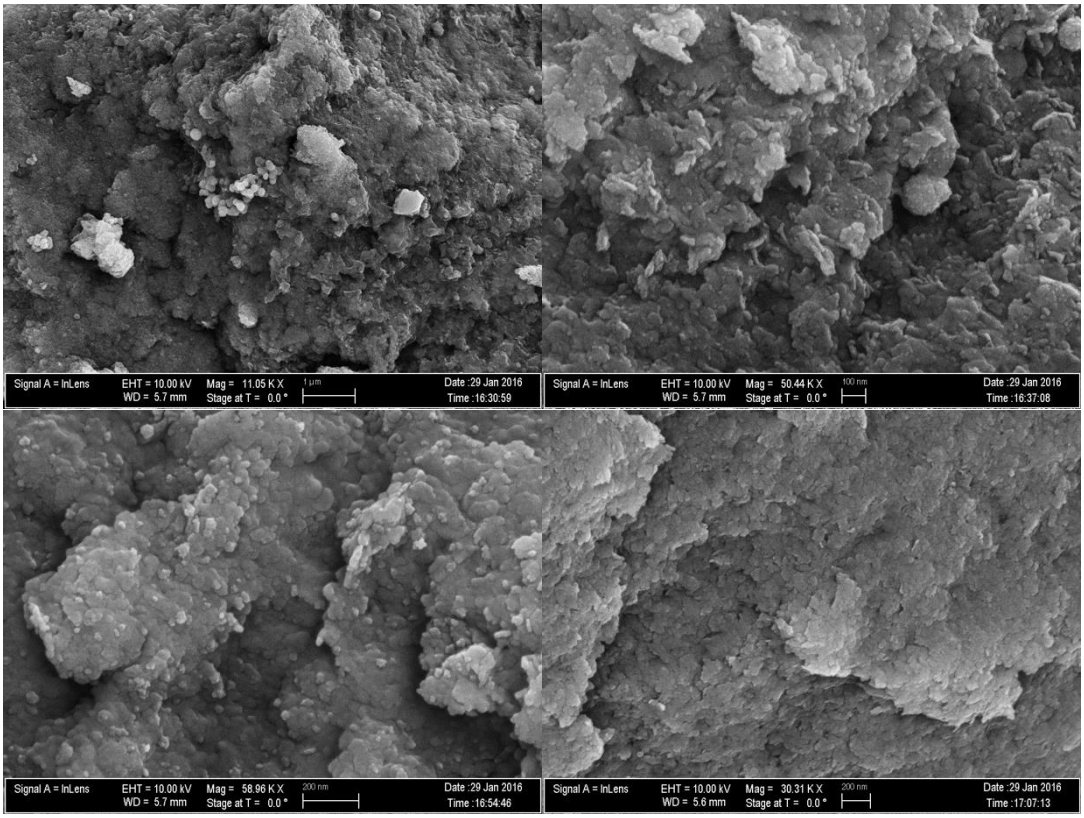


Figure B8. SEM images of the surface of FeS with PCE sample, pH 8, 32 days.

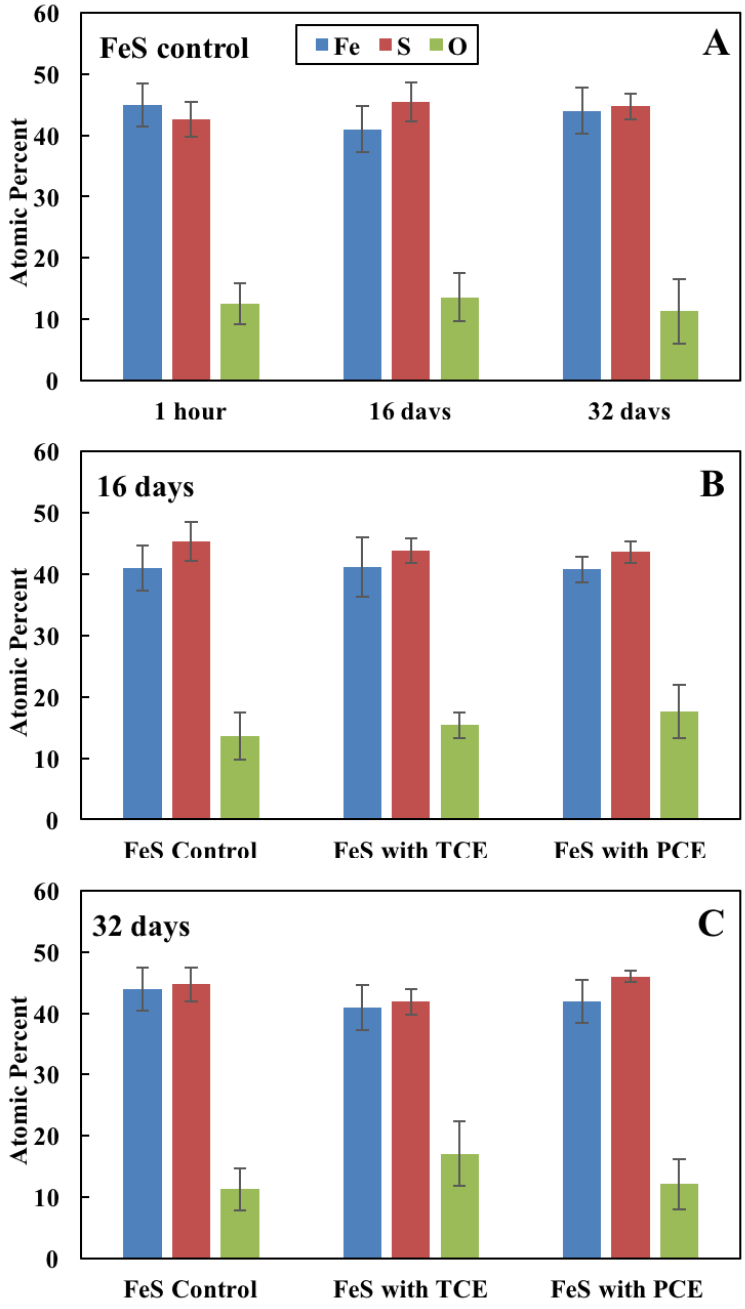


Figure B9. Atomic percent of FeS samples (A) FeS control at different times; (B) 16 days, pH 8; (C) 32 days, pH 8 (n=5-7).

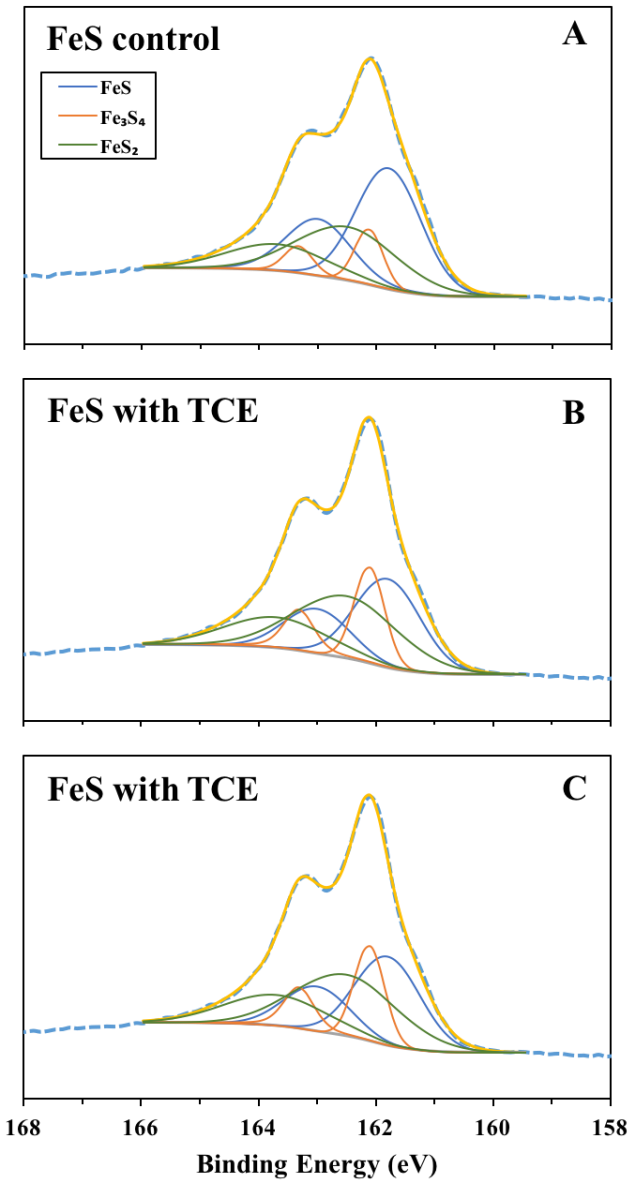


Figure B10. The S 2p XPS spectra of FeS surface (fitted using peaks with binding energies consistent with iron sulfides minerals), pH 8, seven weeks. (A) FeS control; (B) FeS with TCE; (C) FeS with PCE. Blue dotted lines are experimental data, and yellow lines are corresponding fits.

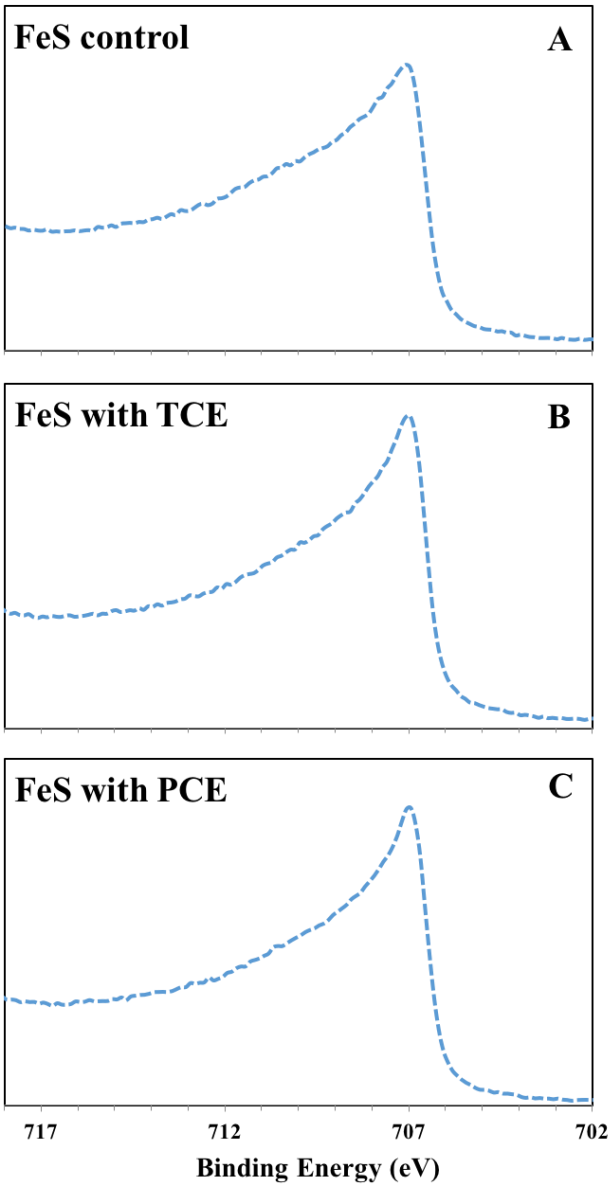


Figure B11. The Fe $2p_{3/2}$ XPS spectra of FeS surface, pH 8, seven weeks. (A) FeS control; (B) FeS with TCE; (C) FeS with PCE.